

AD _____

Award Number: W81XWH-11-2-0076

TITLE: New Methods of Low-Field MRI for Application to Traumatic Brain Injury

PRINCIPAL INVESTIGATOR: Matthew S. Rosen, Ph.D.

CONTRACTING ORGANIZATION: Harvard University, Cambridge MA 02138

REPORT DATE: April 2014

TYPE OF REPORT: Annual

PREPARED FOR: U.S. Army Medical Research and Materiel Command
Fort Detrick, MD 21702-5012

DISTRIBUTION STATEMENT:

X Approved for public release; distribution unlimited

The views, opinions and/or findings contained in this report are those of the author(s) and should not be construed as an official Department of the Army position, policy or decision unless so designated by other documentation.

REPORT DOCUMENTATION PAGE				Form Approved OMB No. 0704-0188	
Public reporting burden for this collection of information is estimated to average 1 hour per response, including the time for reviewing instructions, searching existing data sources, gathering and maintaining the data needed, and completing and reviewing this collection of information. Send comments regarding this burden estimate or any other aspect of this collection of information, including suggestions for reducing this burden to Department of Defense, Washington Headquarters Services, Directorate for Information Operations and Reports (0704-0188), 1215 Jefferson Davis Highway, Suite 1204, Arlington, VA 22202-4302. Respondents should be aware that notwithstanding any other provision of law, no person shall be subject to any penalty for failing to comply with a collection of information if it does not display a currently valid OMB control number. PLEASE DO NOT RETURN YOUR FORM TO THE ABOVE ADDRESS.					
1. REPORT DATE (DD-MM-YYYY) April 2014		2. REPORT TYPE Annual		3. DATES COVERED (From - To) 10January2013-9January2014	
4. TITLE AND SUBTITLE New Methods of Low-Field MRI for Application to TBI				5a. CONTRACT NUMBER	
				5b. GRANT NUMBER W81XWH-11-2-0076	
				5c. PROGRAM ELEMENT NUMBER	
6. AUTHOR(S) Matthew S. Rosen, PhD email:mrosen@cfa.harvard.edu				5d. PROJECT NUMBER	
				5e. TASK NUMBER	
				5f. WORK UNIT NUMBER	
7. PERFORMING ORGANIZATION NAME(S) AND ADDRESS(ES) Harvard University, Cambridge MA 02138				8. PERFORMING ORGANIZATION REPORT NUMBER	
9. SPONSORING / MONITORING AGENCY NAME(S) AND ADDRESS(ES) U.S. Army Medical Research and Materiel Command Fort Detrick, MD 21702-5012				10. SPONSOR/MONITOR'S ACRONYM(S)	
				11. SPONSOR/MONITOR'S REPORT NUMBER(S)	
12. DISTRIBUTION / AVAILABILITY STATEMENT Approved for public release; distribution unlimited.					
13. SUPPLEMENTARY NOTES					
14. ABSTRACT We are developing robust low-magnetic-field implementations of MRI (LFI) focused on brain imaging with two complimentary test scanner systems: electromagnet and permanent magnet based. We have also developing injury-sensitive MRI based on the detection of free radicals associated with injury using the Overhauser effect and subsequently imaging that modified nuclear polarization using low-field MRI (OMRI). We have been optimizing imaging sequences, image reconstruction, and parallel imaging based acceleration in this unique regime. Results include demonstration of 3D human brain imaging in the electromagnet LFI at 6.5 mT, 2D imaging in a 100 lb scanner based on a rotating permanent magnet array, and free-radical imaging ex vivo as a path toward in vivo applications. Application of the suite of techniques and technologies from our work could advise future development of a deployable device with a high diagnostic impact, transforming diagnosis and monitoring of secondary injury prevalent in TBI.					
15. SUBJECT TERMS Low-field brain MRI, Injury-sensitive MRI, Free radical Overhauser imaging.					
16. SECURITY CLASSIFICATION OF:			17. LIMITATION OF ABSTRACT UU	18. NUMBER OF PAGES 111	19a. NAME OF RESPONSIBLE PERSON USAMRMC
a. REPORT U	b. ABSTRACT U	c. THIS PAGE U			19b. TELEPHONE NUMBER (include area code)

Table of Contents

INTRODUCTION:	5
BODY:	6
Low Field Imagers (LFIs)	6
TASK 1A: Low-field MRI Hardware Development	6
<i>HALBACH ARRAY (PERMANENT MAGNET) LFI</i>	<i>7</i>
<i>AUTOMATING ACQUISITION</i>	<i>7</i>
<i>PARALLEL-ARRAY DETECTORS FOR THE ELECTROMAGNET LFI</i>	<i>9</i>
<i>RECEIVE COIL DEVELOPMENT</i>	<i>9</i>
TASK 1B: System control and image acquisition	20
<i>SEQUENCE DESIGN AND OPTIMIZATION</i>	
<i>SPIRAL IMAGING IN THE ELECTROMAGNET LFI</i>	<i>20</i>
<i>MAGNETIC RESONANCE FINGERPRINTING AT 6.5 MILLITESLA</i>	<i>25</i>
<i>8 CHANNEL IMAGE ACQUISITION AND RECONSTRUCTION</i>	<i>27</i>
<i>HALBACH ARRAY LFI:</i>	
<i>IMAGING IN THE ROTATING PERMANENT MAGNET:</i>	<i>31</i>
<i>ASSESSING RESOLUTION</i>	<i>37</i>
<i>FIELD MAPPING TOWARDS 3D IMAGING</i>	<i>40</i>
<i>SPATIAL ENCODING IN 3D:</i>	<i>41</i>
<i>FUTURE WORK</i>	<i>45</i>
TASK 1C: Demonstration of head imaging	46
<i>BRAIN MRI IN THE ELECTROMAGNET LFI AT 6.5 MILLITESLA</i>	<i>46</i>
OMRI Injury Imaging	51
TASK 2A: OMRI Hardware Development	51

<i>IMPROVING RADICAL DETECTION SENSITIVITY THROUGH PULSE SEQUENCE DESIGN</i>	52
<i>PARALLEL IMAGING AND SENSE WITH OMRI</i>	54
TASK 2C: <i>Ex vivo</i> radical detection	57
<i>FREE RADICAL DETECTION IN RODENT BLOOD</i>	57
<i>EXOGENOUS FREE RADICALS AS PROBE OF BBB AND REDOX STATUS IN RATS</i>	58
KEY RESEARCH ACCOMPLISHMENTS:	61
REPORTABLE OUTCOMES:	63
CONCLUSION:	64
REFERENCES:	66
APPENDICIES:	70
<i>YEAR 3 STATEMENT OF WORK</i>	71
<i>ABSTRACTS ACCEPTED FOR PRESENTATION</i>	72
<i>OMRI MANUSCRIPT (PUBLISHED, 2014)</i>	78
<i>HALBACH MANUSCRIPT (ACCEPTED FOR PUBLICATION, 2014)</i>	89

INTRODUCTION:

Year Three of this applied research program continues to build on advances by our collaboration in the development of novel methods and advanced hardware for low-magnetic-field MRI. Without major innovation, high-field MRI instruments offer limited utility for imaging TBI in widely deployable contexts. We focus our research effort on the high-risk and critical challenges that must be solved to enable deployment of a transportable human-head MRI system applicable to TBI imaging in battlefield medical facilities. Our goal is to establish proof-of-principle of a suite of techniques and technologies to advise future development of a field-deployable device with high diagnostic impact. This research effort has two specific aims:

Specific Aim 1: Develop a low-field human-head MRI system (LFI) suitable for high-resolution multi-nuclear imaging, and improve the ability to attain brain images based on the intrinsic *in vivo* ^1H NMR signal in this scanner.

This includes the development of *two* robust low-field scanner hardware methodologies (electromagnet based and permanent magnet based), the development of novel high-speed parallel imaging detection systems, and work on advanced adaptive reconstruction methods including navigators and sparse sampling.

Specific Aim 2: Develop injury-sensitive MRI based on converting the electron spin of free radicals associated with injury (specifically TBI) into nuclear polarization using the Overhauser effect and subsequently imaging that modified nuclear polarization using low-field MRI (**OMRI**). Successful demonstration of OMRI of free radicals associated with injury will be directly applicable to the MRI systems of **Aim 1**, enhancing image-based injury specificity and/or shortening scan acquisition time.

The development of this new MRI contrast mechanism may provide an unambiguous non-invasive *in vivo* marker for cerebral injury, and has potential for assisting the imaging of TBI at both low and high magnetic fields.

BODY:

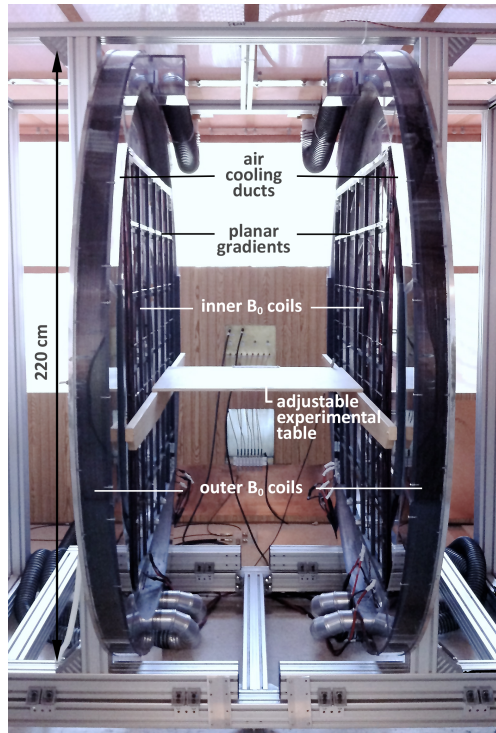
Progress in Year 3 has focused on the optimization of image acquisition strategies and pulse-sequences for the low-field MRI hardware developed during Y1 and demonstrated in Y2. The low-field MRI hardware includes two **LFI** systems (**Aim 1**) and the **OMRI** system (**Aim 2**). The work presented here includes the first 3D human head imaging obtained in the electromagnet LFI, the first high-resolution 2D imaging in the permanent magnet based scanner, and a demonstration of Overhauser-enhanced MRI in a pilot study in rodents *ex vivo* as a first step in new perspectives for the measurement of free radicals *in vivo*.

Low Field Imagers (LFIs)

TASK 1A: Low-field MRI Hardware Development

Much of the of hardware development for the human head LFI test bed systems (Aim 1) and for the OMRI system (Aim 2) was completed in Y1. Hardware development in Y3 includes the automation of data collection with Halbach LFI, and a study of multi-channel imaging coils for the electromagnet LFI at 276 kHz.

The electromagnet LFI (shown below) is an ideal state-of-the art test bed for all of the novel acquisition, detection methodologies, and reconstruction algorithms including navigators and



sparse sampling, and additionally will provide necessary experience and data to advise optimal construction and magnetic field for any future electromagnet-based deployable systems. Currently, this state-of-the-art scanner enables high-performance spectroscopy and 8-channel imaging at 6.5 mT, and is fully equipped for Overhauser DNP experiments.

The permanent magnet system is a lightweight (45 kg) and portable Halbach array. This Halbach array scanner is a highly specialized and potentially disruptive technology scanner that could greatly ease both the cost and burden of a field-forward instrument purpose-built for TBI imaging. This Halbach imager contrasts markedly with the electromagnet LFI in that it has a highly inhomogeneous magnetic field, but we use this inhomogeneity to our advantage as an encoding field to acquire head images without the use of an additional gradient set.

Halbach array (permanent magnet) LFI

This test bed scanner is based around a lightweight array of permanent magnets in a so-called Halbach configuration. This magnet is ideal for portable MRI in that it creates a relatively uniform field transverse to the head without the use of a cryostat or power supplies. This Halbach array scanner is a highly specialized scanner and a potentially disruptive technology that could greatly ease both the cost and burden of a field-forward instrument purpose-built for TBI imaging. This Halbach imager contrasts markedly with the electromagnetic LFI in that it has a highly inhomogeneous magnetic field, but we use this inhomogeneity to our advantage and use it to acquire head images without the use of an additional gradient set.

A truly portable MR system has the potential to quickly detect brain injury at the site of injury. For example hemorrhage detection is critical for both stroke patients and traumatic brain injury victims. In stroke, rapid distinction between a hemorrhagic and non-hemorrhagic event could allow administration of a clot-busting drug such as tPA (tissue plasminogen activator) in an ambulance prior to transportation to the hospital, perhaps advancing this time-sensitive treatment by up to an hour. Subdural hemorrhage (or hematoma) is a form of traumatic brain injury, in which blood gathers between the dura and arachnoid mater (in meningeal layer) and is likely to be visualized on coarse resolution (e.g. 5 mm) T1 images.

In Y1 we designed and built the very portable 45 kg Halbach array magnet for portable MRI, and mapped the magnetic field and drift using NMR measurements at 3.3 MHz. In Y2 we focused on the hardware and encoding techniques needed to turn this magnet into an imager. In Y3, we have solved some critical challenges including the ability to acquire multi-channel images, and we describe these efforts below.

Halbach array LFI: automating acquisition

Significant strides toward routine imaging with the Halbach scanner were made this year. Most notably, data acquisition has been automated using a DC stepper motor controlled by gradient driver pulses from the Tecmag Apollo spectrometer. Two implementations were developed and are described below.

Belt drive stepper motor configuration and RF shielding

To speed up image acquisition and improve repeatability, a DC stepper motor was connected to rollers beneath the Halbach magnet with a pulley mechanism (**Figure 1**). The motor is controlled using short pulses from the Tecmag Apollo spectrometer via one of the gradient control outputs, which are not needed for imaging on the system. Synchronization of the motor triggering with

the pulse sequence allows magnet rotation to occur between TRs. The motor streamlines data collection, saving time and reducing magnet temperature drift over the course of the acquisition.

A Faraday cage-style enclosure consisting of polycarbonate panels clad with copper cloth was fabricated to reduce RF noise inside the magnet. The panels are mounted on a frame of aluminum strut built around the scanner, and are grounded at a single point. RF cables are routed through a connectorized feed-through panel to ensure RF isolation. After moving the magnet inside the enclosure, we observed a large signal-to-noise ratio (SNR) improvement (roughly a factor of 10). As a result, both broadband and synchronous noise are suppressed, reducing the noise floor as well as the presence of interfering environmental spectral lines. This translates directly into improved image quality and reduced acquisition time. High SNR datasets can now be obtained in 10 minutes per channel as compared to ~60 minutes previously though the use of the motor drive and RF cladding.

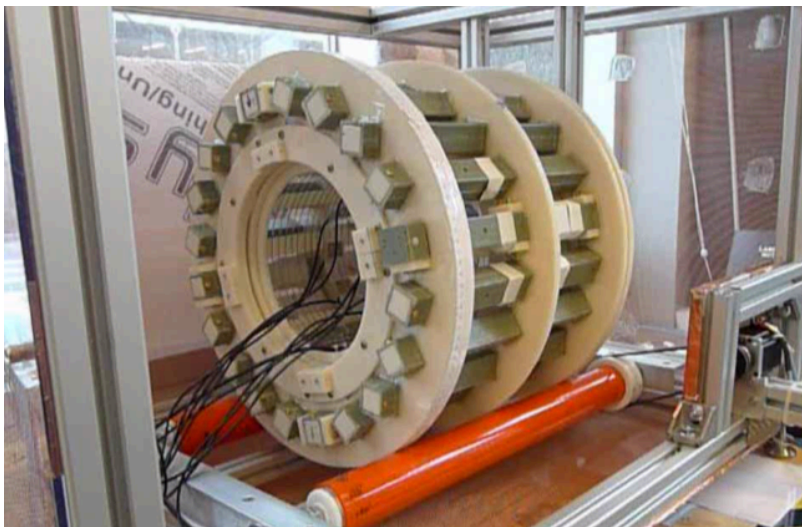


Figure 1: A Faraday enclosure for the Halbach was constructed with copper-cloth on an aluminum strut frame. This enclosure reduced the noise floor by a factor of order 10. Additionally, automated acquisition of NMR projections and field maps is now possible using a DC stepper motor with a belt drive system (seen in the lower-right) that is controlled within the NMR sequence. This automation was a key step to improve the data rate, shortening scan times, as well as ensuring reproducible magnet angular positioning critical to the image reconstruction algorithms.

Direct-drive stepper motor configuration

Although the belt-driven system enabled automated image encoding, subsequent investigation revealed that the belt-drive system was prone to slippage, making the projection data unreliable. To counter this problem, we switched to a direct axle-driven geometry using aluminum axle couplers (Figure 2). The direct-drive approach demands more torque from the stepper motor, requiring use of an in-line gear-ratio transformer. This motor configuration produces much

more repeatable rotations of the Halbach magnet, eliminating a source of systematic error in the image reconstructions.

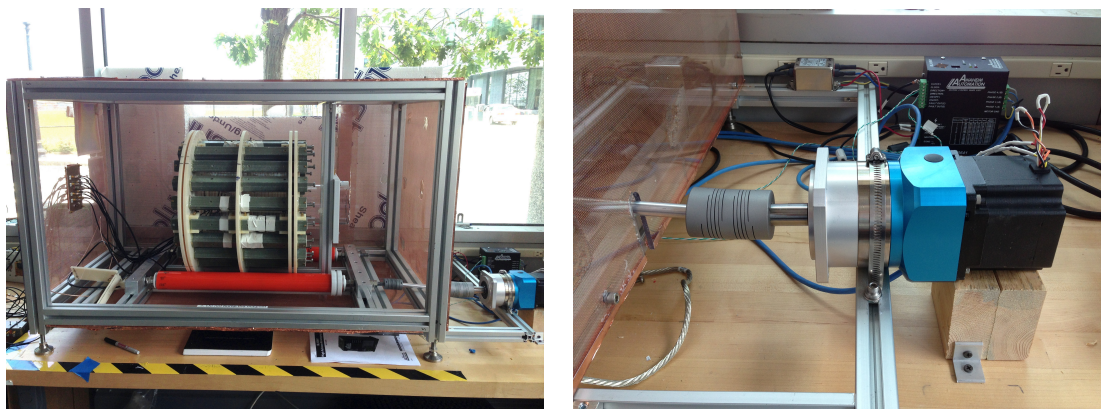


Figure 2: The Halbach magnet (left) with RF shield, aluminum support struts, urethane-clad rollers, and stepper motor assembly. A close-up of the stepper motor, gear-ratio transformer, and axle coupler are shown at right. The stepper motor controller box (visible in the background, right side) is blanked during signal acquisition to prevent electromagnetic interference.

Parallel-array detectors for the electromagnet LFI

We continue to work to understand the limits of acceleration that are possible with low-field MRI including implementation of parallel imaging with array coils. At conventional high-field MRI scanner operational frequencies, “body noise” dominates inductive copper loop detection, resulting in strongly correlated noise on each receive coil in the parallel array. At low field, uncorrelated Johnson noise dominates, which proves a benefit to parallel imaging and accelerated imaging using SENSitivity Encoding (**SENSE**). We previously demonstrated the first 8-channel parallel imaging and acceleration obtained in this new Johnson-noise dominated regime [1]. Progress toward high-performance multi-channel array coils for operation at 276 kHz has been at times frustrated by the lack of robust decoupling strategies in this frequency regime, and we describe our efforts below.

Parallel-array detectors: receive coil development

As discussed in the Y2 Annual Report, parallel imaging at low frequency is a new regime and the optimal receive coil parameters are unknown from the literature. In Y2 we built a simple 8-channel cylindrical array using 30-turn coils with an inner diameter of 8 cm. The individual elements of that coil each required their own tuning and matching circuit board, which was designed and produced on our circuit board router. Each coil element was placed on the 3D form

and tuned/matched to 276 kHz with at least -20 dB return loss. A photograph of the complete 8-channel receive array coil is shown in Figure 3



Figure 3: The Y2 eight-channel array coil (**left**) and the tune/match electronics stack (**right**).

Eight channel “helmet” receive array coil design:

We present here the design of an eight-channel helmet array, for use in *in vivo* human brain imaging in the electromagnet LFI. This 8 channel array has higher sensitivity than a correspondingly sized single channel solenoid receive coil owing to the placement of multiple smaller coils as close to the head as possible in the array.

An anatomical human head model from ANSYS (Figure 4) was used to guide the contouring of the helmet form. These models are anatomically and physiologically correct, and were scaled up slightly to provide a more universal fit for our helmet.

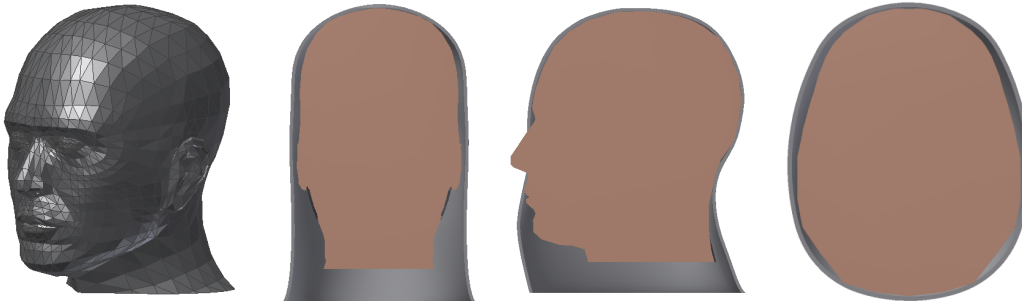


Figure 4: ANSYS human head model (left) and (right) three section views of a head inside the array.

To optimize coverage of the brain by the receive array, the helmet was tiled with 8 coils as shown in Figure 5:

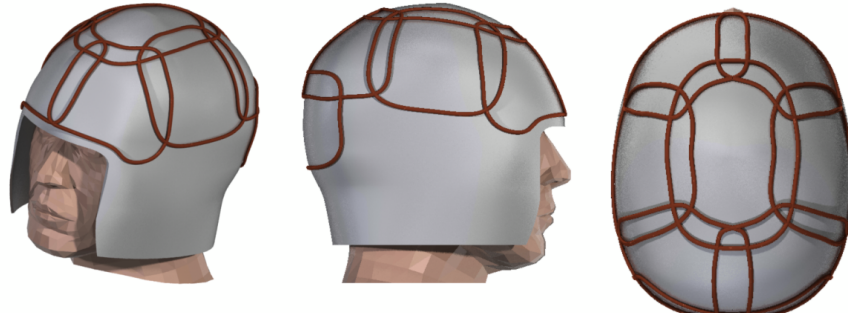


Figure 5: Optimized tiling pattern for the eight receive coils, for operation at 276 kHz.

The final receive array design (Figure 6) includes structures for centering the helmet array inside our 30 cm transmit solenoid coil. The helmet was printed of Polycarbonate in house with a StrataSys Fortus 360mc 3D printer.

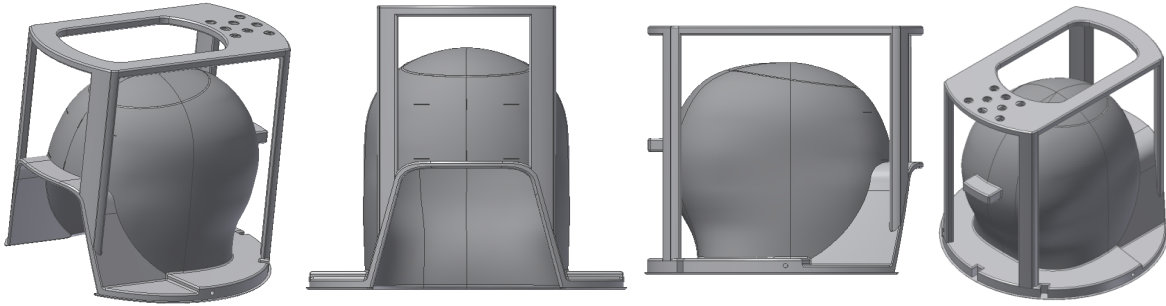


Figure 6: “Helmet” array mechanical design, including strain relief and supports, BNC bulkhead mounting provision, and alignment supports for the 30 cm TX coil.

The combined assembly for multi-channel acquisition of *in vivo* human brain images is rendered in Figure 7. This includes the transparent 30 cm diameter solenoid transmit coil surrounding the eight channel receive array.

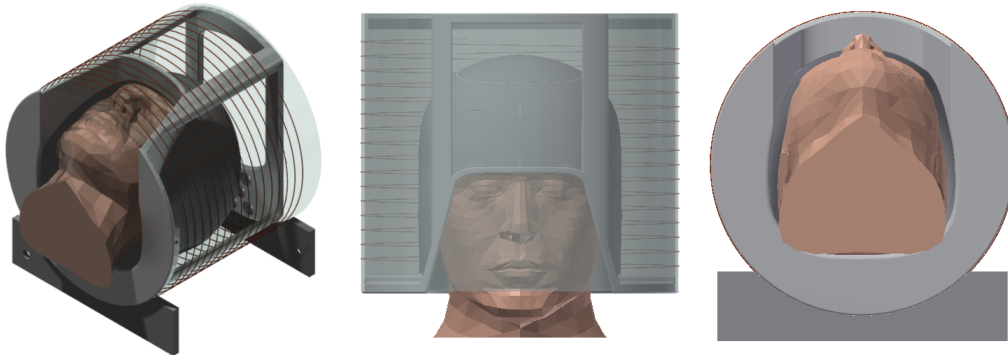


Figure 7: 3D rendering of the complete assembly: eight channel receive array inside the transmit coil.

Eight channel “helmet” receive array coil construction:

A tight fitting helmet was designed and 3D printed using fused deposition modeling with polycarbonate in our Fortus 360 mc printer (Stratasys, Eden Prairie, MN, USA). Coil sizes and positioning were determined by balancing the following requirements

- 1) To acquire signal, coils cannot be perpendicular to B_0 . In our magnet, B_0 is normal to the sagittal plane when the subject is supine. This translates to not placing coils on the sides of the helmet level with the ears.
- 2) Our low-field imager has only eight receive channels. Maximum coverage must be obtained with only eight coils.
- 3) The coils will couple to each other. Coupling will adversely affect signal acquisition and image quality. To simplify decoupling, coil placement should be symmetric. Nearest neighbors can be geometrically decoupled from each other by overlapping loops. This overlap will be the primary factor in determining final coil placement.

With these criteria, we elected to build eight 30-turn receive-only coils using 24 AWG wire with four 12 cm and four 14 cm diameter loops. A 14 cm coil was placed at the top of the helmet centered about the midline. The four 12 cm coils were then tiled—two ventral and two dorsal to the 14 cm coil—symmetrically about the midline to obtain geometric decoupling between nearest neighbors of at least -38 db. Two 14 cm coils were placed lateral to the first 14 cm coil (one on each side) and positioned to obtain geometric decoupling between the three neighboring coils of at least -30 db. The final 14 cm coil was placed dorsal to all previously placed coils and geometrically decoupled to its nearest neighbors to at least -40 db. With all coils placed, decoupling between next nearest neighbors was at least -6 dB. Passive decoupling between transmit and receive was achieved using crossed diodes in series with transmit, and in parallel with receive. Table 1 contains the complete decoupling matrix. Once all coils were placed, they were tuned to 276 kHz and matched to 50Ω . Table 2 contains final tuning values. The final populated helmet is shown in Figure 8.

Coil	1	2	3	4	5	6	7	8
1	-	-40 (1)	-40 (1)	-40 (2)	-6 (15)	-13 (10)	-17 (9)	-13 (10)
2	-	-	-38 (2)	-41 (2)	-35 (2)	-40 (1)	-6 (15)	-40 (1)
3	-	-	-	-5 (18)	-43 (1)	-11 (10)	-16 (9)	-12 (10)

4	-	-	-	-	-6 (14)	-6 (13)	-7 (13)	-40 (1)
5	-	-	-	-	-	-30 (8)	-6 (15)	-6 (15)
6	-	-	-	-	-	-	-40 (3)	-40 (5)
7	-	-	-	-	-	-	-	-43 (5)
8	-	-	-	-	-	-	-	-

Table 1: Decoupling (Bandwidth) in dB (kHz) between each coil in the 8-channel receive array helmet

Coil	Freq (kHz)	dB	Coil	Freq (kHz)	dB
1	276	-27	5	276	-35
2	276	-33	6	276	-29
3	276	-30	7	276	-30
4	276	-35	8	276	-27

Table 2: Tuning frequency (in kHz) and attenuation (in dB) for 8 receive coils in parallel array helmet

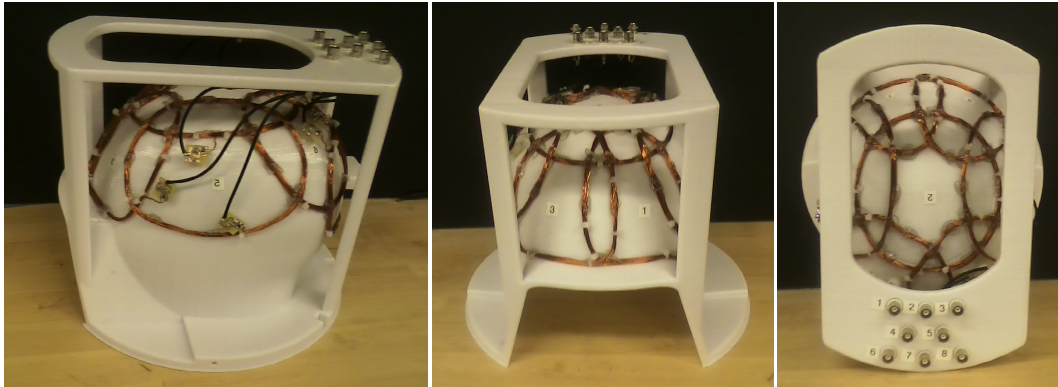


Figure 8: Photographs of the populated eight-channel human head “helmet” array. Shown L-R (a) side, (b) front, and (c) top views.

We were unsure if location of the tuning/match boards would impact our acquired signal. Two simple tests, one spectroscopy and one image-based, were performed with the board located a) 5 cm outside the loop b) next to but outside the loop and c) next to but inside the loop. Results are

shown Figure 9 and Figure 10. We thus concluded that the location of the tuning/match electronics board had no significant impact on acquired signal. It was therefore determined to place the board as close to the coil as possible, our typical lab protocol.

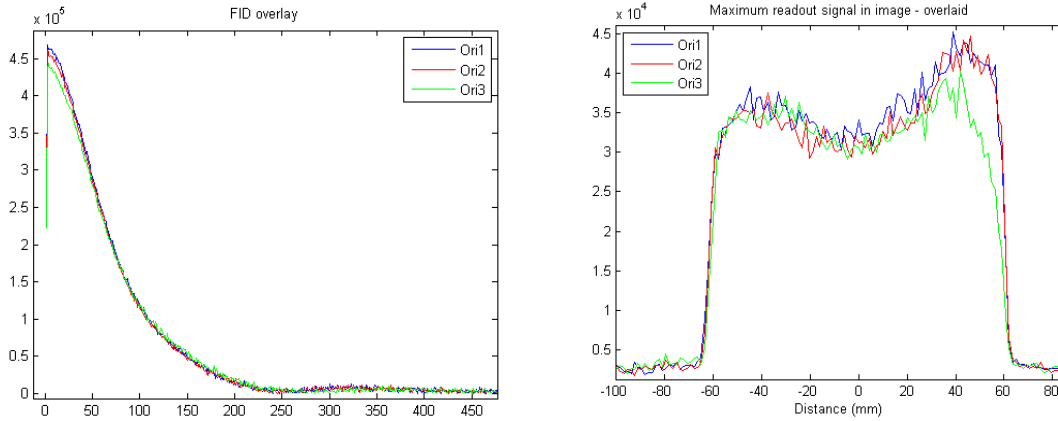


Figure 9: Results from testing tuning/match board location. **(Left)** Overlays of FIDs acquired from a single coil with the tuning/match board located 5 cm outside the loop (“Ori1”), next to but outside the loop (“Ori2”) or next to and inside the loop (“Ori3”). **(Right)** overlay of the maximum signal in each column of the images in Figure 10.

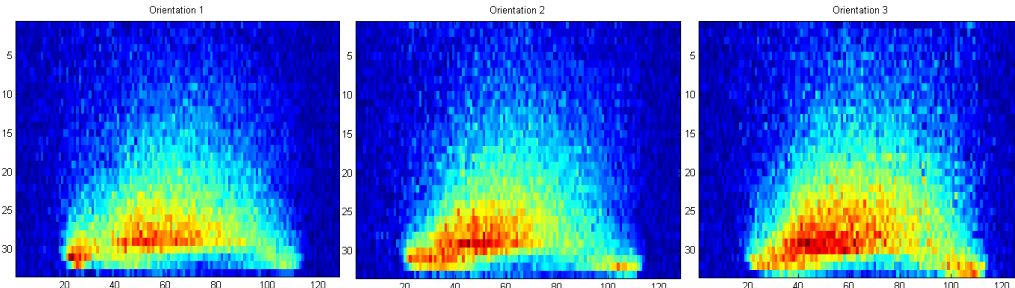


Figure 10: 2D test images acquired transverse from a single surface coil with the tune/match electronics board located in each of the three orientations described in Figure 9: **(Left)** Ori1, **(Middle)** Ori2, and **(Right)** Ori3.

Eight channel “helmet” receive array coil performance:

While the coupling between next-nearest neighbors elements is not ideal, it was decided to acquire images using the helmet to see what additional improvements were needed. Axial (Figure 11A) and sagittal (Figure 11B) images were acquired using a 3D b-SSFP sequence with 50% incoherent undersampling of k-space at 6.5 mT (276 kHz) in a healthy normal adult volunteer. Imaging parameters were: TR/TE = 33.2/21.6 ms, acquisition matrix = (64×64×9), voxel size = (3×3×6) mm³, number of averages (NA) = 200, and flip angle = 70°. The readout duration was 7.04 ms with a 9091 Hz bandwidth. The total acquisition time was 30 min. Both figures reveal recognizable anatomic features in the head including the skull, cortical structures (gyri/sulci) and the corpus callosum.

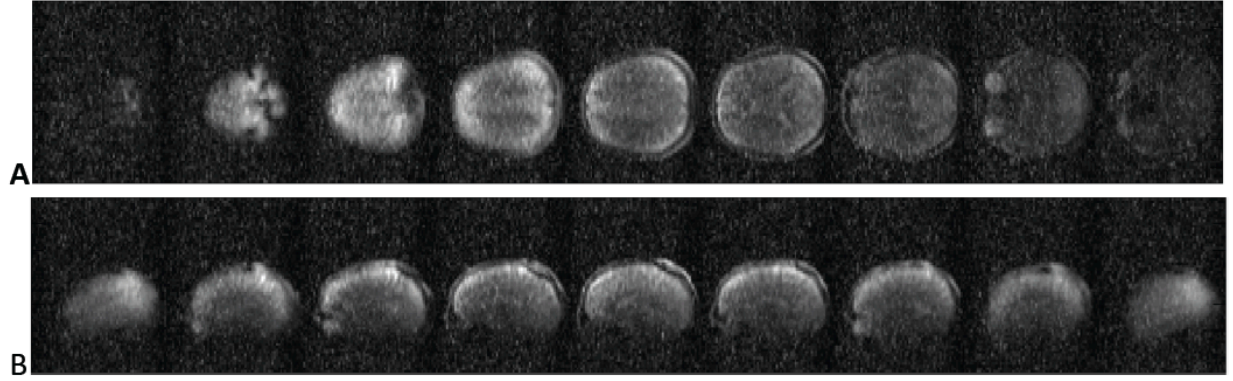


Figure 11: 3D b-SSFP performed in vivo in a human head in (A) axial and (B) sagittal orientation using the optimized 8-channel helmet array at 6.5 mT (276 kHz). Magnitude images are shown. Voxel size was $(3.3 \times 4 \times 17)$ mm³. Total acquisition time was 30 min.

It was observed that the image reconstructed by combining the images obtained from each channel were essentially the same as the image collected by the 14 cm coil positioned dorsal to all others. This is uncharacteristic of a phased array and indicates we had unintentionally created an array of mutually coupled receive coils. These types of arrays can generate coverage similar to an array coil while only connecting a single coil to the receiver [2]. This approach, though unintended, provides a potential solution to the next-nearest neighbor coupling issue and warrants further investigation.

Environmental coherent noise between channels

We noticed an increase in the noise floor of our acquired signal when imaging with the helmet array compared to our other coils. We hypothesize that our custom built subject bed was forming a conductive loop beneath the receive coils, and thereby was coupling noise from the gradient coils into to our helmet and introducing coherent noise to all channels. Our subject table is entirely non-magnetic, however, the aluminum framing beneath the wooden tabletop creates conductive pathways. We measured noise covariance matrices before and after breaking a conductive loop in the table beneath the receive array (Figure 12).

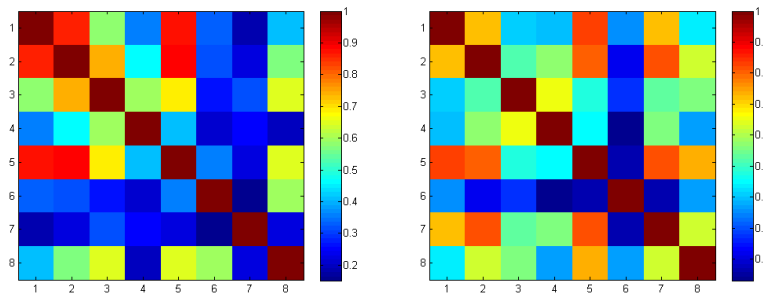


Figure 12: Noise covariance matrix before (A) and after (B) breaking a conductive loop in our subject table located beneath the receive array.

While these covariance matrices do show a high degree of coupling, the noise covariance matrix taken with the conductive pathway broken (Figure 12B) does better describe the observation that the 14 cm coil located dorsal to all others (i.e., channel 7) does in fact strongly couple with the other coils in the array (except for channel 6).

Effect of array coil orientation:

It was also noted that the images obtained from the lateral 14 cm coils were not identical even though the coils have approximately the same shape, size and orientation. In particular the right lateral 14 cm coil (“channel 5”) provides much lower SNR left lateral 14 cm coil (channel 4). Because the orientation of these two coils is the closest to being perpendicular to B_0 , some simple tests were conducted to determine the influence of coil orientation in the magnet on the acquired SNR. First, images were acquired in the original orientation and then rotated 90° so that the top of the helmet was perpendicular to B_0 (Figure 13). While not quantitative, the images suggest orientation of the coil inside the magnet may be affecting the performance of the individual coils.

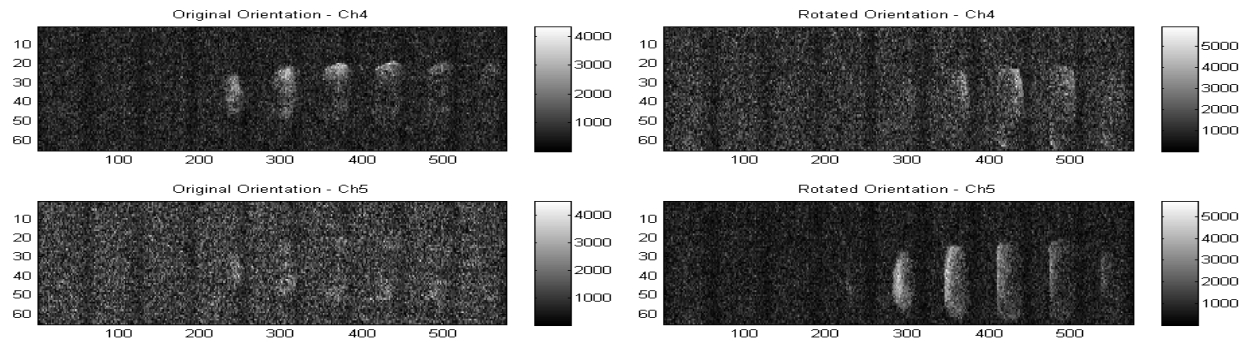


Figure 13: Images acquired by coil #4, the left lateral 14 cm coil (**top row**) and by coil #5, the right lateral 14 cm coil (**bottom row**). **Left** panel shows the images in the original orientation while **right** panel was acquired with the helmet rotated so that the 14 cm coil at the top of the helmet was perpendicular to B_0 . These images suggest that orientation of the coils inside the imager affects SNR.

As a next step, NMR spectra were collected from channel 5 in three different orientations (0°, 45° and 90°; rotation about B_1) first without- and then with the other coils connected. Connecting the coils allowed us to compare the effect of inductive coupling in addition to coil orientation. The spectra are overlain in Figure 14 and indicate that the orientation of channel 5 affects the acquired signal (blue line compared to green). Coupling has an additional detrimental effect to the signal (black compared to purple). Despite the coupling, channel 5 is much improved when rotated 90°. However, this would require that the human subject be forced to lay on their side during the imaging sequence—surely not an ideal situation. Additionally, rotating the helmet so channel 5 is in a more favorable position moves other coils into a more unfavorable orientation and the problem still exists. Two possible solutions are 1) retile the coils on the helmet array to

avoid the extreme left and right lateral positions or 2) implement a decoupling strategy. We have elected to pursue decoupling strategies.

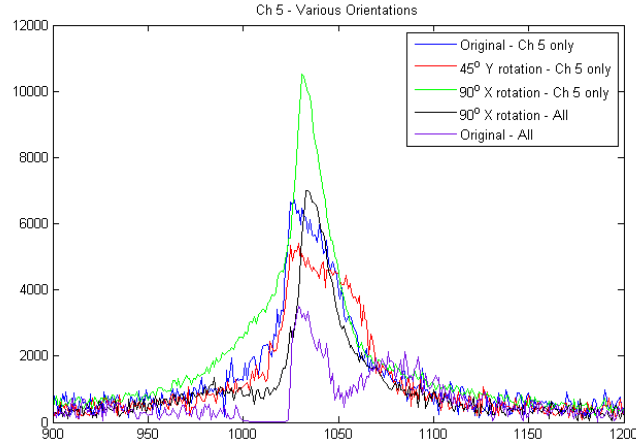


Figure 14: NMR spectra acquired from channel 5 in various orientations (rotation about B_1) with- and without the remaining array coils connected to the receiver ($50\ \Omega$ terminated). Signal amplitude is affected by both coil orientation and coupling.

Receive coil decoupling:

Despite the amount of inductive coupling between next-nearest neighbors, we are encouraged by the initial multi channel brain images of Figure 11. To improve image SNR, we began investigating ways to reduce noise and improve decoupling. We observed that the performance of each coil was strongly influenced by connecting next-nearest neighbors to the receiver ($50\ \Omega$ terminated). Spectra acquired from each coil as the other coils were sequentially added are shown in Figure 15. Channel 2, the 14 cm coil at the top of the helmet and symmetric about the midline, is geometrically decoupled from all coils except 7, the 14 cm coil dorsal to all others. Its FID, though affected by each coil, is only drastically changed by connected channel 7, its only next-nearest neighbor. In order to use all eight receive channels, a decoupling solution must be found.

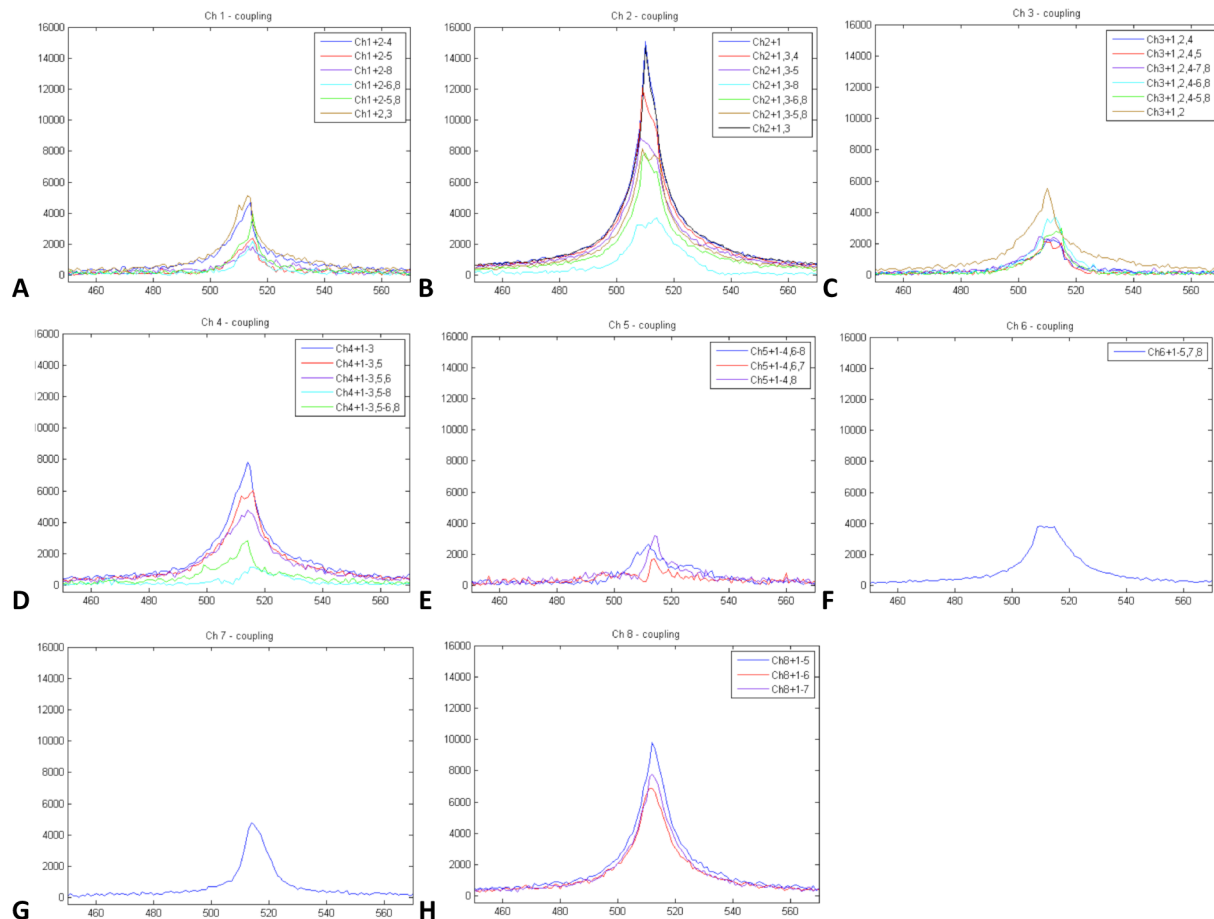


Figure 15: NMR spectra obtained from each coil (A-H) in the helmet array as they are sequentially connected to the receiver. Coils are added in order (channel 2 first, channel 7 last). Spectra are only slightly affected when a nearest neighbor is added, but is more heavily affected when a next-nearest neighbor is added.

At clinical MRI field strengths (i.e., nominal 100 MHz receive frequency), unwanted inductive coupling between receiver elements is typically prevented using preamplifier decoupling. While there is a wealth of in-house knowledge about this technique (in the Wald lab in particular), no commercial preamps exist suitable for the operational frequency our low-field imager. We are therefore currently investigating seven potential decoupling techniques in the hopes of identifying a simple solution at low field with the least impact on our signal chain, and enumerate them below.

- 1) Capacitive decoupling [3]. Capacitance is added between two coupled coils to cancel the mutual inductance of the coils.
- 2) Inductive decoupling [4]. As in capacitive decoupling, inductors are used between two coupled coils to cancel the mutual inductance of the coils. However, at 276 kHz, the in-

ductors may have to be physically large, and often will have a ferrite core not suitable for placement in the magnet.

- 3) Decouple (or “decorrelate”) in software [5], [6]. Theory suggests that if the noise covariance matrix is known, one should be able to tune and match the coils to a reasonable degree (say, at least -12 dB return loss when tuned to 276 kHz and matched to 50 ohm) and then the noise covariance matrix can be used to decouple the combined image created from the individual coils.
- 4) Decoupling matrix [3], [7]. With the full S-parameter matrix, it is possible to design a decoupling matrix. Values are determined through simulation using simplification assumptions. At 276 kHz it may be possible to build the matrix entirely using lumped elements.
- 5) High impedance preamplifiers [8], [9]. High impedance preamps essentially draw no current and make a pure voltage measurement of the NMR signal. This drives to zero the flux generated by each coil and the associated inductive coupling. We performed preliminary tests with two coils and a commercial research preamp (SRS SR560), however, were inconclusive.
- 6) Untuned coils. Untuned receive coils have essentially a Q of 1, and losses due to cross-coupling can be avoided at a cost of reduced induced signal voltage and increased noise voltage due to lack of off resonance rejection. Preliminary tests appear to confirm this.
- 7) Single channel receive. Coupling is an issue with our helmet because there are 8 elements. Surely, single channel receive as well as single channel transmit and receive are possible. Preliminary results using our 30 cm solenoid for both transmit and receive yielded poor SNR owing to low filling factor. In this configuration, obtaining useful images comparable to those obtained in the multichannel helmet would require many more acquisitions, increasing the scan time. For this case, the helmet even with coupling outperforms the solenoid. However, an optimized single channel helmet coil was also developed with very promising results. This work is discussed below in **Section 1C, p. 46**.

We have demonstrated that an optimized 8-channel helmet array combined with fast acquisition techniques and under-sampling strategies enables 3D imaging at very low field *in vivo*. With $(3.3 \times 4 \times 17)$ mm³ total voxel size we obtain 2 times greater spatial resolution than very recently published work using a SQUID detector in an ultra-low field MRI system with an 80 mT pre-polarization field [10]. In addition, our 3D dataset (9 slices) was acquired more than seven times faster than the single slice 2D brain dataset of the SQUID-detected work. Future work will focus on improved coil decoupling schemes.

TASK 1B: System control and image acquisition

We briefly mention that the bidirectional control and processing pipeline developed in the Rosen lab in Y1 and Y2 to pass data between TNMR and MATLAB has been extremely stable. Tecmag, Inc. has worked closely with us to quickly release maintenance upgrades of TNMR as minor issues arise.

We have been focused on improving imaging at a very fundamental level, *i.e.*, rigorous consideration of alternative methods of sampling k -space beyond the standard Cartesian strategy, including the highly efficient but notoriously problematic ‘spiral encoding’ technique. We have successfully implemented spiral imaging in the electromagnet LFI, and incorporated k -space trajectory mapping as a way to improve spiral image reconstruction artifacts.

Sequence design and optimization: spiral imaging in the electromagnet LFI

One of the main challenge of performing MRI at very low magnetic field can be seen as reaching high signal to noise ratio (SNR) per unit time. This is the main reason why our efforts have been focused on fast imaging techniques, such as balanced steady state free precession [11] (bSSFP). We have described our use of bSSFP in our previous reports, including its use in conjunction with undersampling and compressed sensing algorithms. Using bSSFP, we have achieved $2 \times 3 \times 9 \text{ mm}^3$ voxel size in a bell pepper in 1 min 12 s with 50% undersampling (see Year 2 Annual Report).

Sequence wise, non-Cartesian acquisitions of k -space also provide a rich field of investigation for fast imaging techniques [12]. In Cartesian acquisitions (Figure 16a), k -space sampling can be seen as acquiring lines of a 2D $M \times N$ matrix, where each line of M points is acquired for N phase encode steps. Thus the total acquisition time is weighted by the necessity of acquiring every line of k -space N times, which can be long depending on the size and/or the resolution of the image being acquired. Undersampling lines of k -space is a good way to shorten the total acquisition time, and we have successfully implemented this in the electromagnet LFI. However, undersampling requires the sampling of a certain minimum number of k -space lines in order to be efficient [13].

Spiral sampling provides the ability to acquire the entire k -space in a single readout following a spiral trajectory (Figure 16b), or in several interleaves (Figure 16c) in order to reduce the repetition time (TR).

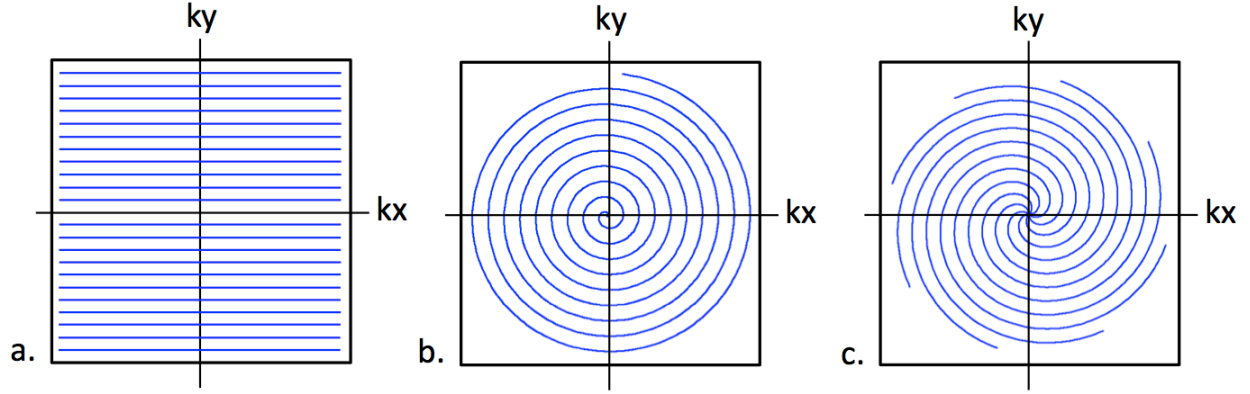


Figure 16: Comparison of a. Cartesian sampling versus b. and c. Spiral sampling of k -space (blue trace). k -space can be sampled within a single readout (b) or with several interleaves (c) in order to reduce TR.

Spiral MRI is also, by design, a good candidate for undersampling since each spiral samples the center of k -space, thus oversampling the latter, and emphasizing low spatial frequencies and image contrast. Spiral imaging can also be coupled to SSFP strategies for acceleration purpose. We describe here our implementation of 2D bSSFP with spiral sampling of k -space in the electro-magnet LFI.

Sequence design

A suite of MATLAB (Mathworks, Natick MA) tools was created in our laboratory to generate and transfer spiral gradient waveforms to our spectrometer software, TNMR, on our Tecmag Redstone console (Tecmag Inc., Houston TX). These tools were initially developed by Hargreaves *et al.* [14] and the source code is freely available online at <http://mrsrl.stanford.edu/~brian/mintgrad>.

This set of MATLAB scripts was customized and integrated to in-house codes in order to suit our low field MRI specifications and communicate with TNMR (Figure 17).

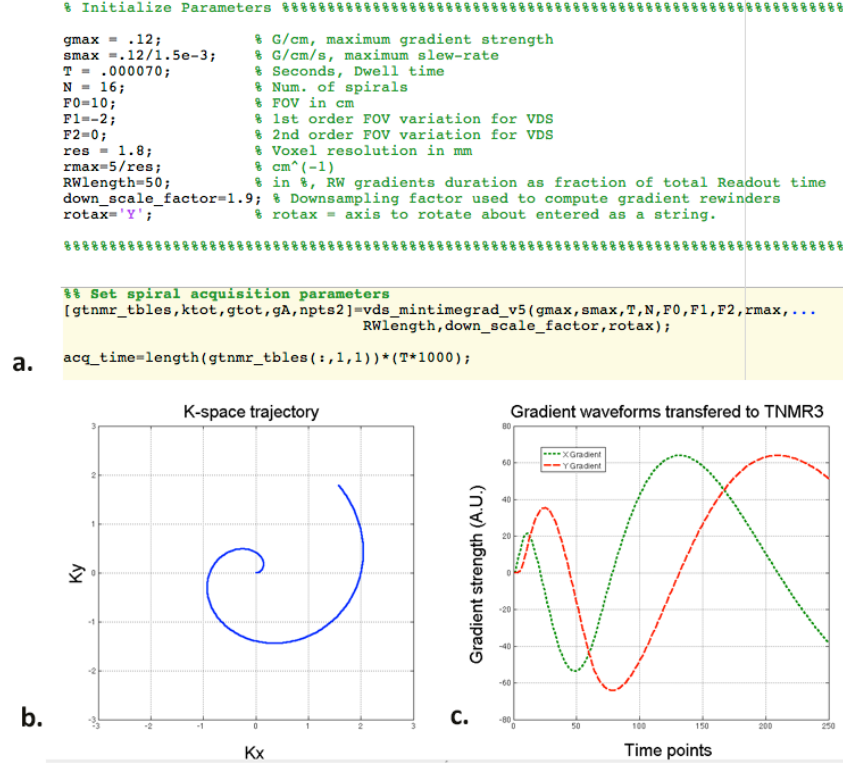


Figure 17: a. MATLAB code used to generate spiral k -space trajectories, b. Spiral interleaf (one of 16 spirals is shown), and c. corresponding gradient waveforms being transferred to the spectrometer software TNMR. The sequence parameters for this acquisition were: 16 spirals, maximum gradient strength = 0.12 Gauss/cm, Dwell time = 70 ms, Field of view (FOV)=10cm, voxel size = 1.8×1.8 mm².

Image reconstruction

Image reconstruction scripts were coded in MATLAB. At first, image reconstruction using gridding [15] was used. In this case, the acquired spiral trajectories are gridded onto a 2D matrix, correcting for oversampling of k -space center [16]. The image is then obtained from 2D Fourier transform of the gridded k -space. We then switched to non-uniform Fourier transform (NUFFT) reconstruction where the k -space spiral trajectories are directly fed to a NUFFT operator and also corrected from k -space center oversampling [17]. Reconstruction of spiral datasets was tested with several sets of simulated data (Figure 18). The simulated data was obtained by solving the Bloch's equations for sequence parameters being used for imaging. Off resonance and unbalanced gradients effects have been simulated too to have a baseline of expected image reconstruction artifacts resulting from those imperfections (Figure 19).

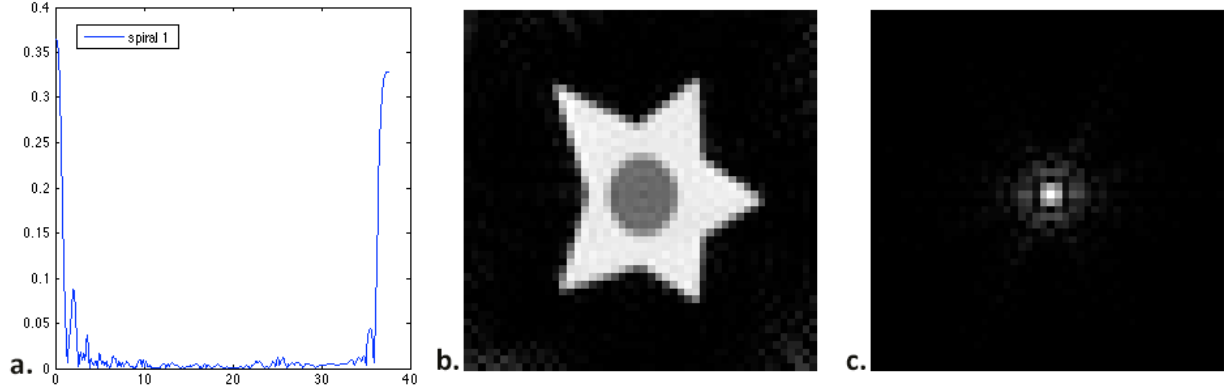


Figure 18: a. Simulated signal for spiral number 1 of 16, b. Reconstructed image from simulated dataset, and c. 2D inverse Fourier transform of the reconstructed image (gridded k -space). Sequence simulation parameters were: 16 Spirals, maximum gradient strength = 0.12 Gauss/cm, Dwell time = 70 ms, Field of view (FOV)=12cm, voxel size = 2.5×2.5 mm².

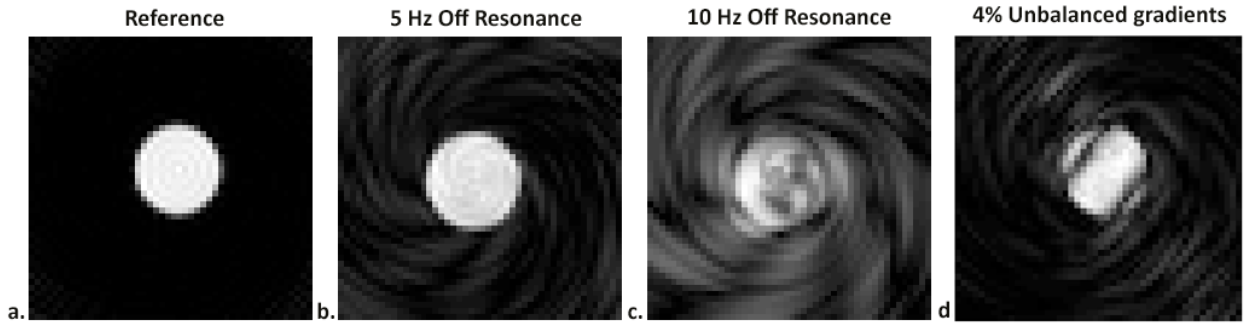


Figure 19: Images reconstructed from simulated datasets for a. 0 Hz, b. 5 Hz, c. 10 Hz off resonance spins, and d. on-resonance spins with 4% unbalanced gradients. The simulated object is a disk with homogeneous proton density. Spiral shaped artifacts appear around the object, alteration of the object shape and banding in the case of unbalanced gradients. Sequence simulation parameters were: 16 Spirals, maximum gradient strength = 0.12 Gauss/cm, Dwell time = 70 ms, Field of view (FOV)=12cm, voxel size = 2.5×2.5 mm².

Spiral acquisition strategies are very demanding as the gradient amplifiers are slewing at 100% duty cycle during readouts. Non-ideal performance of gradient amplifiers may induce lags or imperfections that cause the k -space trajectories to vary from their theoretical design. This requires mapping the actual k -space trajectories in order to prevent artifacts (resulting from non perfect k -space trajectories) on the reconstructed images.

We achieved k -space trajectory mapping as described by Duyn *et al.* [18]. For each gradient direction, an acquisition was performed with the slice select gradient of the corresponding direction turned on. The exact same scan was then repeated with the spatial encoding gradients

turned off. The k -space trajectories can be extracted from the measured phase difference between the two scans as follows:

$$\Delta\phi_r(t) = \int_0^t \gamma \cdot G_r(t) \cdot D_r \cdot dt = D_r \cdot k_r(t)$$

with γ = gyromagnetic ratio

$G_r(t)$ = spatial encoding gradient amplitude

r = encoding direction (x , y , or z)

D_r = distance of the slice to gradient isocenter

$k_r(t)$ = k -space trajectory.

The results are shown in Figure 20. The measured k -space trajectories were fitted with 9th degree polynomial fit and then used for reconstruction. The reconstruction results compared with our initial reconstruction are shown in Figure 21.

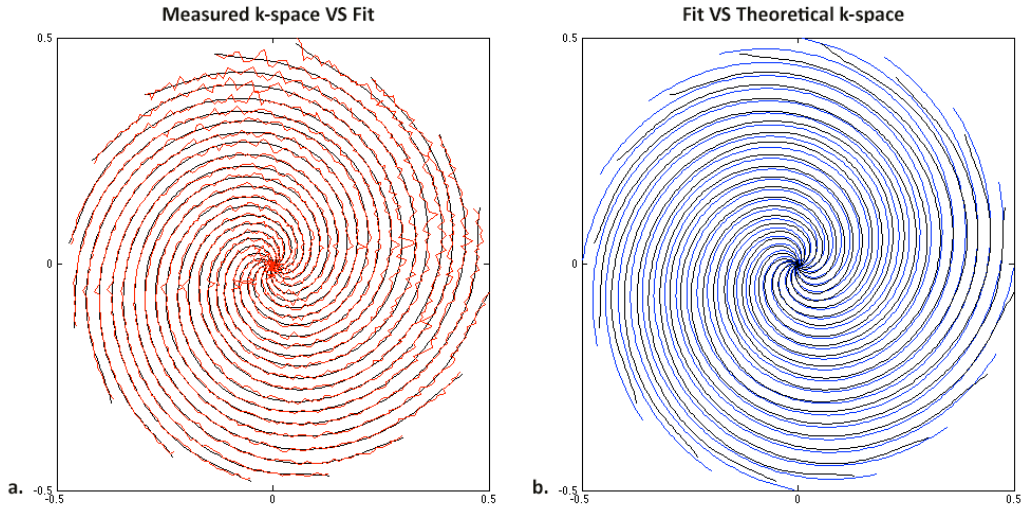


Figure 20: a. Measured k -space trajectories (red) superimposed with corresponding fit (black), b. Fit k -space trajectories (black) superimposed with theoretical k -space trajectories (blue).

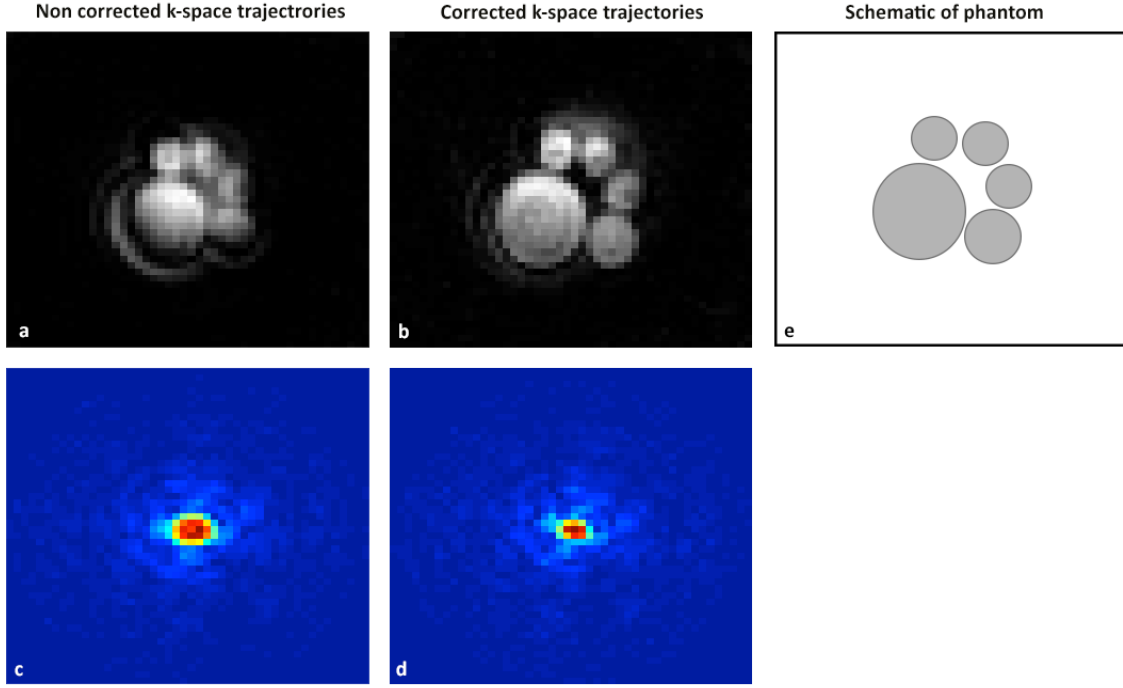


Figure 21: Reconstructed images from a. Uncorrected k -space trajectories and b. Corrected k -space trajectories from fit (black line) shown Figure 5. Corresponding reconstructed k -spaces from c. Uncorrected trajectories and d. corrected trajectories. Sequence parameters were: 16 Spirals, maximum gradient strength = 0.12 Gauss/cm, Dwell time = 70 ms, Field of view (FOV)=12cm, voxel size = 2.5×2.5 mm². A schematic of the imaged phantom is shown in e.

The use of corrected k -space trajectories clearly improves image reconstruction (Figure 21b) even though some artifacts remain. We need to further investigate the impact of field inhomogeneities and unbalanced gradients to improve our reconstruction but this really shows how slight variations in k -space can cause important distortions in the image domain. We also plan to add slice selection to our spiral imaging sequence to allow us to investigate multi-slice imaging techniques.

Sequence design and optimization: magnetic resonance fingerprinting at 6.5 mT

A key challenge in obtaining clinically relevant MRI images at low magnetic fields is the ability to acquire T_1 and/or T_2 relaxation-weighted images, and thereby provide contrast to different types of tissue. Typically, gradient-echo and spin-echo sequences are used to obtain relaxation-weighted images, but these types of imaging experiments become prohibitively time consuming at low magnetic fields where signal averaging is required. The fast imaging MRI sequence that has become the workhorse in our laboratory, b-SSFP, is time efficient, but results in a spin-density weighted images and does provide much soft tissue contrast. We have investigated a new strategy to provide contrast based on b-SSFP called “magnetic resonance fingerprinting” (MRF) [19], and have successfully implemented it at 6.5 mT.

A recent paper has proposed a new imaging technique termed “magnetic resonance fingerprinting” (MRF) [19]. Unlike **all** other MRI sequences, a MRF acquisition creates a rapid time series of low quality images. Each image is created with a pseudorandom flip angle and repetition time. The purpose of using a randomized sequence is to generate a unique signal trajectory over the time series of images. The signal magnitude for each voxel in time is determined by the sample relaxation properties for that voxel, and importantly, can be accurately simulated by Bloch simulations. In MRF, a large “dictionary” of simulated signal trajectories is built by performing Bloch simulations for all possible relaxation and off resonance values that are possible for the particular sample. The data acquired with the pseudo-random sequence is compared to the dictionary, and the best match is chosen, giving T_1 , T_2 , and the off resonance frequency for that voxel. Thus, in a single fast and efficient sequence, T_1 , T_2 , spin density, and B_0 maps are all obtained. MRF has the potential to allow low magnetic field scanners to produce clinically relevant images *without* hyper-polarization because each image in the time series does not need to be of high quality. The pseudo-random sequence and pattern matching algorithm used in MRF is fairly robust to noise and under-sampling artifacts, and thus the goal of an MRF sequence is to generate unique signal trajectories in the shortest amount of time possible.

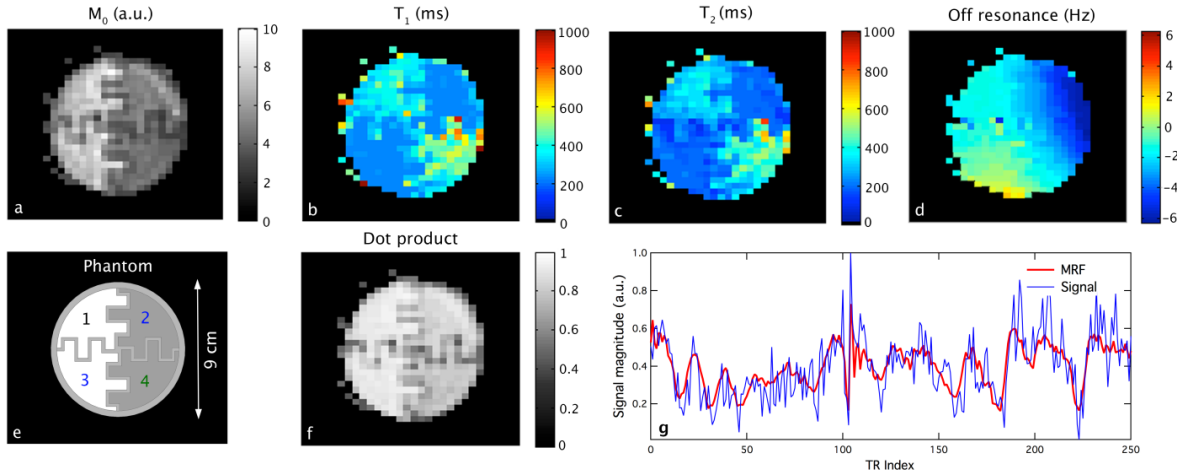


Figure 22: Initial MRF results obtained in 16 minutes at 6.5 mT. The four compartment liquid filled phantom is illustrated in (e). The vary in volume and relaxation properties. After matching each voxel to the dictionary, the M_0 , T_1 , T_2 and off resonance maps (a-d) are immediately obtained. The confidence of the match is given by the dot product (f) for each voxel and is used to threshold the data. The magnetization trajectory for a typical voxel is shown in (g) along with the simulated trajectory of its best match.

Our initial results implementing MRF in the 6.5 mT LFI are shown in Figure 22. We note here that to the best of our knowledge we present here the first implementation of MRF outside of the original manuscript of reference [19], and the first results at low field. The four compartments of the phantom were filled with varying volumes and solutions of varying relaxation times to test the ability of MRF to determine the spin density, T_1 , T_2 , and off resonance frequency of each

compartment. The set of four images in Figure 22 **a-d** were acquired in just 16 minutes at 6.5 mT. Each image gives unique information about the sample properties, in contrast to a traditional b-SSFP sequence where only M_0 (Figure 22**a**) is acquired. For example, Figure 22 **b-c** clearly shows that compartments 1 and 3 (2 and 4) have different relaxation properties. Also shown in Figure 22**g** is the first 250 time points (out of 1000) of a signal trajectory and its best MRF dictionary match. While the data is indeed noisy due to the small signal magnitude at 6.5 mT, it clearly follows the predicted trajectory from the Bloch simulation.

Despite our very encouraging initial MRF results, there are several challenges to overcome. The algorithm to match the data to the dictionary assumes that each voxel is homogenous. If a voxel contains multiple components, the signal trajectory will not be in the dictionary and can thus lead to incorrect assignment of relaxation properties. It is therefore critical to obtain sufficient resolution such that partial volume effects are minimized. This was obtained in Figure 22 by designing a phantom that was homogenous in the out of plane dimension so a 2-D projection image could be performed. Future MRF efforts will focus on implementing slice selection at 276 kHz to reduce partial volume effects. There are no active, high-power, switches available at 276 kHz and thus we have to carefully calibrate our hardware to pre-distort shaped pulses for slice selection. Accurate calibration will be important because MRF relies on matching data to a simulated trajectory, and thus, hardware imperfections will lead to matching errors.

Sequence design and optimization: 8 channel image acquisition and reconstruction

Image acceleration via SENSE: migration to a new optimized reconstruction code:

Image acceleration via SENSE implies coherent undersampling of k -space, which results in an aliased image. In order to unfold the image, SENSE reconstruction uses the information gathered from different coils in an array to solve a set of over-determined linear equations.

When performing SENSitivity Encoding (SENSE) at typical clinical field strengths, noise is body-dominated and therefore correlated between all coils in a parallel imaging array. In this particular regime, the coil sensitivity profiles change as the coils load differently from a sample to another. Therefore, when performing SENSE at high magnetic fields the sensitivity maps needed to unfold a SENSE accelerated image must be calculated for each imaged object, thus requiring the acquisition of a fully sampled dataset (spatial resolution may change) prior to the acquisition of an accelerated image.

In the Johnson noise dominated regime, there is typically no correlated noise between coils in the array. Additionally, in this low-frequency regime, inductive detection coils do not ‘load’, that is, the resonant properties are not affected by the presence or details of the imaging sample. Because

of this, a sensitivity map obtained on a homogenous phantom should be able to be used to unfold any SENSE images collected with the array in the LFI.

In our previous work, optimal results (*i.e.* image unaliasing) were obtained when our sensitivity map was generated from a fully sampled image of the actual imaged phantom and not from a homogeneous non-structured phantom. Though a promising first step, this was not the expected functionality. After deeper investigations we concluded that the code we were using was not creating sensitivity maps properly. A new code developed with MATLAB was used and, after optimization, was able to unfold our SENSE accelerated images using sensitivity maps obtained from a homogeneous phantom (Figure 23D). An important detail for successful image reconstruction was to make use of a large homogeneous phantom for the calculation of the B_1 sensitivity maps, at least 3 pixels bigger than the imaged structured object (for a given field of view). Typically, the same reconstruction code used with a homogeneous phantom with exact same size as the imaged object will result in artifacts from the edges. The homogeneous phantom used is shown in Figure 24. The sensitivity profiles acquired from each element in our 8 channel parallel array are shown in Figure 25.

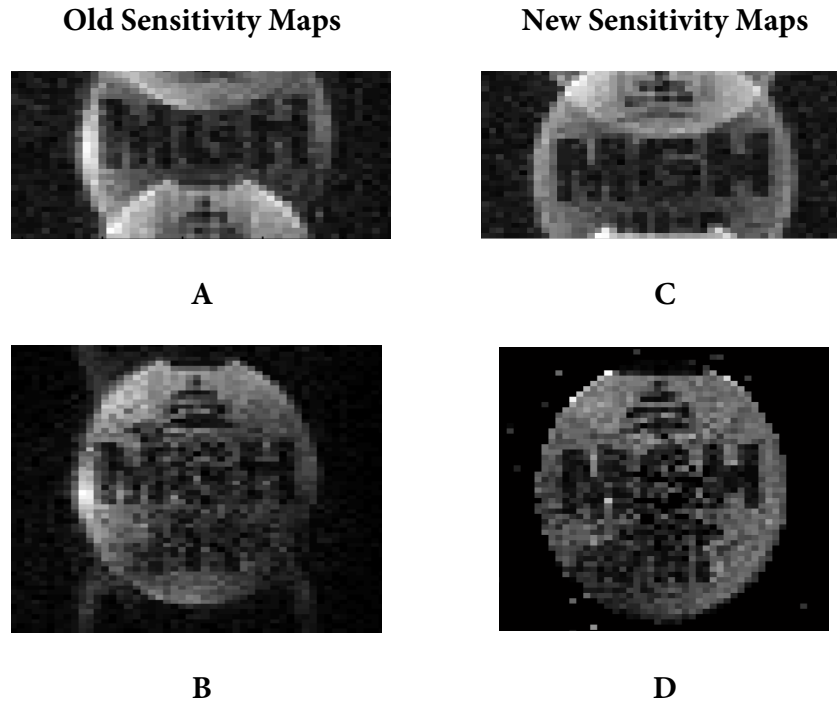


Figure 23: Accelerated aliased images (A, C reduction factor $R=2$) and reconstructed (B,D) images of the MGH/MIT phantom. Images B and D were unaliased using sensitivity maps generated from a large, homogeneous phantom. Image B was generated using sensitivity maps generated from a homogeneous phantom with our prior code and D was generated using our new code. Of importance to the present work is the absence of aliasing in the background of D. All images acquired at 6.5 mT.



Figure 24: Large homogeneous bottle phantom (filled with blue CuSO_4) for use in generating sensitivity maps, inserted into the eight channel array coil. This configuration is preferable because it completely fills the array, and allows coil sensitivity profiles to be measured outside the normal field-of-view of the object to be imaged.

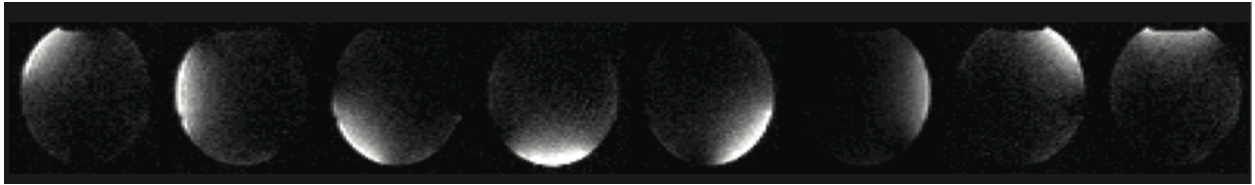


Figure 25: Sensitivity profiles of each element in the 8 channel parallel array using the large homogeneous bottle phantom of Figure 24. All images acquired at 6.5 mT.

Development of new phantoms:

New phantoms were designed and 3D printed for use with the parallel receive array. Figure 26 A, B incorporates structures with varying thicknesses and shapes in the bottom to assess the ability of SENSE applied at 6.5 mT to preserve the object features as a function of the undersampling rate. The same phantom incorporates ramps to evaluate the performance in 3D. The second phantom is based on the Harvard *Veritas* crest (Figure 26C). The fully sampled MRI images of these phantoms are shown in Figure 26 D–F.

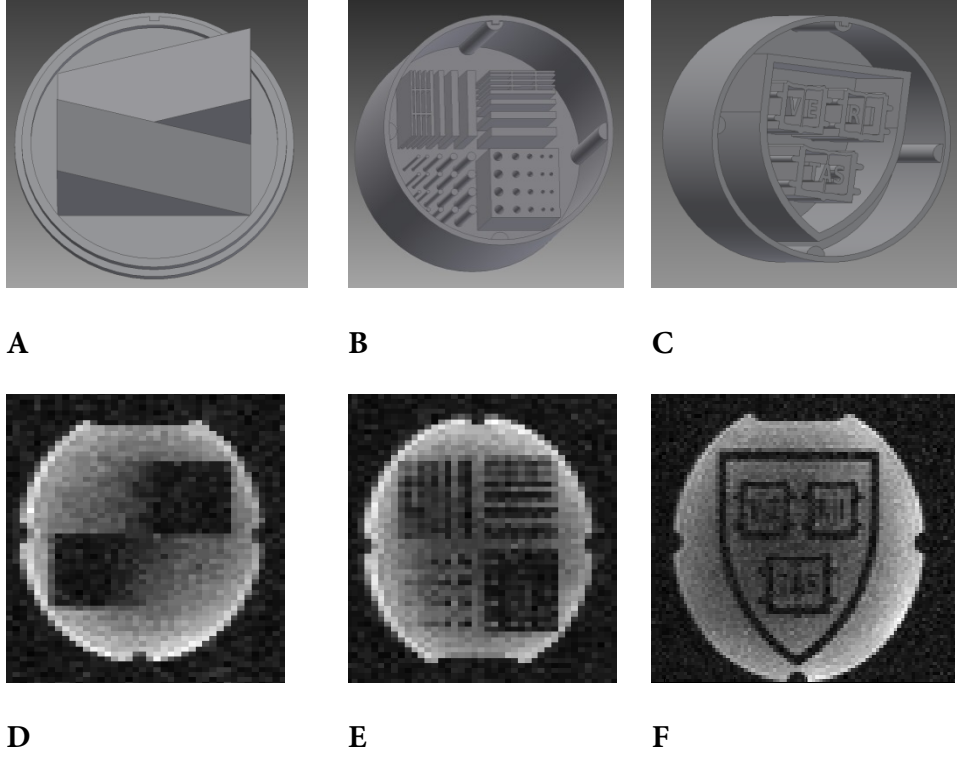


Figure 26: Drawings (A-C) and fully sampled images (D-F) of two new phantoms for parallel imaging testing purposes: the two-part structured phantom (lid shown in A and body in B) and the Harvard *Veritas* crest (C,F). Images acquired at 6.5 mT.

Acceleration imaging results in the new structured phantoms:

Images of one of the new phantom were acquired with $R=1$ (*i.e.*, no acceleration) and $R=2$ (acceleration factor=2) and are shown in Figure 27 (A, B). Cartesian acquisition of k -space was used with $\text{FOV}=192 \times 169 \times 256 \text{ mm}^3$, acquisition matrix= $64 \times 65 \times 9$ for $R=1$, acquisition matrix= $64 \times 33 \times 9$ for $R=2$, $\text{TE/TR}=14/29 \text{ ms}$, number of averages (NA)=60. The readout duration was 7.04 ms with a total readout bandwidth of 9091 Hz. Total acquisition time was 17 min for $R=1$ and 8.5 min for $R=2$. Multi-channel image data was combined with a sum-of-squares method [8]. We tested the ability of our new SENSE code to reconstruct aliased images by deleting alternate lines of the fully sampled k -space data (*i.e.*, $R=2$) and using the MATLAB reconstruction code to it generate the image shown in (Figure 27 C). The image shown in Figure 27D is an $R=2$ reconstruction from actual accelerated data.

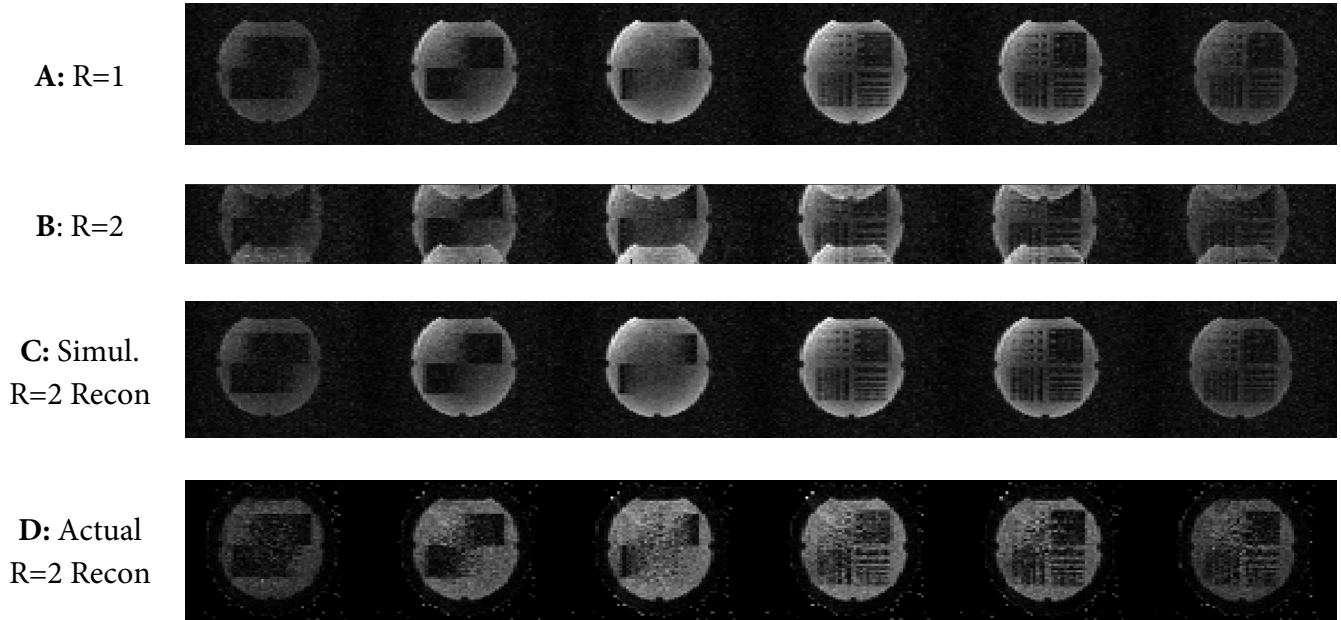


Figure 27: Six of the nine acquired slices in (A) the fully sampled phantom, (B) R=2 before applying SENSE reconstruction, (C) R=2 simulated from fully sampled dataset and (D) actual R=2 results after SENSE reconstruction.

Halbach array LFI: Imaging in the rotating permanent magnet:

Single channel imaging

To understand the details of the image acquisition process using the automated magnet rotation as described above on page 7, we acquired images using the solenoid RF coil for both transmit and receive. Because the coil's sensitivity is relatively uniform over the FOV, it allows us to isolate the effect of the Halbach field map on the quality of the reconstructed images before moving on to the more complex case of multiple receive coil sensitivity profiles. Using the solenoid coil for TX and RX, we obtained our best images to date (**Figure 28, Figure 29**). Images were acquired using a thin circular phantom containing the water-filled letters "MGH". Since only one coil was used, the letters are aliased through the origin, as expected from the non-bijective mapping of the multipolar (quadratic) encoding field. The fact that the "real" letters are sharper than the ghosts can be attributed to the relatively small linear field components (impurities) in the Halbach field.

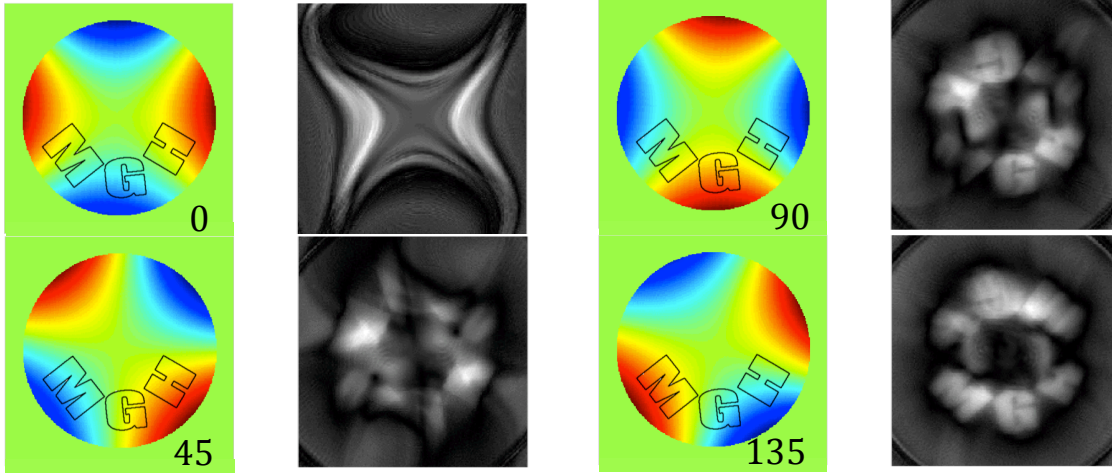


Figure 28: Image estimates at various points in the image reconstruction process. The estimator converges to the object as successively greater fractions of the data are processed. These images show estimators based on one back projection (at 0°) and then using $\frac{1}{4}$, $\frac{1}{2}$, and $\frac{3}{4}$ of the acquired data. This corresponds to rotation of the Halbach magnet over the ranges 0° , 45° , 90° , and 135° , respectively. Images were acquired from a 3D-printed phantom containing the water-filled letters “MGH”.

Figure 28 shows how the image estimate gradually takes shape during reconstruction. The estimator is updated using each basis function in the encoding matrix to enforce consistency with the acquired data. Back projection proceeds until all rows of the encoding matrix (and data points) are exhausted, completing one iteration through the matrix. With each iteration through the encoding matrix, the image converges closer to the least squares estimator to the object. As shown in **Figure 29**, image bias shrinks with each iteration, reducing the blurriness of the image features. However, since noise also grows with the number of iterations, an intelligent stopping point must be chosen at which object features are adequately resolved but noise has not been excessively amplified.

Reconstructed images from single-coil phantom dataset

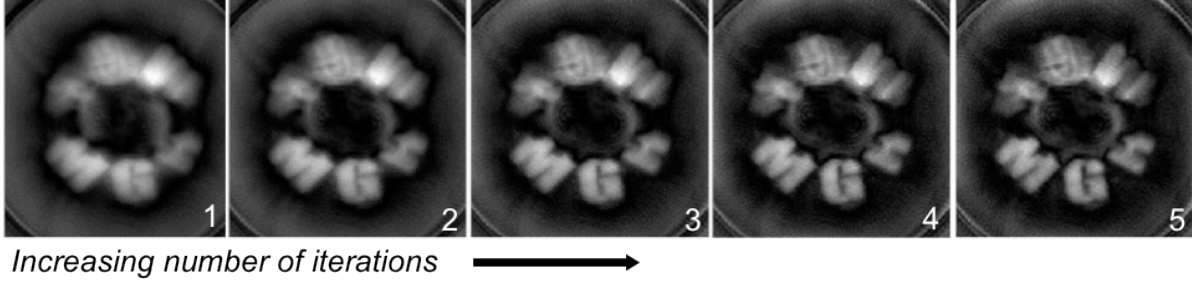


Figure 29: Reconstructed images from a single-channel (solenoid) dataset with 91 projection angles between 0 and 180 deg. Results are shown for differing numbers of iterations through the encoding matrix in the algebraic reconstruction. The images show the expected trade-off between noise and bias; as the algorithm iterates further, the object features become less blurry but the image also grows noisier.

When the multi-coil datasets are reconstructed in parallel using each coil’s spatially-varying sensitivity, the image quality deteriorates severely. This indicates that there is systematic error in our model of B_I , which describes the RF receive sensitivity of each surface coil over the FOV. In conventional MRI scanners, B_I is measured by acquiring an image with each coil and dividing them by the image formed using a uniform transmit volume coil. However, since linear gradients are not included in the Halbach scanner, this approach can not be used. Alternatively, we are approximating the coil sensitivities using the Biot-Savart Law (**Figure 30**) under the assumption that near-field wave behavior is minimal at the imaging frequency (3.3 MHz).

Adding further complexity, the surface coil sensitivity varies in between projections as the B_0 rotates within the transverse plane. Each coil only detects signal using field components that are perpendicular to the B_0 vector. Because of this, the shape of the B_I field changes dramatically with the B_0 orientation; for instance, when B_0 points through the center of a coil, the sensitivity resembles a “donut” shape, whereas for B_0 oriented tangential to the coil, the sensitivity is a more typical profile that decays with distance from the coil.

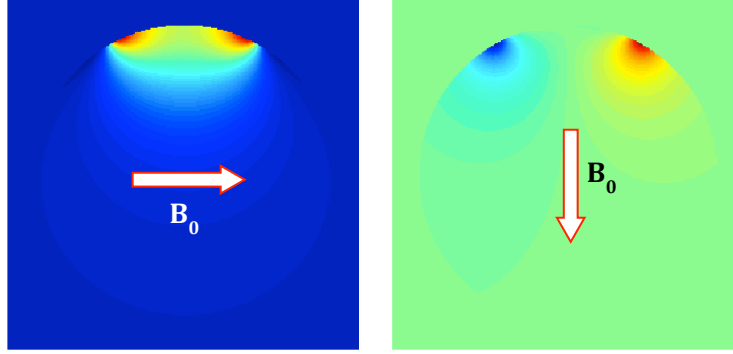


Figure 30: The real part of the B_1^- field of a receiver surface coil approximated using the Biot-Savart Law. The coil sensitivity changes as the transverse B_0 field rotates within the imaging plane. Accurate reconstruction requires that the correct coil profile be used for each acquired projection described by the encoding matrix. The poor quality of multi-coil reconstructions indicates the presence of systematic error in our present model of the B_1^- fields.

Multi-coil imaging and reconstruction

Our previous multi-coil datasets suffered from severe artifacts due to the use of inaccurate surface coil sensitivity maps. In conventional MRI, a bootstrap approach is used whereby surface coil receive sensitivities (B_1^-) are acquired by imaging a phantom sample with each coil using the scanner’s own switchable gradients for spatial encoding. This is not possible on the Halbach scanner, as the imaging gradients are intrinsic to the magnet and not switchable. Making matters more complex, the surface coil sensitivities change as B_0 rotates within the transverse plane, since only the coil field component perpendicular to B_0 contributes to the acquired signal.

At the frequency used for the Halbach experiment (3.3 MHz), the coil RF field is taken to be a close approximation to the magnetostatic limit. However, it is difficult to know a priori how to set the phase of the B_1^- field for each coil. To calibrate the spatially-varying phase of the coils, data were acquired from a small “point source” (partially-filled 9 mm dia. NMR tube) at a known location near a receive coil. An imaging sequence was then run at 91 rotation angles of the Halbach magnet. At each angle, the echo signal was Fourier transformed to generate a 1-D projection. The phase of this projection was compared to the phase for a projection calculated using the Biot-Savart law B_1^- coil sensitivity. Based on this comparison, the real and imaginary parts of the coil profile were heuristically adjusted until agreement was achieved with the data.

The phase of the projection was found to alternate between $+90^\circ$ and -90° , with a transition as the B_0 vector reaches the angle where it is perpendicular to the coil loop. The phase of B_1^- depends on the arctangent of the two components of B_1 that are perpendicular to B_0 . We realized

that the alternating phase was caused by the fact that the term in the arctangent denominator, which points along the Halbach axis, is virtually zero in the central plane where we perform imaging. This results from the symmetry of the coil loops about this plane.

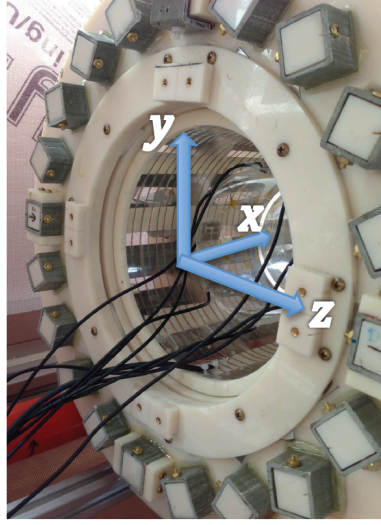


Figure 31: Coordinate system used to describe coil profiles. The system rotates between signal readouts such that z always points along B_0 .

In the end, good agreement between simulated and acquired projections was found as follows, using the coordinate system shown in Figure 31. First, the 3D vector magnetic field map for each coil, \mathbf{B}_i , was calculated using Biot-Savart. Second, for all n rotation angles of vector background field \mathbf{B}_0 , the component parallel to \mathbf{B}_0 was subtracted from \mathbf{B}_i :

$$\mathbf{B}_{1n}^\perp = \mathbf{B}_1 - (\mathbf{B}_1 \cdot \mathbf{B}_{0n}) \mathbf{B}_{0n}$$

Third, the angle was calculated between \mathbf{B}_0 and the perpendicular \mathbf{B}_i field:

$$\theta_n = \sin^{-1} \left(\frac{|\mathbf{B}_{1n}^\perp \times \mathbf{B}_{0n}|}{|\mathbf{B}_{1n}^\perp| |\mathbf{B}_{0n}|} \right)$$

where $\mathbf{B}_{1n}^\perp = \mathbf{B}_{1n}^{\perp,x} \hat{\mathbf{x}} + \mathbf{B}_{1n}^{\perp,y} \hat{\mathbf{y}}$ with x pointing along the Halbach axis, y pointing perpendicular to B_0 in the imaging slice, and z pointing along B_0 . Finally, the complex B_1^- sensitivity was found using the magnitude of \mathbf{B}_{1n}^\perp and the phase set by the relative amounts of \mathbf{B}_{1n}^\perp along x and y :

$$\mathbf{B}_{1n}^- = |\mathbf{B}_{1n}^\perp| e^{-i \tan(B_{1n}^{\perp,y}/B_{1n}^{\perp,x})} = |\mathbf{B}_{1n}^\perp| e^{\frac{-i\pi}{2} \text{sgn}(\theta_n)}$$

Since \mathbf{B}_i along x is essentially zero in the symmetry plane of the coil, this expression reduces to simply the sign of the angle θ_n . The variation in a single coil's \mathbf{B}_i^- as a function of \mathbf{B}_0 angle is illustrated in Figure 32.

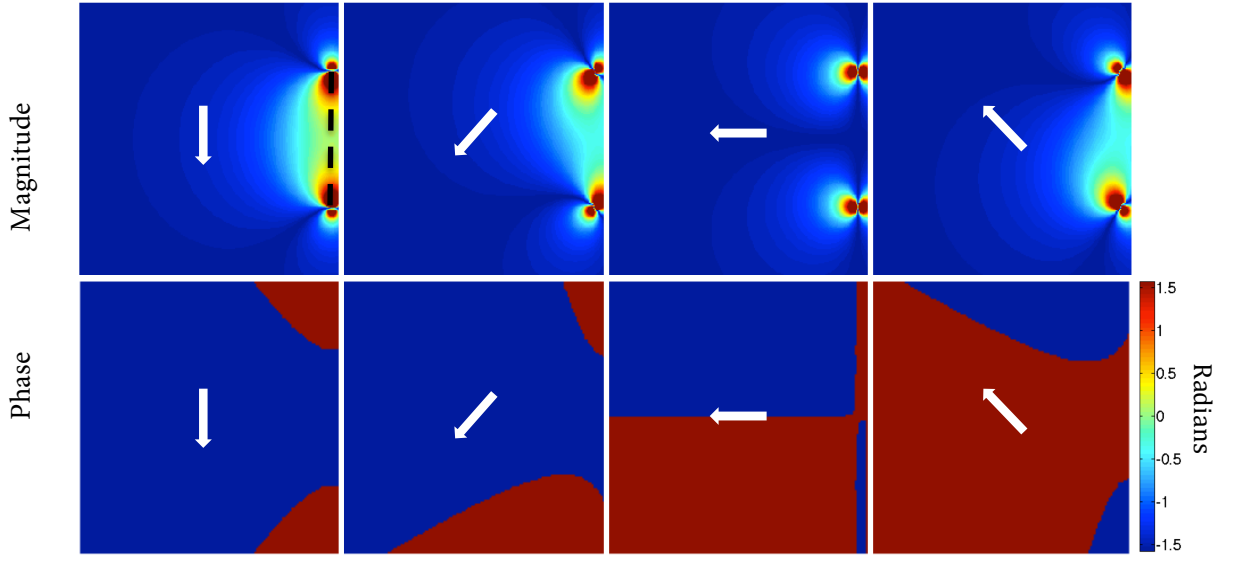


Figure 32: Biot-Savart calculation of coil \mathbf{B}_1^- magnitude and phase for a single representative surface coil located at the right side of the FOV (position marked with black dotted line). The arrow shows four representative orientations of \mathbf{B}_0 at different times during data acquisition. Image reconstruction requires accurate coil sensitivity profiles for each \mathbf{B}_0 angle used in the experiment.

When \mathbf{B}_0 points through the coil, the sensitivity profile resembles a “donut” pattern, providing low sensitivity in the center of the FOV. As expected, maximum signal sensitivity occurs when \mathbf{B}_0 is oriented parallel to the plane of the coil loop.

Equipped with more accurate coil profiles, we were able to achieve huge improvements in our multi-coil datasets. Previously, our most compelling images were acquired using a single uniform-sensitivity receive coil, leading to “PatLoc ghosting” of signal through the isocenter of the nonlinear encoding field [20]. With the new coil profiles, however, we were able to obtain multi-coil images with the PatLoc ghost removed (Figure 33). Coils on opposite sides of the FOV were successfully used to disambiguate signals lying along the same isocontours of the nonlinear encoding field.

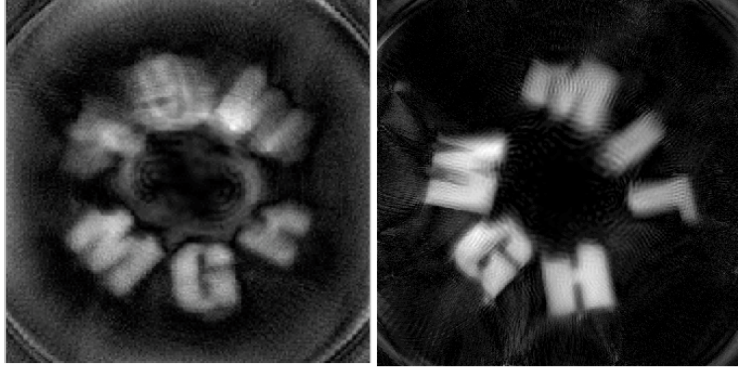


Figure 33: Single-coil image (left) of “MGH” phantom shows the expected pattern of aliasing through the isocenter caused by the nonbijective mapping of the nonlinear encoding field. By contrast, a 7-coil image (right) resolves this aliasing when properly calibrated coil sensitivities are used. Black regions at the top of the letters reveal where water leaked out of the phantom. Resolution at the edge of the FOV in the 7 coil image is 0.625 mm.

Halbach array LFI: assessing resolution

Tuned-up coil sensitivities and more accurate stepper motor rotation contributed to substantial improvements in image quality. This prompted investigation into other sources of systematic error that may continue to cause artifacts and loss of resolution. To establish an ultimate performance goal, we used the acquired Halbach encoding field to simulate the “ideal” image quality we could theoretically achieve in the absence of systematic errors (Figure 34). With a grid phantom serving as a reference, forward projection was used to simulate a signal with the parameters used in our previously acquired data. Image reconstruction was then performed using the iterative matrix solver used in the experiments.

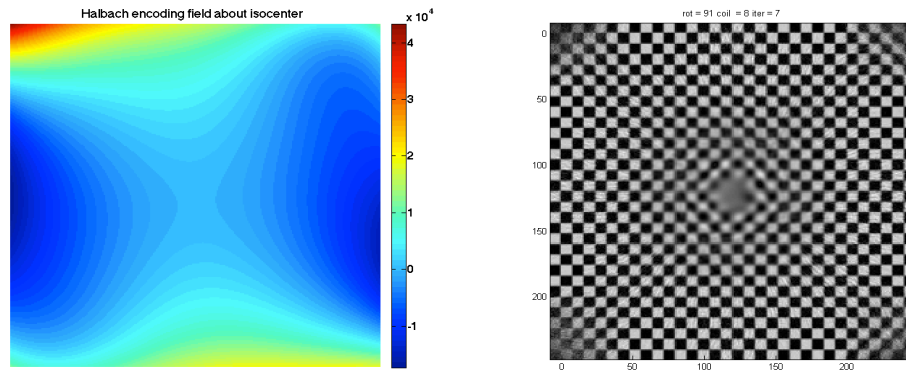


Figure 34: Noiseless simulation of a 5mm grid numerical phantom showing the ultimate resolution possible with existing experimental protocol in the absence of systematic errors. Outstanding resolution at the periphery gradually gives way to a blurry “PatLoc hole” at the center of the image. Simulated acquisition parameters: 7 surface coils, 91 projections angles, 256 readout points.

As expected, we found excellent resolution at the periphery, with gradual blurring toward the flat region of the encoding field at the center of the FOV (so-caled “PatLoc hole”) [20]. However, when we acquired data with the same parameters on an experimental grid phantom, image resolution fell far short of that predicted in the simulation (Figure 35). This suggests that additional systematic errors remain in the experiment, possibly including the following:

- a. Thermal drift
- b. Inaccuracies in the encoding magnetic field map
- c. Through-plane spin dephasing
- d. Additional phase accumulation by off-resonance spins during RF excitation due to finite RF pulse bandwidth

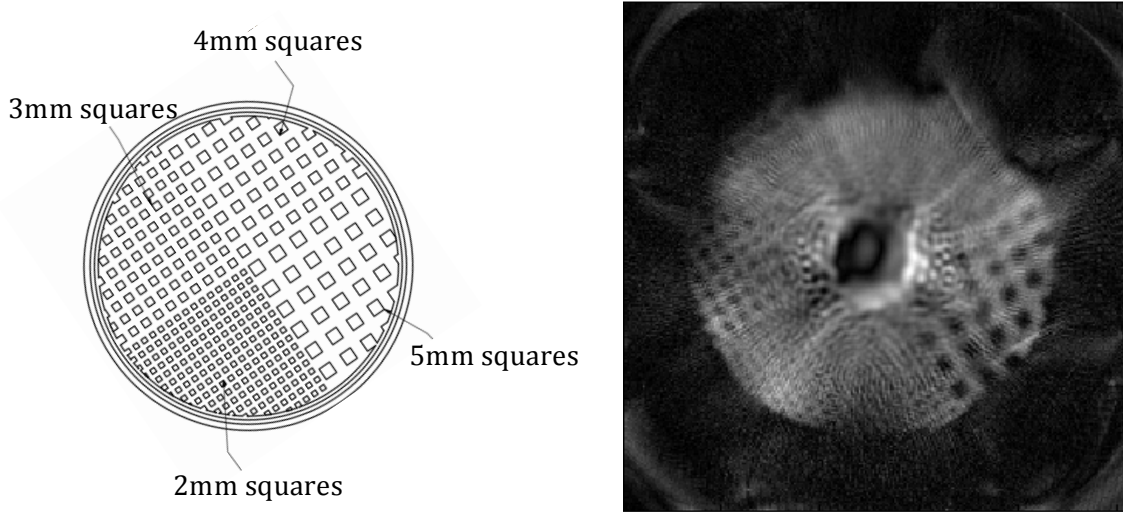


Figure 35: Grid phantom (left) designed to test the resolution of the Halbach scanner. The image reveals some of the grid structure, with expected resolution loss near the center, but the variation in image quality over the FOV shows that improved field mapping is required. Some resolution is lost near the top of the phantom due to the absence of a receiver coil in this region; this will be corrected in future work.

Our first un-aliased 2D images of phantoms using the Halbach portable brain scanner prototype are shown in Figure 36. These images were made possible by (1) improved stepper motor control of the Halbach rotation angle during data acquisition and (2) higher-fidelity calculations of the spatially-varying coil sensitivities used for signal reception and for unwrapping voxels that alias atop one another in the nonbijective mapping of the nonlinear encoding field.

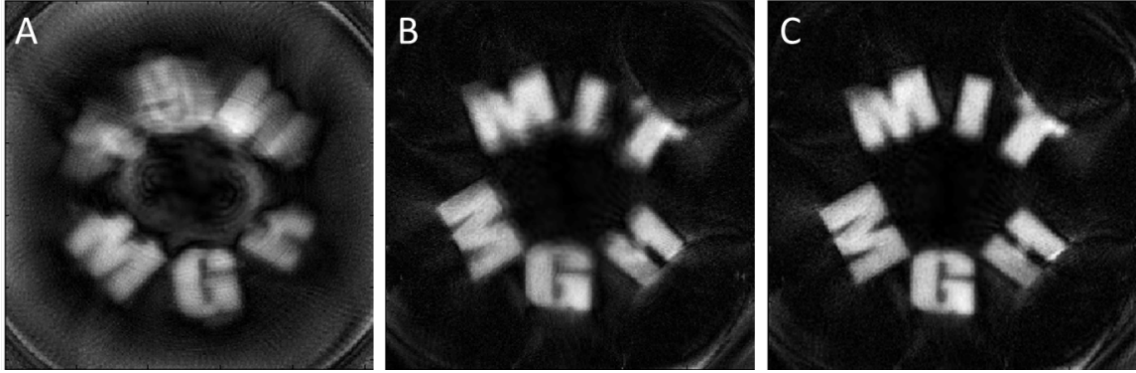


Figure 36: Images acquired using 3D-printed test phantom with 91 rotations of the magnet, FOV=16cm, BW = 40 KHz, readout pts=256, TE/TR=8/550ms. (A) Image acquired with uniform transmit coil show aliasing that is resolved when 8ch receive array is used (B) Accounting for magnet temperature drift with navigator field probe provides further improvement (C). Acquisition time = 66 min. for multi-coil data.

Our first 2D images of a “biological” is shown in Figure 37, where a lemon slice was imaged with a multi-coil RF receive array and either 91 or 181 projection angles. While the resolution varies inversely with distance from the center, as expected from the shape of the encoding field (Figure 37C), at a distance of 4 cm from isocenter the resolution approaches 1–2 mm in-plane, which is well within the range of clinically-useful imaging protocols. The acquisition time of 93 minutes could be shortened to 15 minutes by acquiring data in parallel from all 8 receive coils using a multi-channel RF receiver system.

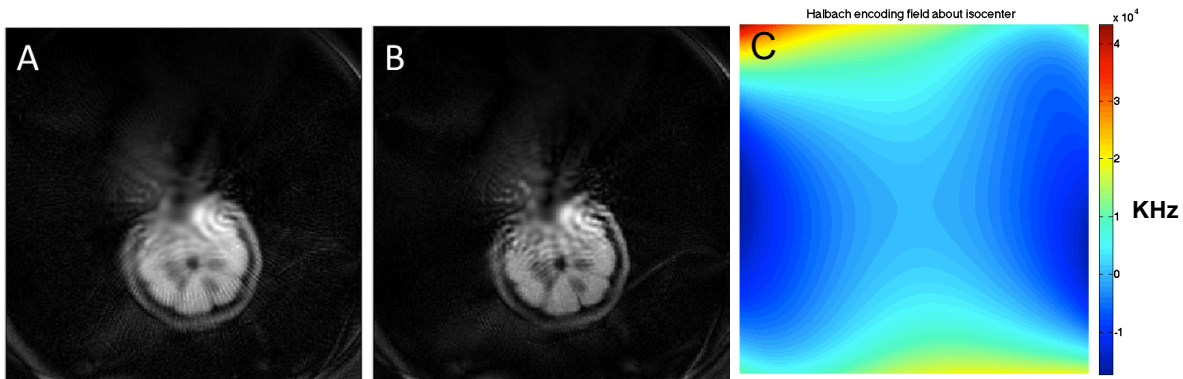


Figure 37: Spin echo image of a 1 cm thick slice of lemon. FOV = 16cm, BW = 40KHz, NA = 1, 128-echo train, readout pts = 256, TE/TR = 8/4500ms. (A) 91 magnet rotations spaced 2° apart, (B) 181 magnet rotations spaced 1° apart, and (C) matching slice of the Halbach nonlinear encoding field. Acquisition time for 181 projections was 93 minutes, which can be reduced to 15 min. with simultaneous parallel reception.

Halbach array LFI: field mapping towards 3D imaging

Having achieved proof-of-concept of 2D imaging with the Halbach scanner, there is a clear path to acquire 3D images.:

1. Map the Halbach field over a 3D spherical imaging volume, superseding our existing 2D field map.
2. Reconstruct 2D phantom objects positioned in planes offset from the magnet isocenter.
3. Build a TRASE RF transmit coil in order to apply a linearly-varying transmit field during spin excitation, performing phase encoding along the slice direction.

Toward goal 1, we have designed and fabricated an array of field probes [21] oriented along “lines of longitude” on a spherical surface of radius 8 cm Figure 38. Previously we rotated the Halbach magnet around a 1D linear array of probes in order to create the 2D field maps used for reconstructing the images in Figure 36 and Figure 37 above. By contrast, the new 2D field probe array is rotated while the Halbach magnet remains stationary, acquiring frequencies across the entire surface of a sphere (Figure 39). The frequency data are then fit to spherical harmonic basis functions that in turn are used to calculate field maps in any desired slice within the sphere.

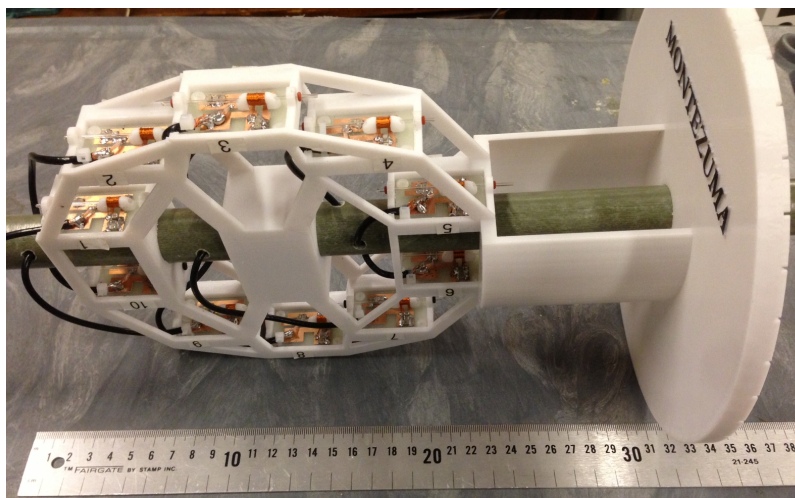


Figure 38: New 2D field probe rotates in increments of 15 degrees on a fiberglass rod that is coaxial and centered relative to the Halbach magnet rungs.

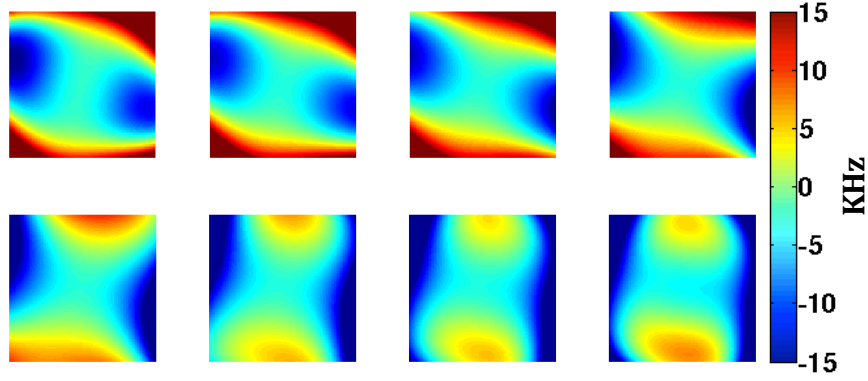


Figure 39: At each rotation angle of the field probe in Figure 38, NMR data is acquired along a “line of longitude” residing on the spherical ROI. Spherical harmonics up to 5th order are fit to the acquired NMR frequency data. Field maps are then calculated on any desired grid of points within the mapped region. Transverse slices at offsets of -4cm to +3cm from isocenter are shown.

Halbach array LFI: spatial encoding in 3D:

Two dimensional Halbach imaging was successfully implemented and is in press in *Magnetic Resonance in Medicine* [attached as Appendix 9]. Moving forward, our goal to implement spatial encoding along the remaining third dimension: the axis of the Halbach cylinder. The Halbach’s “built-in” rotating encoding field achieves high in-plane resolution transverse to the axis, but provides minimal spatial encoding along the axis of rotation. Our goal is to use a specially-designed RF transmit coil with linear B_1 phase variation to encode slices along the third “missing” dimension. The name for this spatial encoding technique is Transmit Array Spatial Encoding, or TRASE [22].

TRASE performs spatial encoding in a manner entirely analogous to conventional phase encoding. Before each acquired echo in a spin echo train, a progressively stronger linear phase modulation is applied to the spins. The difference is that instead using a linearly-varying magnetic field, TRASE uses the linearly-varying phase of an RF field.

For B_0 oriented along the z -axis, the spatial variation of a TRASE coil B_1^+ field can be described as

$$\bar{B}_1 \cong \bar{y}\cos(gx) \pm \bar{x}\sin(gx),$$

where the phasor describing the time-harmonic variation of the RF field has been ignored for clarity. The factor g describes the strength of the phase gradient along the x -direction. By Euler’s theorem, this expression is equivalent to $\exp(\pm jgx)$, which describes a linear phase slope along x . The coil should be designed so that this phase varies by 90-deg across the field of view.

During spin excitation and refocusing pulses, the phase of the transmit B_1^+ field is applied to the spins along the encoding direction. If the direction of the phase slope is switched between subsequent refocusing pulses in a spin echo train (for instance using a 180-deg phase shifter circuit), then each acquired echo corresponds to a different point in k -space for the slice dimension. Using an appropriate echo train, k -space can be traversed for the desired slice thickness and field-of-view (FOV). Separation of the data into slices is then achieved via Fourier transformation along the echo train. As in conventional MRI spatial encoding, the strength of the phase slope determines Δk and thus the FOV, while the number of acquired readouts/ k -space points sets the slice thickness (resolution).

We have made significant progress toward building a TRASE coil array for the Halbach scanner, but we expect it will take several more months before we finish building the coil and use it for spatial encoding. The principal reason for the delay has been the difficulty of achieving linear B_1 phase variation over the target 16 cm-diameter volume-of-interest (VOI). Because the TRASE coils reside on 18 cm and 20 cm cylinders that are only slightly larger than the VOI, it is difficult to eliminate undesired (concomitant) B_1 vector components everywhere within the VOI. Previous realizations of TRASE coils [22], [23] minimized concomitant fields by placing coil windings further away from the VOI. For instance, the Helmholtz-pair/double-Maxwell-pair shown in Figure 40 used coil windings on a 28 cm×28 cm×42 cm rectangular former to image a volume with a 16.7 cm diameter.

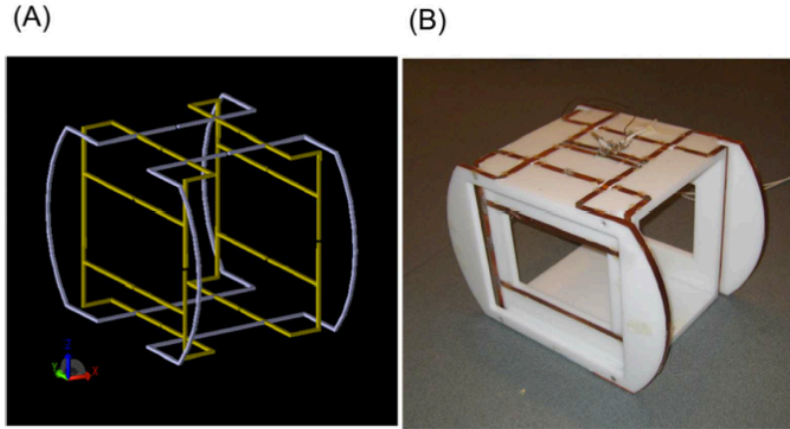


Figure 40: Prototype TRASE coil used in [23] to perform spatial encoding along one dimension. The coil consists of a double Maxwell pair (yellow) and curved Helmholtz coil (blue) that are driven 90 deg out of phase. Unfortunately, this boxy coil geometry is not well-suited to the cylindrical Halbach magnet system. Image reprinted from [23].

The tentative design for the Halbach TRASE array is shown in Figure 41. This array contains a reverse Maxwell pair to provide the $\bar{x}\sin(gx) B_1$ component (Figure 41a). The $B_1 \bar{y}\cos(gx)$ component is created by an “Orthogonal Double Solenoid” (ODS) coil (Figure 41b)

[24]. The Maxwell coil will be wound on an 18 cm diameter cylinder, which will be nested inside the 20 cm diameter ODS coil. Along the x-axis, the design shows the desired field orientation and phase slope (Figure 42). However, as visible in Figure 41, substantial cross-term components exist for off-axis positions, causing variation in the phase slope and effective slice thickness. Presently the coil is being redesigned in an effort to reduce the concomitant fields. Techniques such as the target field method [25] will be explored as methods for generating winding patterns on the cylinder surface that minimize the unwanted field components.

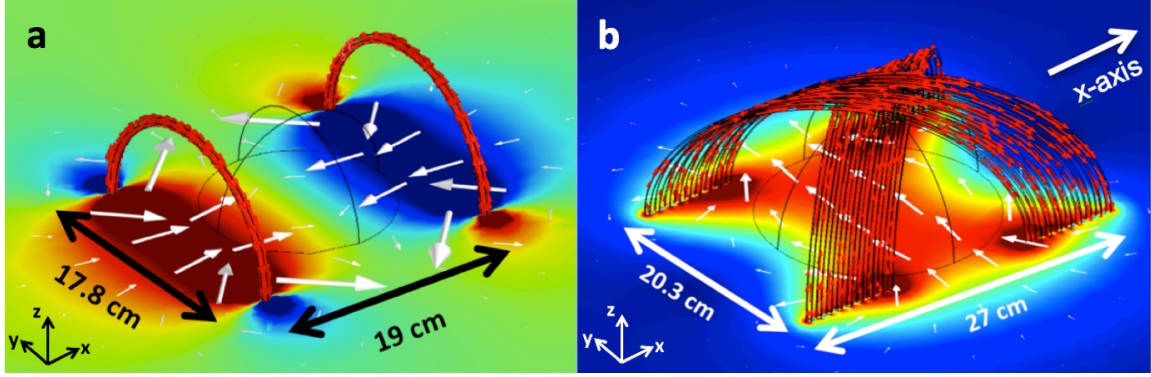


Figure 41: B_1^+ vector plots (white) and current paths (red) of the preliminary design for crossed solenoid (left) and Maxwell pair designs for the y and x oriented fields, respectively. The B_0 background field is oriented along z and the axis of the Halbach cylinder is along x. Simulations are performed using a Biot-Savart magnetostatic calculation to approximate the 3.3 MHz RF field distribution. The plots show significant concomitant fields within the 16 cm-diameter spherical volume-of-interest. These field variations translate into variability in the slice thickness at different in-plane voxels. Refinements to the coils designs should mitigate the undesired off-axis concomitant fields.

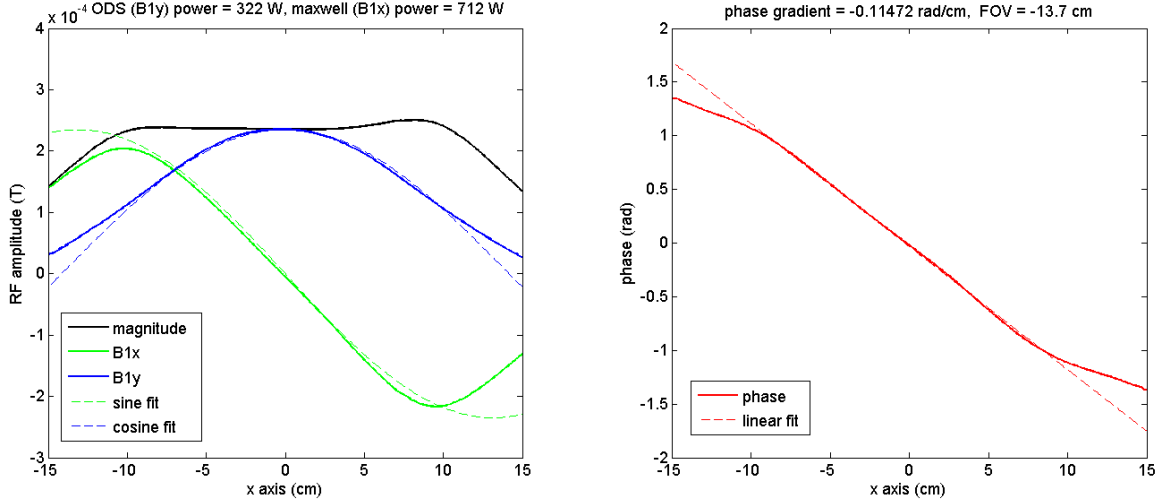


Figure 42: Magnitude plots (left) along the Halbach axis for the Maxwell pair (B_{1x}) and the crossed solenoids (B_{1y}) provide good approximations for the desired sine and cosine field variation. The linear phase required for Fourier encoding is shown at right. Unfortunately, in this preliminary design, the linear phase slope varies by as much as a factor of two at points away from the Halbach axis, causing variation in the encoded slice thickness and making direct Fourier reconstruction intractable.

Alternatively, if concomitant fields can not be mitigated with a practical, realizable coil design, then the plan is to implement the existing TRASE coil design along with full 3D image reconstruction that explicitly accounts for variation in the slice thickness as a function of in-plane position. In this approach, care will be taken to avoid aliasing between slices due to under-encoding in regions where the B_1 phase slope is weakest. One disadvantage of this approach is that it uses a time-consuming iterative solver for all three reconstruction dimensions, whereas TRASE data acquired using a suitably linear phase gradient can be reconstructed by simple Fourier transformation.

TRASE coil implementation will occur during Q1–Q2 Y4. We are confident that the coils can be redesigned, built, and tested on the scanner during the first half of 2014. Once TRASE is functioning, the Halbach system will stand as the world’s first truly portable, lightweight MRI brain scanner.

RF power amplifier:

In Q4Y3, we acquired a state-of-the-art 2 kW Tomco RF power amplifier with more than twice the available power of any other amplifier in the lab. This will permit shorter excitation and refocusing pulses in the Halbach imaging sequence, broadening the bandwidth of the pulses. To excite the full imaging volume, the RF pulse must cover the full range of frequencies in the sample (~ 30 -50 KHz). The Halbach magnet has a permanent quadrupolar inhomogeneity/encoding field

that can not be switched off during excitation. Because of this, it is critical that the RF system deliver power across the entire spin bandwidth to obtain signal from every voxel in the sample. The new 2 kW amplifier will be instrumental in achieving this goal.

Halbach array LFI: future work

Once 3D spatial encoding is demonstrated on the Halbach proof-of-concept prototype, we summarize here the steps needed extend the technique to human brain imaging, beyond the scope of the presently funded work. The roadmap for developing such a scanner is as follows:

1. Design and build a modestly larger Halbach array to accommodate the human head.
 - a. Include subject support structure to accommodate and support the subject's shoulders while still permitting free rotation of the Halbach magnet assembly.
 - b. Explore the use of trapezoidal rungs to permit the use of more magnetic material, maintaining or even increasing the B0 field strength as compared with the first prototype (78 mT).
 - i. Optional: Interleaving Halbach rungs of NdFeB with SmCo would allow temperature stabilization of the magnetic field, at some detriment to the field strength and signal-to-noise ratio as described in [26].
2. Map the field of the new Halbach magnet in the brain region-of-interest using a field probe assembly.
3. Build a set of transmit and receive coils at the frequency of the human Halbach magnet prototype.
4. Procure a multi-channel RF receiver to allow true parallel imaging in order to limit the acquisition time.

TASK 1C: Demonstration of head imaging

Brain MRI in the electromagnet LFI at 6.5 mT

Single channel Transmit/receive helmet coil at 276 kHz

Over the last quarter, a single channel head coil (Figure 43) was built in order to perform head MRI in healthy volunteers at 276 kHz. The coil features high sensitivity over the entire volume of interest thanks to a close-fit winding. The coil was designed to provide very homogeneous magnetic field profiles as all our imaging sequences rely on steady-state techniques [11], extremely sensitive to flip angle homogeneity. The coil was wound with a 45° oblique angle around a fiberglass head cast so that magnetic field B_1 stays orthogonal to the main magnetic field B_0 , preventing coupling issues.

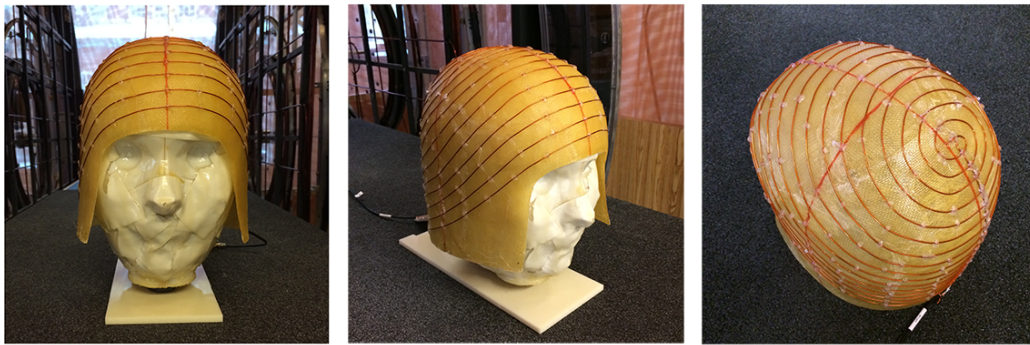


Figure 43: Front, side and rear view of the single channel head coil placed on a head-shaped phantom. 19 AWG insulated copper wire was wound in spiral around a fiberglass head cast.

By design, the very homogeneous B_1 field makes this specific coil suitable for both transmit and receive operations. The ability to use the single channel spiral coil with SSFP techniques (i.e. potential artifacts resulting from flip angle inhomogeneity) was first tested in a 15 cm diameter plastic bottle filled with water (Figure 44). The sequence was combined with undersampling strategies as described in previous reports. The images show high signal to ratios (SNR) and very good signal homogeneity over the entire volume without any of the typical b-SSFP related artifacts [11].

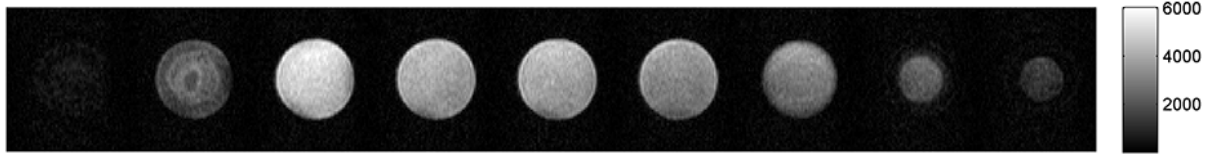


Figure 44: 3D images acquired in a plastic bottle filled with water. The imaging parameters were as follows: TE/TR=20/33 ms, Matrix=64×65×9, voxel size =3×3×10mm³, $\alpha = 90^\circ$. undersampling rate = 52%, number of averages (NA) = 50. Max SNR = 44. Total acquisition time was 8.5 min. All images acquired at 6.5 mT.

The imaging sequence was then optimized with a head-shaped phantom. The image shown in Figure 45 shows 3D coronal slices in the head-shaped phantom seen in Figure 43.

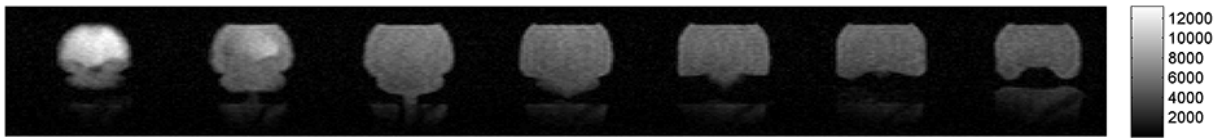


Figure 45: 3D images acquired in the head-shaped phantom (Figure 1), 7 central slices are shown. The imaging parameters were as follow: TE/TR=20/33 ms, Matrix=64×65×9, voxel size =3×3×10mm³, $\alpha = 90^\circ$. Number of averages (NA) = 100, undersampling rate = 52%. Max SNR = 56. Total acquisition time was 17 min. All images acquired at 6.5 mT.

Non-magnetic subject table for human imaging in the electromagnet LFI

A non-magnetic subject table was built out of Baltic birch plywood and aluminum strut (Figure 46). Every conducting loop in the table near the receiver coil was eliminated to prevent electronic noise to be picked up by our NMR detection coil.

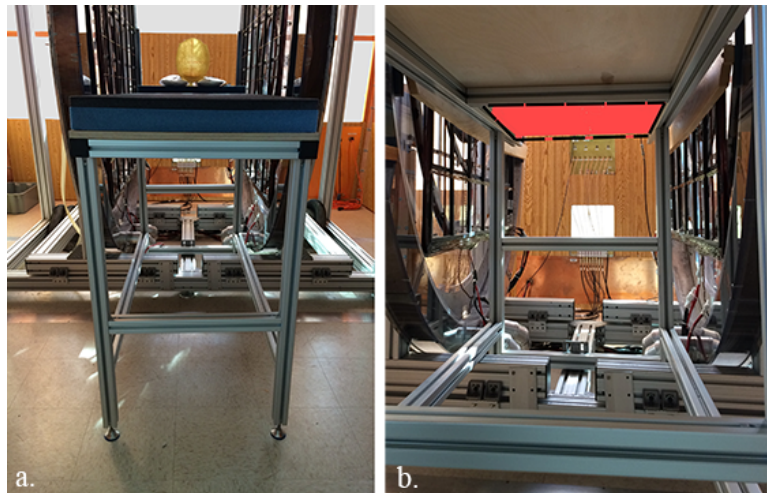


Figure 46: Images of **a.** subject table built for *in vivo* human head imaging in the electromagnet LFI (the head coil is placed on the table top), and **b.** Detail of the aluminum strut from below the table. Conductive loops were removed in the vicinity of the detection coil (highlighted in red).

Head imaging in healthy normal subject at 6.5 mT

Head images were acquired in a healthy volunteer in axial, sagittal and coronal orientations using b-SSFP combined with undersampling. Flip angle was set to 70° to maximize SNR *in vivo*, undersampling rate was set to 50%. Images in the coronal orientation are shown in Figure 47.

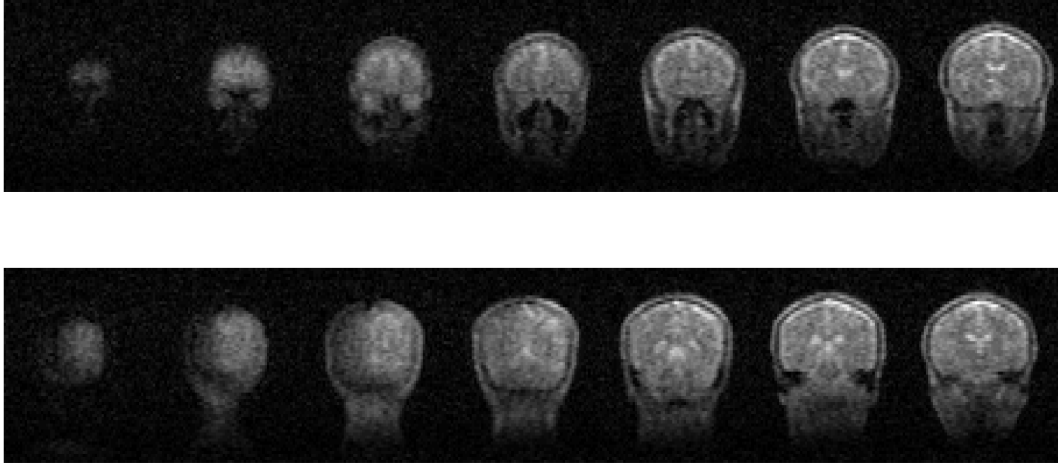


Figure 47: 3D images acquired in a healthy volunteer. The imaging parameters were as follow: TE/TR=20/33 ms, Matrix=64×65×15, voxel size=3×3×10mm³, $\alpha = 70^\circ$, undersampling rate = 50%, number of averages (NA) = 110. Max SNR = 30. Total acquisition time was 29 min. Images acquired at 6.5 mT.

Data in all three orientations were zero-filled so that the resulting interpolated matrices were 128×128×15. Filtering was applied to all interpolated datasets using anisotropic diffusion filtering [27]. Anisotropic diffusion filtering is a powerful denoising filter that iteratively convolves images of interest with Gaussian filters of different sizes. The anisotropic diffusion filtering algorithm detects regions of high signal intensity (grey level) gradients after each iteration, and adapts the size of the Gaussian filter locally, thus preserving edges and high spatial frequencies and preventing image blurring. The processed interpolated matrices are shown in Figure 48.

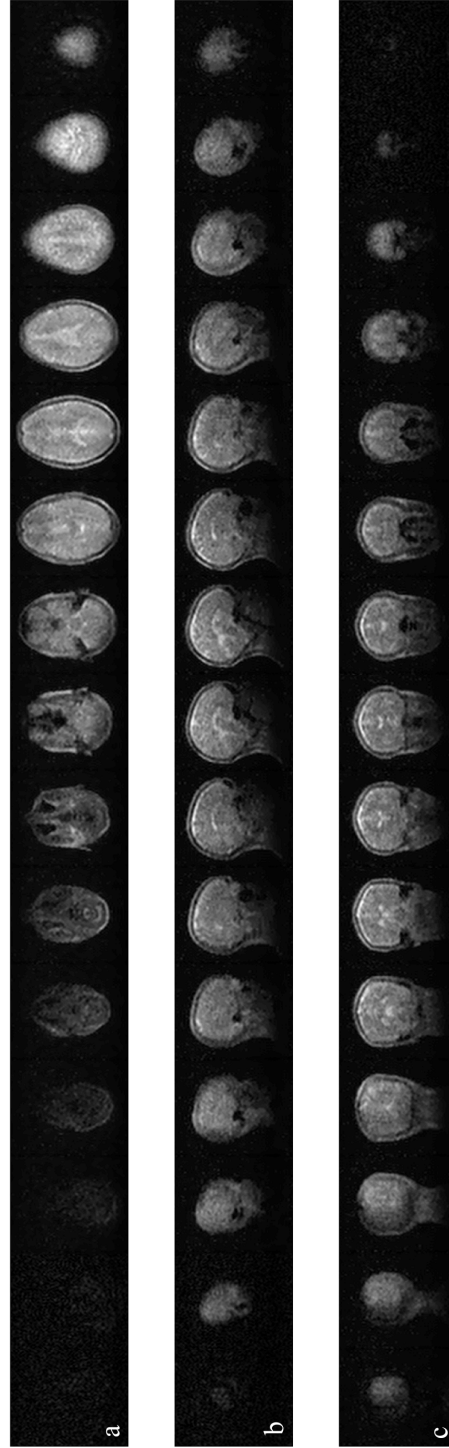
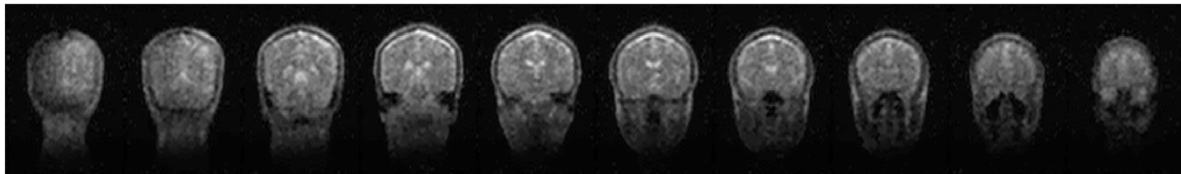


Figure 48: 3D head images acquired in a healthy volunteer at 6.5 mT, **a.** axial, **b.** sagittal, and **c.** coronal orientations after interpolation and anisotropic diffusion filtering. The imaging parameters were as follow: TE/TR=20/33 ms, Matrix=64×65×15, voxel size =3×3×10mm³, $\alpha = 70^\circ$, undersampling rate = 50%, number of averages (NA) = 110. Max SNR after interpolation and filtering = 96. Total acquisition time was 29 min.

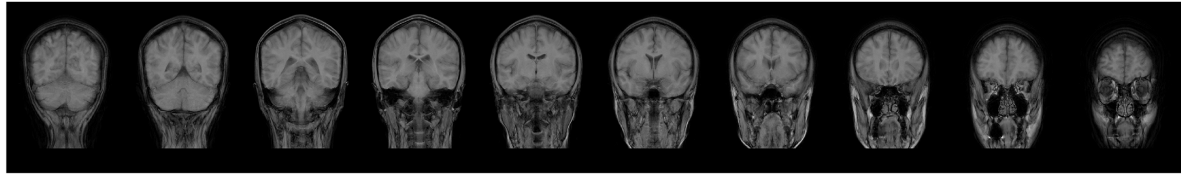
Comparison of 6.5 mT to 1.5 T

The images acquired at 6.5 mT were compared to images of the same subject acquired at 230 times higher magnetic field, (1.5 T) in Figure 49. The images acquired at low field show many of the anatomic features that are seen at higher magnetic field, such as CSF around the brain hemispheres and in the ventricular system, grey and white matter, the cerebellum, the eyes, sinuses and ear ducts. The contrast obtained using b-SSFP at low magnetic field, which relies on the ratio T_2/T_1 of the imaged species, is closer to T_2 -weighted contrast, as suggested by the axial high magnetic field MR image presented in Figure 49 (lower row). In the latter case cerebrospinal fluid is bright and grey matter is darker than white matter.

a. Coronal

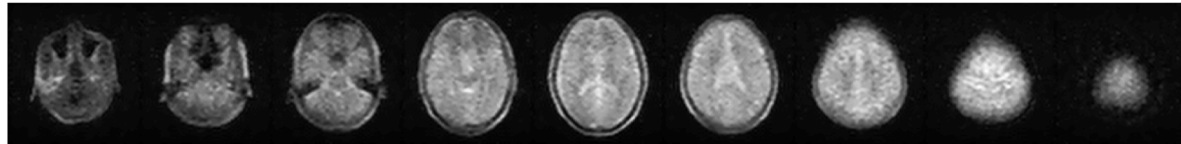


0.0065 T

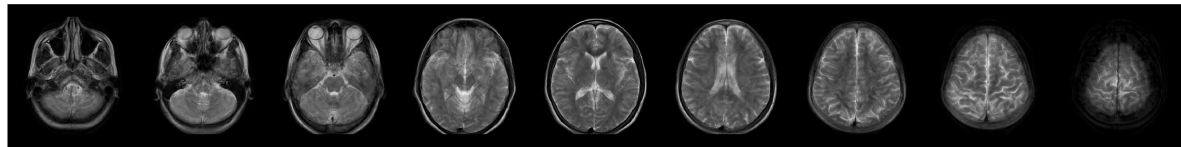


1.5 T - T_1 weighted

b. Axial



0.0065 T



1.5 T - T_2 weighted

Figure 49: Comparison of the head images acquired at 6.5 mT with images of the same subject acquired at 1.5 T in a. coronal and b. axial orientation. Ten and nine center-most slices are shown, in each orientation, respectively.

Another benefit of low magnetic field imaging is that magnetic susceptibility differences are much smaller, preventing phase aberrations that will result in signal losses or image distortions at

air-tissue interfaces, or due to the presence of metal, such as in the case of dental work, as shown in Figure 50.

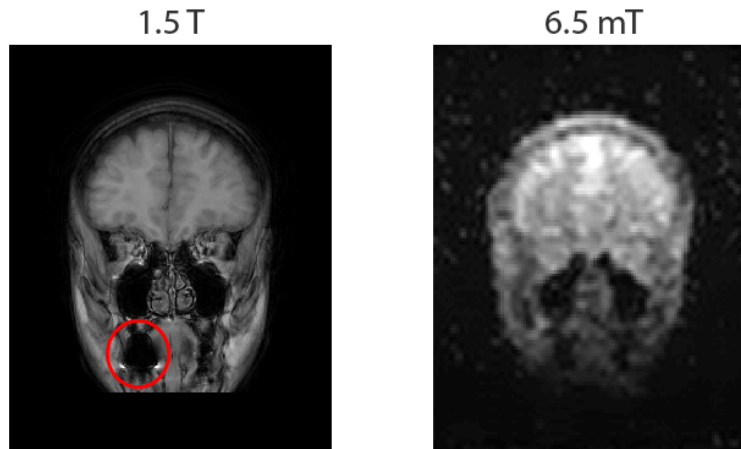


Figure 50: At 1.5 T the presence of metal dental work in this subject results in signal losses in the mouth of the subject (inside the red circle) due to magnetic susceptibility artifact. Despite low SNR in this particular area due to coil coverage, no susceptibility artifact is seen at 6.5 mT.

In summary, images of a human head were acquired *in vivo* in a human head in less than 30 minutes with a single channel coil with $3 \times 3 \times 10 \text{ mm}^3$ voxel size. The improvements required to decrease the acquisition time while increasing the spatial resolution are well known. To date, the major restrictions on our current setup are noise filtering on the gradient line and gradient strength provided by the LFI scanner, with a maximum of $1 \text{ mT} \cdot \text{m}^{-1}$, slewing at a maximum of $0.75 \text{ mT} \cdot \text{ms}^{-1}$. With proper noise filtering and twice the gradient strength, the images shown here could be easily acquired in less than a minute. Combined with multi-channel detection strategies, the current images could be acquired within far shorter acquisition times.

OMRI Injury Imaging

TASK 2A: OMRI Hardware Development

The optimization of hardware and pulse sequences required for Overhauser Magnetic Resonance Imaging (OMRI) is of key importance to Specific Aim 2. We describe below a new acquisition strategy aimed at improving the sensitivity of OMRI to free radicals *in vivo*. We also report in this section the realization of SENSE-based parallel imaging acceleration in combination with Overhauser-enhanced free radical fast imaging in the electromagnet LFI.

Improving radical detection sensitivity through pulse sequence design

A key challenge in implementing OMRI for TBI will be detecting the small concentrations of radical present *in vivo*. We have previously shown (see Y2 Annual Report) that 10 μM nitroxide radical in water and 50 μM nitroxide radical in water can be detected with Overhauser spectroscopy (Figure 51) and OMRI (Figure 52), respectively. The concentration of free radical at the location of injury remains *unknown*, but estimates range from 50 nM to 50 μM [28]-[35]. Additionally, detecting free radicals *in vivo* will be more difficult than in phantoms due to extra relaxation pathways reducing the efficiency of DNP. Therefore we would like to try and improve our detection efficiency even further.

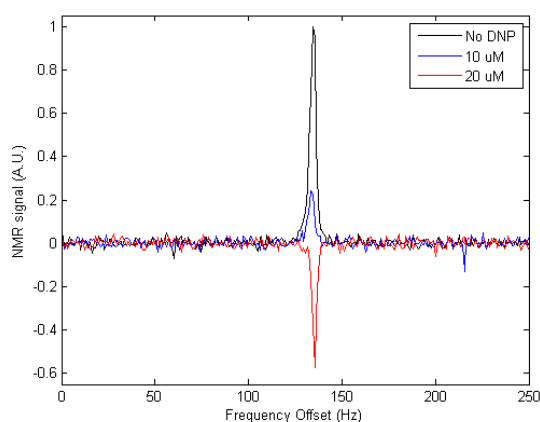


Figure 51: Measurement of the sensitivity threshold to small concentrations of nitroxide radical via Overhauser enhanced NMR spectroscopy. These spectra were acquired in the electromagnet LFI at 6.5 mT (276 kHz). The ESR frequency was 140 MHz.

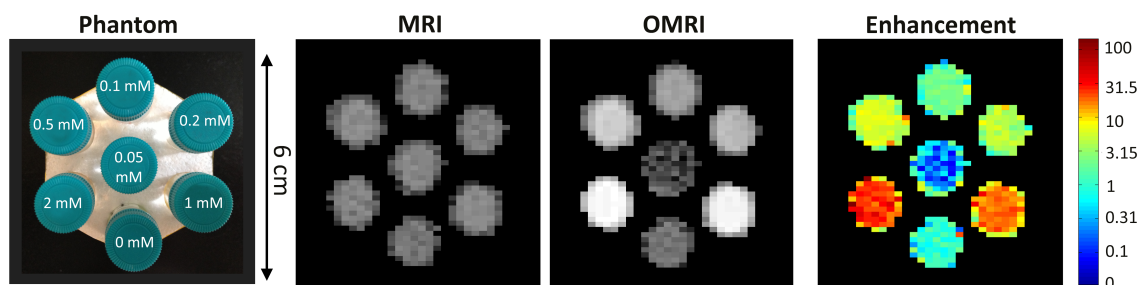


Figure 52: Photograph of phantom used to demonstrate the sensitivity of OMRI to nitroxide radical concentration. All seven vials have very similar image magnitudes in the conventional **MRI** image. The **OMRI** scan demonstrates marked image-based free radical sensitivity. The signal magnitude from the control vial remains unchanged in OMRI scan. **OMRI enhancement** image is computed from the ratio of OMRI to MRI magnitude. MRI and OMRI were both obtained at 6.5 mT. The NMR frequency is 276 kHz and the ESR frequency is 140 MHz.

There are a limited number of steps one can take to try and improve the detection sensitivity of the Overhauser effect to free radicals. One possible route would be to use three transmit coils tuned to each of the three EPR resonances of the nitroxide radical. This would result in a dramatic increase in SAR, but could in principle result in a threefold increase in detection sensitivity. Hardware limitations prevent us from testing this technique as our spectrometer has a single high frequency transmit channel. Another route is to take advantage of the fact that we can turn the DNP enhancement on and off with RF, unlike relaxation contrast agents. This means we can modulate the signal amplitude at a known frequency in regions where free radicals are present. We are inspired by the BOLD fMRI experiment [36] where changes in the oxygenation of the blood result in a small (1-5%) change from a known stimulus and are measured by analyzing the signal amplitude versus time. Fitting a known modulation function to the noisy data may be more sensitive to small amplitude changes than signal averaging alone.

To test the feasibility of this technique, simulations were performed of small amplitude changes that are corrupted with noise (**Figure 53**, black line with open circles). The added noise amplitude was two times larger than the change in signal amplitude (equivalent to an SNR of $\frac{1}{2}$) and 1% linear drift was added to emulate a small temperature change (the temperature can be monitored in a real experiment and added into the modulation function used to fit the data). In the simulation two data points are acquired without application of DNP (i.e., zero amplitude change), followed by two data points acquired with DNP (decrease in signal of 0.3), and the sequence is repeated 15 times. Random noise with peak to peak amplitude of 0.6 was added to all data points. Looking at the noisy data alone, it is unclear if there is any signal change with DNP. However, fitting the data to the known modulation function gives a signal change of 0.31 ± 0.04 which is in excellent agreement with actual signal change in the simulation. Moreover, the error in the fit is very small so there is little doubt that a signal change with DNP exist, meaning free radicals are present (in the simulation).

A benefit of interleaving the reference and DNP images in this way as opposed to normal signal averaging is to lower the time averaged SAR. That is, by alternating between reference and DNP images, the time averaged SAR can be reduced by a factor of two without increasing the total experiment time. As SAR is a concern for *in vivo* applications due to the high power of ESR irradiation needed for DNP, interleaving the reference and DNP images could prove very beneficial to mitigate heating effects.

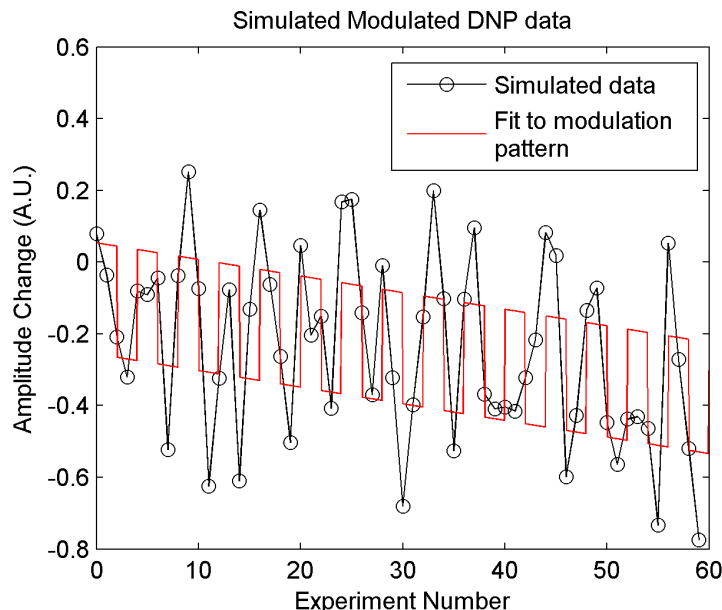


Figure 53: Simulation of interleaved reference and DNP signals. Two experiments are simulated with no DNP followed by two experiments with DNP (open circles, black line is to guide the eye). The added noise is two times larger than the simulated signal change of 0.3, yet the fit to the noisy data unambiguously determines a signal change with DNP (0.31 ± 0.04).

Parallel imaging and SENSE with OMRI

In Y3, we made significant progress incorporating DNP into parallel imaging. This is an important step because for larger samples, and particularly human subjects, parallel imaging is the standard technique for accelerated MRI. The addition of DNP into our parallel imaging setup required the construction of both a 140 MHz coil for saturation of the electron spin resonance and a larger 276 kHz coil for NMR transmit. The larger NMR transmit coil was required as both the 8 coil receive array and the 140 MHz coil must fit inside the NMR transmit coil (Figure 54). Large, high frequency coils can be particularly challenging to build due to increased radiation losses [37]. This problem is compounded by the need for high power continuous wave irradiation for DNP; requirement commercial high field coils do not meet. As an initial step towards human head size coils, we constructed a 14 cm outer diameter saddle coil that fits inside our current 8-channel array. This coil has proven handle high power CW irradiation for extended periods of time.

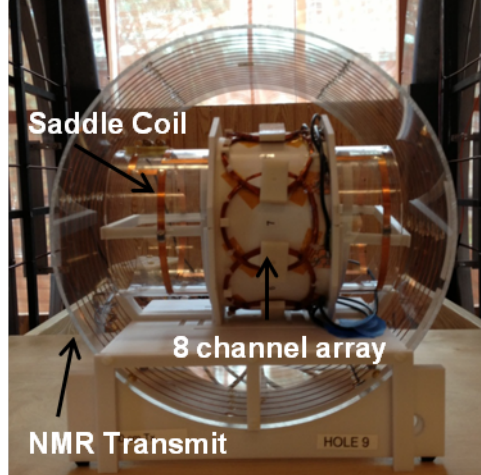


Figure 54: Photograph of the multi-channel OMRI system. The 8 channel receive parallel array was described in previous reports. The NMR Tx coil is a 30 cm diameter solenoid, and the ESR Tx coil is a 14 cm diameter saddle coil. The NMR frequency is 276 kHz and the ESR frequency is 140 MHz.

As discussed previously, SENSitivity Encoding (SENSE) at low magnetic field (and low frequency) is an unusual regime because the coil sensitivity is expected to be a constant, in contrast to at high magnetic fields where the coil sensitivity must be recalibrated for each sample. However, for this to be successful, it is crucial that the alignment of the parallel array with respect to both the sample and the EPR coil be repeatable. Misalignments can result in large artifacts as shown in Figure 55.

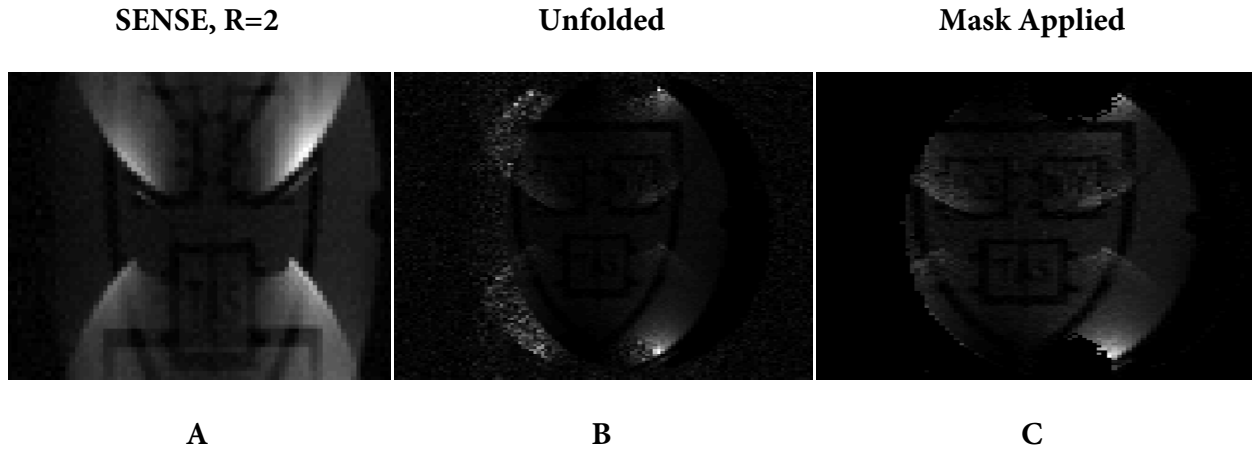


Figure 55: Example of misalignment between coil sensitivity map and sample. **A** is a typical aliased image resulting from SENSE imaging with a reduction factor $R=2$. **B** is the unfolded/unaliased image. The image of the phantom displaying the Harvard shield and logo has been coherently reconstructed. However, due to a small deviation in the placement of the sensitivity map and the sample, a crescent shaped wedge on the left side of the image has been mapped to the noise while a crescent wedge on the right has been reconstructed as containing no signal. The final image in **C** was obtained by applying a mask obtained from the sensitivity map image.

In order to avoid these complications, an assembly for positioning the coils and phantoms was designed and 3D printed. This new assembly (shown in Figure 56) enables repeatable positioning within the transmit array (Figure 56-1) of the parallel array coil receive coil (Figure 56-2), EPR saddle coil (Figure 56-3) and phantom (Figure 56-4), with respect to each other. This assembly consists of four parts:

- a) A table to center the receive array inside the transmit coil.
- b) Two half rings that mount to the saddle coil to keep it concentric to the receive array and support and center the saddle coil inside the NMR transmit coil.
- c) A belt with knobs fastened to the saddle coil (not visible) to prevent the coil from rotating and maintain a repeatable orientation.
- d) Plugs for centering the phantom inside the parallel array. The arms register to the edges of the saddle coil.

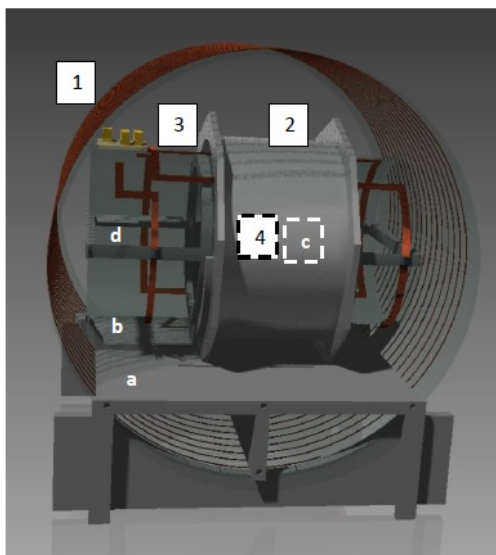


Figure 56: Schematic of the imaging assembly for Overhauser-enhanced parallel imaging

Using the new kinematic mounting assembly we have achieved the first accelerated SENSE reconstruction images at low magnetic field with DNP (Figure 57b). Further, this reconstruction was performed using a coil sensitivity map acquired on a homogeneous sample. This is an encouraging first result as this is not possible at high magnetic field. However, while the SENSE reconstruction is of sufficient quality to see the object, there are still artifacts from unaliasing the undersampled image. We believe this artifact is caused in part by the very large SNR at the edge of the sample from DNP.

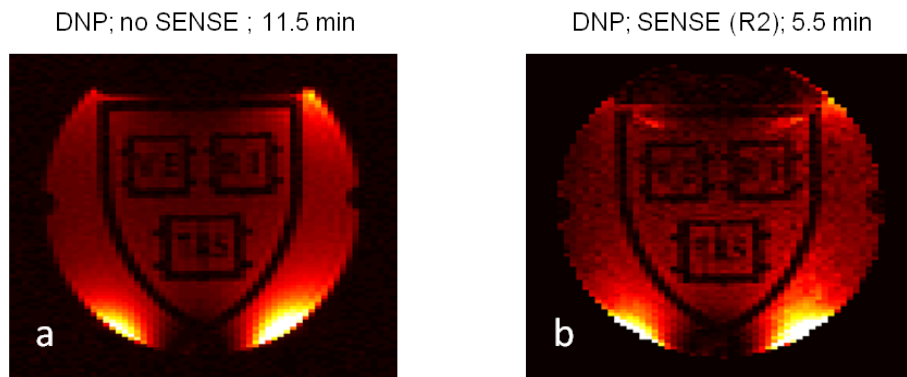


Figure 57: a) Parallel image with DNP and no acceleration. b) Parallel image with $R = 2$ SENSE reconstruction with DNP.

We are encouraged by these early DNP results with parallel imaging and that we were able to obtain a quality SENSE reconstruction using a sensitivity map acquired on a different sample. We are currently working on improving the SENSE reconstruction method to remove the artifact observed in Figure 57b. We are also exploring incoherent random undersampling strategies that we have used in the past [38]. We plan to compare the two approaches to determine which technique provides reliable image reconstruction in the shortest amount of time.

TASK 2C: *Ex vivo* radical detection

Free Radical Detection in Rodent Blood

Our previous work on the detection of free radicals has focused on decreasing the image acquisition time [38] and improving the detection limit for low concentrations of free radicals (see Y2 Annual Report). Our efforts on these two areas has focused on unique acquisition strategies and improved hardware. During this development stage we have used simple phantoms of dissolved free radicals in solution. In Year 3 we began experiments aimed towards *in vivo* applications with Dr. Peter Caravan's group at the MGH/A.A. Martinos Center for Biomedical Imaging. Dr. Caravan is an expert in targeted molecular imaging and his group has labeled the protein albumin with the TEMPO free radical. Not only will these experiments provide a more realistic measure the DNP enhancements we can expect *in vivo*, but nitroxide labeled albumin may prove to be a new class of valuable, redox sensitive imaging contrast agent.

Animal experiments were performed under an existing protocol from the Caravan group. The labeled albumin was injected into the bloodstream of an anesthetized rat, and blood draws were done at 2, 5, 15, 30, 60, and 90 minutes to estimate the lifetime and visibility of TEMPO in the blood. Overhauser-enhanced spectroscopy measurements were made shortly after each blood

draw, with the drawn blood stored on ice prior to measurement. Figure 58 shows the decay of the DNP enhancement factor with time. An exponential fit of the data gives a lifetime for the free radical in the blood of ~ 16.5 minutes. However, even at 30 minutes, there is still an easily measureable DNP signal.

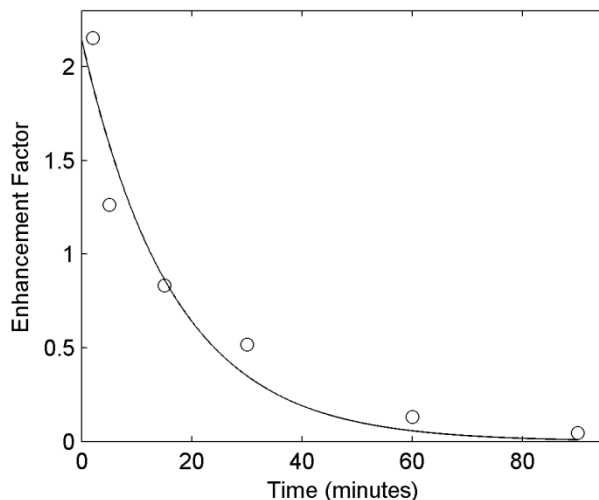


Figure 58: The decay of the DNP signal from the TEMPO radical attached to the protein albumin. The solid line is an exponential fit to the data giving a lifetime of 16.5 minutes.

The enhancement factors shown in Figure 58 are relatively small; however, a small concentration of labeled albumin was used in this experiment due to a limited amount of material. The concentration of free radical can be increased by a factor of ten, which would result in five to ten times larger DNP enhancements. The data in Figure 58 suggests that a fivefold increase in the DNP enhancement would push the visibility of free radical in the blood to approximately one hour. In Q4, we expect to increase the yield and efficiency of attaching TEMPO to albumin, and thus achieve much larger enhancements and visibility time than shown in Figure 58.

Exogenous free radicals as probe of BBB and redox status in rats

Our previous OMRI experiments focused on pushing the limits of speed, resolution, and sensitivity to free radicals beyond what has previously been obtained. These experiments have been successful in achieving the fastest and highest quality OMRI to date [38]. While our OMRI strategy shows great promise, it is crucial that we test and verify the safety of OMRI experiments. Small animal imaging is the next logical step in the development of OMRI for diagnostic use.

We have been collaborating with Dr. Cenk Ayata and Dr. Fannie Herisson in the departments of Neurology and Neuroscience at Massachusetts General Hospital. Dr. Ayata is stroke neurologist and neuroscientist with an interest in the use of OMRI in conjunction with injected nitroxide radicals as a new tool to probe hyperacute disruption of the blood-brain barrier (BBB). Dr. Ayata

provided several rats to our group for a pilot study on the feasibility of using OMRI to detect radicals inside the brain. Dr. Ayata's laboratory induced a reversible occlusion of the middle cerebral artery (fMCAO) in these rats as described below.

Ischemia reperfusion model in rodents

In the transient occlusion rodent models, a nylon filament is used to occlude the middle cerebral artery (MCA), one of the intracranial branches of the internal carotid artery. Rats are operated under anesthesia and temperature control system with a heating pad. After cervicotomy and dissection of the carotid bifurcation, the pterygopalatine artery, which is the only cervical branch of the internal carotid artery, is ligated. A nylon monofilament will be then inserted into the internal carotid artery from the external carotid artery and pushed in the circulation to the MCA in the brain. The right positioning and the effectiveness of the filament occlusion is continuously monitored by transcranial Doppler. After 30 to 60 minutes of filament occlusion, the reperfusion is allowed by removing the filament.

Pilot study in rat

In our initial experiment, a rat was subject to a 75 minute ischemia and 60 minute reperfusion according to the animal protocol in Dr. Ayata's lab. A solution of 300 mM TEMPOL per gram of body weight was prepared, and 3.6 μ L injected. The animal was sacrificed immediately afterwards. The rat was then quickly brought to our laboratory and loaded into a coil specifically designed for these experiments shown in Figure 59. Approximately 20 minutes after the animal was sacrificed, we began an OMRI experiment using our new b-SSFP OMRI sequence previously described. The total imaging time was 3 minutes.



Figure 59: Rat loaded into a coil designed for OMRI brain imaging. A solenoid coil is used for MRI transmit and receive while a single turn surface coil sits just above the head for EPR transmit.

OMRI easily reveals the presence of free radical inside the rat brain as shown in Figure 60. This is an encouraging result as regions where nitroxide radicals are present were much more intense and easily distinguishable from non-affected tissue. This suggests that the nitroxide radical can provide excellent contrast inside the brain. Additionally, the high intensity of affected regions implies a smaller dose of radical and/or lower applied EPR power can be used and still provide contrast. As this was our first attempt at imaging a rat brain, no undersampling was implemented in this experiment. Previous experiments showed successful reconstruction with 50 – 70 percent undersampling rates. Assuming these can be applied to the rat brain, the acquisition time could be reduced to as little as 1 minute.

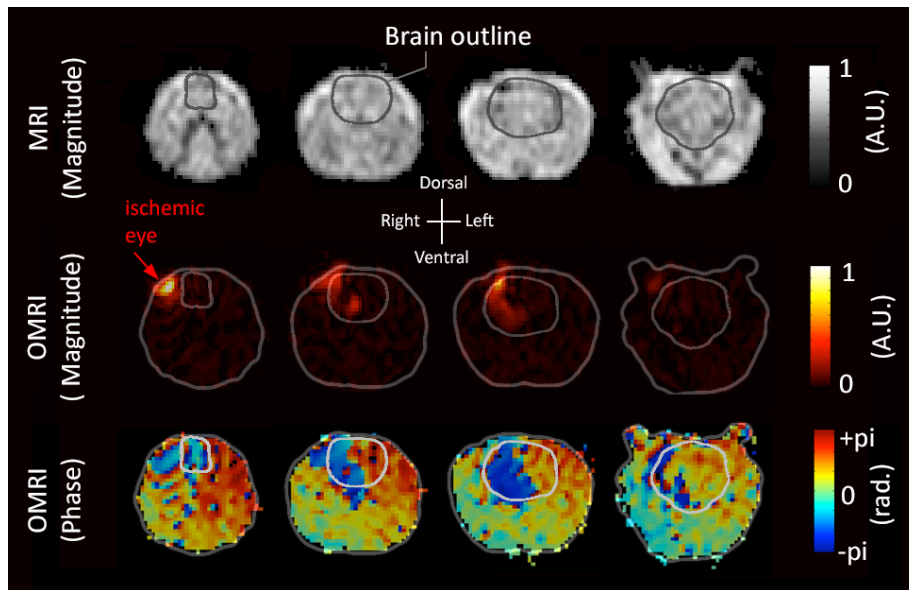


Figure 60: *Top row*: Reference image of the rat brain acquired after the OMRI image below. Acquisition time of the reference image was 23 minutes. *Middle row*: OMRI image acquired ~ 20 minutes after death. Regions where the nitroxide radical is present have much larger signal amplitude and are easily visible. Acquisition time was 3 minutes. *Bottom row*: The phase of the OMRI image is more sensitive to free radical concentration than the magnitude. Signal in the blue regions have the opposite phase of the surrounding tissue, a signature of the Overhauser effect, and thus the presence of free radicals. *OMRI and Reference Images* were taken with the same b-SSFP sequence parameters: TE/TR = 25/50 ms, voxel size = $1.1 \times 1.6 \times 8$ mm, matrix size = $128 \times 35 \times 10$. The OMRI image was acquired with NA = 10 while the reference image was acquired with NA = 80.

Due to the protocol in place at the time of this pilot study, this experiment was performed on a rat sacrificed just prior to imaging. No attempt, therefore, was made to limit SAR. Before imaging live animals, it is important to determine if the heating caused by the EPR irradiation is sufficiently low. To estimate the heating, a second rat was sacrificed according to Cenk Ayata's protocol. The rat head was then immediately removed, brought to the laboratory, and placed inside the OMRI setup shown in Figure 59 above. A fiber optic temperature probe was placed into the brain

of the rat and the temperature was recorded during an OMRI experiment. The same sequence described in Figure 60 was used. Figure 61 shows the change in temperature over the course of the experiment for three different RF power levels. A $\Delta T < 2^\circ\text{C}$ over the imaging experiment is estimated to be acceptable given that there is no blood flow to help cool the brain in this experiment. The EPR coil could handle a maximum input power of about 10.3 W forward power, but this power caused too much heating in the brain and is deemed unsafe. At 6.5 W forward power, the temperature increased 2.1°C in 300 s, and thus is very close to the maximum power that may be acceptable. However, the acquisition time can be decreased to ~ 150 s by implementing 50% undersampling. At 150 s, the heating using 6.5 W forward power was 1.5°C . Again, because this represents an upper limit, we believe this is an acceptable power to use for initial live animal experiments.

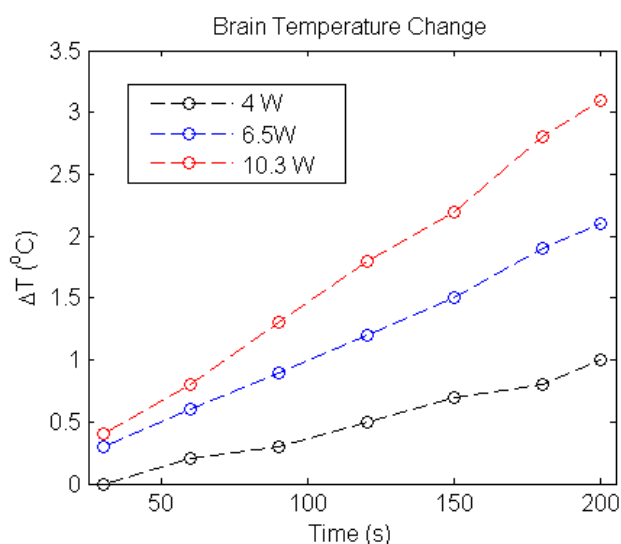


Figure 61: Plot of the temperature change in the brain of a decapitated rat vs. time during an OMRI sequence at various power. No actual imaging was performed. The sequence was run to determine a safe power level for EPR irradiation. The b-SSFP OMRI sequence has been previously described and used $TE/TR = 25/50$ ms.

KEY RESEARCH ACCOMPLISHMENTS:

Electromagnet LFI:

- Designed, constructed, and characterized high-efficiency single channel spiral “helmet” for human head imaging at 6.5 mT
- Constructed non-magnetic subject table suitable imaging in human subjects
- Acquired high-quality head images from human subjects with $3 \times 3 \times 10$ mm resolution in 29 minutes

- Compared brain images obtained at 6.5 mT with images obtained at 1.5 T

Permanent magnet Halbach LFI:

- Automated magnet rotation with stepper motor under pulse sequence control
- Integrated Halbach magnet and rotation assembly in a lightweight RF Faraday shield
- Developed high-performance probe array for field mapping critical for reconstruction
- Acquired single-channel 2D images of test phantoms to optimize reconstruction
- Modeled angular dependence of array coil B1 profiles critical for multichannel image reconstruction
- Acquired and reconstructed multi-channel 2D images of test phantoms and fruit
- Simulated ultimate attainable image resolution in Halbach encoding field
- Simulated TRASE array to enable 3D encoding

Parallel imaging in electromagnet LFI

- Evaluated accelerated imaging in new structured phantoms
- Designed, built, and evaluated 8-channel “helmet” Rx array for head imaging at 276 kHz
- Acquired the first 8-channel human head MRI image in the Johnson noise regime
- Evaluated optimal coil element orientation
- Evaluated several multi-channel decoupling strategies suitable at low frequency

System control and image acquisition in electromagnet LFI

- Integrated TNMR/MATLAB pulse sequence control and processing pipeline is stable
- Developed and implemented k -space mapping pulse sequences
- Implemented spiral imaging and image reconstruction
- Implemented “magnetic resonance fingerprinting” and Bloch simulation engine
- Migrated 8-channel SENSE reconstruction to a new optimized reconstruction code

Overhauser MRI in electromagnet LFI:

- Designed and simulated improved free radical detection methodology using interleaved OMRI/MRI acquisition
- Acquired the first accelerated images combining SENSE and OMRI
- Measured the decay of free radical in TEMPO bound to albumin in rodent blood
- Designed and built combined MRI/OMRI probe for rodent imaging
- Acquired 10 slice, $1.1 \times 1.6 \times 8$ mm in-plane resolution MRI and OMRI in *ex vivo* rats
- Measured temperature rise due to OMRI sequence in tissue sample

REPORTABLE OUTCOMES:

1. M Sarracanie, BD Armstrong, and MS Rosen, “High speed 3D b-SSFP at 6.5 mT”, presented at the *2013 Experimental NMR Conference*, 14–19 April 2013, Pacific Grove, CA.
2. BD Armstrong, M Sarracanie, J Stockman, and MS Rosen, “High speed 3D Overhauser-enhanced MRI using combined b-SSFP and compressed sensing”, presented at the *2013 Experimental NMR Conference*, 14–19 April 2013, Pacific Grove, CA.
3. CD LaPierre, M Sarracanie, LL Wald, and MS Rosen, “Parallel imaging and acceleration in the Johnson noise dominated regime”, presented at the *2013 Experimental NMR Conference*, 14–19 April 2013, Pacific Grove, CA.
4. CZ Cooley, JP Stockman, BD Armstrong, MS Rosen, and LL Wald, “A lightweight, portable MRI brain scanner based on a rotating Halbach magnet”, presented at the *2013 Experimental NMR Conference*, 14–19 April 2013, Pacific Grove, CA.
5. M Sarracanie, BD Armstrong, and MS Rosen, “High speed 3D b-SSFP at 6.5 mT”, presented at the *2013 International Society for Magnetic Resonance in Medicine*, 20–26 April 2013, Salt Lake City, UT.
6. BD Armstrong, M Sarracanie, JP Stockman, and MS Rosen, “High speed 3D Overhauser-enhanced MRI using combined b-SSFP and compressed sensing”, presented at the *2013 International Society for Magnetic Resonance in Medicine*, 20–26 April 2013, Salt Lake City, UT.
7. CD LaPierre, M Sarracanie, LL Wald, and MS Rosen, “Parallel imaging and acceleration in the Johnson noise dominated regime”, presented at the *2013 International Society for Magnetic Resonance in Medicine*, 20–26 April 2013, Salt Lake City, UT.
8. CZ Cooley, JP Stockman, BD Armstrong, MS Rosen, and LL Wald, “A lightweight, portable MRI brain scanner based on a rotating Halbach magnet”, presented at the *2013 International Society for Magnetic Resonance in Medicine*, 20–26 April 2013, Salt Lake City, UT.
9. JP Stockman, CZ Cooley, MS Rosen, and LL Wald, “Flexible spatial encoding strategies using rotating multipolar fields for unconventional MRI applications”, presented at the *2013 International Society for Magnetic Resonance in Medicine*, 20–26 April 2013, Salt Lake City, UT.

10. MS Rosen, invited seminar, “High performance low-field MRI: fact or fiction?”, Southern Illinois University, Department of Chemistry and Biochemistry, Carbondale IL, 8 March 2013.
11. MS Rosen, invited talk, “Free Radical MRI”, *MGH/NSF Physics of Cancer Imaging Workshop*, MGH/A.A. Martinos Center, 6 November 2013.
12. Six abstracts accepted for presentation in 2014 that result from research presently funded in the Rosen lab by DoD/DMRDP are attached below as **Appendices 2–7**.
13. M Sarracanie, BD Armstrong, JP Stockman, and MS Rosen, “High Speed 3D Overhauser-enhanced MRI using combined b-SSFP and Compressed Sensing”, published in *Magnetic Resonance in Medicine*, 2014; 71(2):735–45, attached as Appendix 8.
14. CZ Cooley, JP Stockman, BD Armstrong, M Sarracanie, MH Lev, MS Rosen, and LL Wald, “2D Imaging in a Lightweight Portable MRI Scanner without Gradient Coils”, accepted for publication, *Magnetic Resonance in Medicine*, 2014, attached as Appendix 9
15. Funding applied for: NIH R21 NS087344-01 (PI Rosen), “Non-invasive Free Radical MRI in Stroke”, 2013.
16. Funding applied for NIH R01 EB018976-01 (PI Wald), “Technology for Portable MRI”, 2013.
17. Funding applied for: GE/NFL Head Health Challenge I (two proposals), 2013.
18. Funding applied for: GE/NFL Head Health Challenge II (one proposal), 2014.

CONCLUSION:

The reason MRI is not widely deployable is that high-strength magnetic fields (of order 1 T) are necessary with conventional MRI to obtain useful brain images. Such high field scanners involve large, heavy, fragile, expensive equipment (such as superconducting magnets) that are difficult to site in field hospitals. We contend that that low-magnetic-field implementations of MRI can be developed to allow robust, transportable imaging modalities well suited to diagnose the types of battlefield injuries prevalent in TBI and practical for operation in field hospitals. Application of the suite of techniques and technologies from our work could advise future development of a deployable device with a high diagnostic impact and could be transformative, enabling improved diagnosis and monitoring of battlefield injuries prevalent in TBI.

The electromagnet LFI provides an ideal state-of-the art test bed for all of the novel acquisition, detection methodologies, and reconstruction algorithms including navigators and sparse sam-

pling, and additionally will provide necessary experience and data to advise optimal construction and magnetic field for any future electromagnet-based deployable systems. In its current configuration, this state-of-the-art scanner enables high-performance spectroscopy and 8-channel imaging at 6.5 mT, and is fully equipped for Overhauser DNP experiments. We continue to improve the ability to acquire images based on the intrinsic ^1H signal by combining new low-field hardware methodology and advanced pulse sequence and reconstruction methods.

Our second low field imaging test bed, the permanent magnet Halbach LFI is based around a lightweight (45 kg) and portable magnet with a built-in encoding field for MRI. It is a highly specialized and potentially disruptive scanner that could greatly ease both the cost and burden of a field-forward instrument purpose-built for TBI imaging. The 2D imaging results acquired in the highly inhomogeneous magnetic field of the Halbach scanner using simultaneous NMR measurement to track magnet drift, and multi-channel receive arrays to unwrap image aliasing, and are encouraging. A truly portable MR system based on this technology has the potential to quickly detect brain injury at the site of injury, for instance in an ambulance prior to transportation to the hospital.

We have also been developing technology for a wholly new approach to brain imaging that may revolutionize the use of MRI for the assessment and treatment of secondary brain injury following TBI: direct tomographic detection of endogenous free radicals as an early marker for TBI. This new form of contrast, “injury-sensitive MRI”, is based on the enormous signal enhancement attainable with Overhauser DNP, converting the electron spin of endogenous free radicals into nuclear polarization using the Overhauser effect and subsequently imaging that modified nuclear polarization using low-field MRI (OMRI).

Much of the hardware development for the human head LFI test bed systems (**Aim 1**) and for the OMRI system (**Aim 2**) was completed in Y1. Progress in Y2 for Aim 1 focused on imaging sequence development and optimization, and implementation of parallel imaging acceleration. Aim 2 efforts included work to maximizing the OMRI signal attainable from free-radical test solutions with a minimum of applied Overhauser power. In Y3, we have successfully demonstrated the first 3D human brain imaging in the 6.5 mT electromagnet LFI, and the first 2D imaging in the 100 lb permanent magnet based LFI. We have also demonstrated Overhauser-enhanced MRI in a pilot study in rodents *ex vivo* as a step toward the measurement of free radicals *in vivo*.

The imaging experiments presented above in the optimized electromagnet LFI are compelling: high quality ^1H brain MRI at 6.5 mT is in fact attainable over reasonable averaging times using high performance hardware and advanced MRI sequences. A critical question for this work is the understanding of the clinical balance and impact that the tradeoff between acquisition time and resolution implicit in imaging plays on the operation of a deployable scanner.

The low-field OMRI results presented above demonstrate promise for high-speed high-resolution free-radical imaging, and offers new perspectives for the measurement of free radicals in living organisms. The long-term goal of this work is an *in vivo* implementation of this technique. Free-radical sensitive low-field OMRI as a novel imaging and diagnostic MRI-based method with specificity to secondary-injury has the potential to clarify the mechanisms involved in secondary damage and the local effects of novel therapies. Time-critical imaging of free radicals can provide the unique interventional access critically needed for drug therapies and this technique would fill the clear need for an “injury imager”, suitable for non-invasive tomographic measurement (Figure 62).

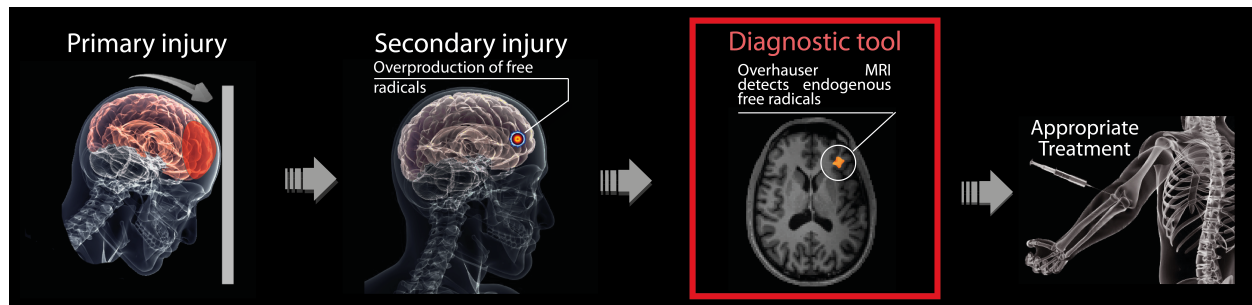


Figure 62: Schematic of the development of a new interventional imaging and treatment tool for *in vivo* detection of endogenous free radicals associated with secondary injury following TBI using low-field OMRI as developed here. This same approach can similarly open up new treatment windows into stroke and other ischemic events. MRI-based *in vivo* free radical imaging using OMRI is impossible at high-field due to the inability of the ESR pulse to penetrate into tissue, and the danger of RF heating in the microwave regime.

Successful demonstration of this system *in vivo* will provide image-based injury specificity for TBI and for the first time open a window into a critical mechanism of TBI-related disease and an unambiguous non-invasive *in vivo* marker for cerebral injury. Time-critical imaging of free radicals associated with secondary imaging can provide the unique interventional access critically needed to develop and deliver drug therapies to mitigate brain damage, reducing disability and death from secondary injury following TBI. The low-field approach would allow placement of this critical new diagnostic “injury imager” tool close to the source of injury—as well as in hospitals and clinics where rehabilitation takes place.

REFERENCES:

- [1] C. D. LaPierre, M. Sarraçanie, L. L. Wald, and M. S. Rosen, “Parallel imaging and acceleration in the Johnson noise dominated regime,” presented at the Proc. Intl. Soc. Mag. Reson. Med., Salt Lake City, UT, 2013, p. 2772.
- [2] S. M. Wright, R. L. Magin, and J. R. Kelton, “Arrays of mutually coupled receiver coils: theory and application,” *Magnetic Resonance in Medicine*, vol. 17, no. 1, pp. 252–268, 1991.

- [3] J. Jevtic, "Ladder Networks for Capacitive Decoupling in Phased-Array Coils," presented at the Proc. Intl. Soc. Mag. Reson. Med., 2001, vol. 9, p. 17.
- [4] J. Wang, "A novel method to reduce the signal coupling of surface coils for MRI," presented at the Proc Int. Soc. Magn. Reson. Med, 1996, p. 1434.
- [5] H. T. Hui, "An effective compensation method for the mutual coupling effect in phased arrays for magnetic resonance imaging," IEEE Trans. Antennas Propagat., vol. 53, no. 11, pp. 3576–3583, Nov. 2005.
- [6] A. Reykowski, C. Saylor, and G. R. Duensing, "Do We Need Preamplifier Decoupling?," presented at the Proc. Intl. Soc. Mag. Reson. Med., 2010, vol. 19, p. 3883.
- [7] R. F. Lee, R. O. Giaquinto, and C. J. Hardy, "Coupling and decoupling theory and its application to the MRI phased array," Magnetic Resonance in Medicine, vol. 48, no. 1, pp. 203–213, 2002.
- [8] P. B. Roemer, W. A. Edelstein, C. E. Hayes, S. P. Souza, and O. M. Mueller, "The NMR phased array," Magnetic Resonance in Medicine, vol. 16, no. 2, pp. 192–225, 1990.
- [9] P. J. Ledden and S. Inati, "Four channel preamplifier decoupled phased array for brain imaging at 1.5T," presented at the Proc. Intl. Soc. Magn. Reson. Med, 2001, p. 1117.
- [10] B. Inglis, K. Buckenmaier, P. SanGiorgio, A. F. Pedersen, M. A. Nichols, and J. Clarke, "MRI of the human brain at 130 microtesla," Proceedings of the National Academy of Sciences, vol. 110, no. 48, pp. 19194–19201, Nov. 2013.
- [11] K. Scheffler and S. Lehnhardt, "Principles and applications of balanced SSFP techniques," European Radiology, vol. 13, no. 11, pp. 2409–2418, Nov. 2003.
- [12] M. Lustig, D. L. Donoho, J. M. Santos, and J. M. Pauly, "Compressed sensing MRI," IEEE Signal Process. Mag., vol. 25, no. 2, pp. 72–82, 2008.
- [13] M. Lustig, D. Donoho, and J. M. Pauly, "Sparse MRI: The application of compressed sensing for rapid MR imaging," Magnetic Resonance in Medicine, vol. 58, no. 6, pp. 1182–1195, 2007.
- [14] B. A. Hargreaves, D. G. Nishimura, and S. M. Conolly, "Time-optimal multidimensional gradient waveform design for rapid imaging," Magnetic Resonance in Medicine, vol. 51, no. 1, pp. 81–92, 2004.
- [15] H. Schomberg and J. Timmer, "The gridding method for image reconstruction by Fourier transformation," Medical Imaging, IEEE Transactions on, vol. 14, no. 3, pp. 596–607, 1995.
- [16] J. G. Pipe and P. Menon, "Sampling density compensation in MRI: Rationale and an iterative numerical solution," Magnetic Resonance in Medicine, vol. 41, no. 1, pp. 179–186, Jan. 1999.
- [17] M. Lustig and J. M. Pauly, "SPIRiT: Iterative self-consistent parallel imaging reconstruction from arbitrary k-space," Magnetic Resonance in Medicine, vol. 64, no. 2, pp. 457–

- 471, 2010.
- [18] J. H. Duyn, Y. Yang, J. A. Frank, and J. W. van der Veen, "Simple Correction Method for k-Space Trajectory Deviations in MRI," *Journal of Magnetic Resonance*, vol. 132, no. 1, pp. 150–153, 1998.
 - [19] D. Ma, V. Gulani, N. Seiberlich, K. Liu, J. L. Sunshine, J. L. Duerk, and M. A. Griswold, "Magnetic resonance fingerprinting," *Nature*, vol. 495, no. 7440, pp. 187–192, Mar. 2013.
 - [20] G. Schultz, P. Ullmann, H. Lehr, A. M. Welz, J. Hennig, and M. Zaitsev, "Reconstruction of MRI data encoded with arbitrarily shaped, curvilinear, nonbijective magnetic fields," *Magnetic Resonance in Medicine*, vol. 64, no. 5, pp. 1390–1403, Sep. 2010.
 - [21] C. Barmet, N. D. Zanche, and K. P. Pruessmann, "Spatiotemporal magnetic field monitoring for MR," *Magnetic Resonance in Medicine*, vol. 60, no. 1, pp. 187–197, Jul. 2008.
 - [22] J. C. Sharp and S. B. King, "MRI using radiofrequency magnetic field phase gradients," *Magnetic Resonance in Medicine*, vol. 63, no. 1, pp. 151–161, Jan. 2010.
 - [23] J. C. Sharp, S. B. King, Q. Deng, V. Volotovskyy, and B. Tomanek, "High-resolution MRI encoding using radiofrequency phase gradients," *NMR in Biomedicine*, vol. 26, no. 11, pp. 1602–1607, Jan. 2013.
 - [24] L. C. Bell, E. T. Peterson, S. B. Fain, and K. N. Kurpad, "Dual-tuned $^1\text{H}/^{13}\text{C}$ orthogonal double solenoid volume coil for simultaneous acquisition in small animals in vivo," presented at the Proc Int. Soc. Magn. Reson. Med, 2011, p. 1894.
 - [25] J. Bellec, S. B. King, C.-Y. Liu, and C. P. Bidinosti, "Target Field Based RF Phase Gradient Transmit Array for 3D TRASE MRI," presented at the Proc Intl Soc Mag Res Med, 2013, vol. 21, p. 0138.
 - [26] E. Danieli, J. Perlo, B. Blümich, and F. Casanova, "Highly Stable and Finely Tuned Magnetic Fields Generated by Permanent Magnet Assemblies," *Phys. Rev. Lett.*, vol. 110, no. 18, p. 180801, Apr. 2013.
 - [27] P. Perona and J. Malik, "Scale-space and edge detection using anisotropic diffusion," *IEEE Trans. Pattern Anal. Machine Intell.*, vol. 12, no. 7, pp. 629–639, Jul. 1990.
 - [28] M. J. Ahn, E. R. Sherwood, D. S. Prough, C. Yie Lin, and D. S. DeWitt, "The effects of traumatic brain injury on cerebral blood flow and brain tissue nitric oxide levels and cytokine expression," *Journal of Neurotrauma*, vol. 21, no. 10, pp. 1431–1442, 2004.
 - [29] X. Zheng, K. Liu, and Y. Yang, "Real-Time Measurement of Murine Hippocampus Hippocampus NO Levels in Response to Cerebral Ischemia/Reperfusion Reperfusion," in *Nitric oxide methods and protocols*, vol. 704, no. 6, Totowa, NJ: Humana Press, 2010, pp. 73–80.
 - [30] T. Malinski, F. Bailey, Z. G. Zhang, and M. Chopp, "Nitric oxide measured by a porphyrinic microsensor in rat brain after transient middle cerebral artery occlusion," *Journal of Cerebral Blood Flow & Metabolism*, vol. 13, no. 3, pp. 355–358, 1993.

- [31] C. Iadecola, "Bright and dark sides of nitric oxide in ischemic brain injury," *Trends in neurosciences*, vol. 20, no. 3, pp. 132–139, 1997.
- [32] L. Cherian, J. C. Goodman, and C. S. Robertson, "Brain nitric oxide changes after controlled cortical impact injury in rats," *Journal of neurophysiology*, vol. 83, no. 4, pp. 2171–2178, 2000.
- [33] L. Cherian, J. C. Goodman, and C. Robertson, "Neuroprotection with Erythropoietin Administration Following Controlled Cortical Impact Injury in Rats," *Journal of Pharmacology and Experimental Therapeutics*, vol. 322, no. 2, pp. 789–794, May 2007.
- [34] P. A. Rashid, A. Whitehurst, N. Lawson, and P. M. W. Bath, "Plasma nitric oxide (nitrate/nitrite) levels in acute stroke and their relationship with severity and outcome," *Journal of Stroke and Cerebrovascular Diseases*, vol. 12, no. 2, pp. 82–87, Mar. 2003.
- [35] K. L. Carpenter, I. Timofeev, P. G. Al-Rawi, D. K. Menon, J. D. Pickard, and P. J. Hutchinson, "Nitric oxide in acute brain injury: a pilot study of NO(x) concentrations in human brain microdialysates and their relationship with energy metabolism.," vol. 102, pp. 207–13, Jan. 2008.
- [36] S. Huettel, A. Song, and G. McCarthy, *Functional Magnetic Resonance Imaging*. {Sinauer Associates}, 2004.
- [37] J. Mispelter, M. Lupu, and A. Briguët, *NMR probeheads for biophysical and biomedical experiments : theoretical principles & practical guidelines*. London : Imperial College Press ; Hackensack, NJ : Distributed by World Scientific,, 2006.
- [38] M. Sarraçanie, B. D. Armstrong, J. Stockmann, and M. S. Rosen, "High speed 3D overhauser-enhanced MRI using combined b-SSFP and compressed sensing," *Magnetic Resonance in Medicine*, vol. 71, no. 2, pp. 735–745, 2014.

APPENDICIES:

Year 3 Statement of Work

We attach for reference the Year 3 SOW as **Appendix 1**.

Abstracts accepted for presentation

We attach six abstracts (**Appendices 2–7**) accepted for presentation in 2014 that result from research presently funded in the Rosen lab by DoD/DMRDP. Abstracts marked with a ‡ will be presented as a poster at the 55th Experimental NMR Conference (ENC) to take place 23–28 March 2014 in Boston, MA, and abstracts marked with a § will be presented as a poster at the 23rd Annual Meeting of the International Society for Magnetic Resonance in Medicine (ISMRM) to take place 10–16 May 2014 in Milan, Italy. A symbol printed in red indicates that the abstract will be presented as a talk.

1. ‡§ High speed MR fingerprinting at 6.5 mT
2. ‡§ An optimized 8-channel helmet array for head imaging at 6.5 mT
3. ‡§ Overhauser-enhanced MRI with SENSE acceleration in the Johnson noise dominated regime
4. ‡§ Overhauser-enhanced MRI as a non-invasive probe of BBB breakdown and redox state following ischemia/reperfusion
5. § Spatial resolution in rotating spatial encoding magnetic field MRI (rSEM-MRI)
6. ‡§ 2D imaging in a portable MRI scanner without gradient coils

Manuscripts published/accepted for publication

We attach as **Appendix 8** our manuscript “High Speed 3D Overhauser-enhanced MRI using combined b-SSFP and Compressed Sensing”, published in *Magnetic Resonance in Medicine* 2014. We also attach as **Appendix 9** our manuscript “2D imaging in a lightweight portable MRI scanner without gradient coils”, currently in press in *Magnetic Resonance in Medicine*.

Y3 1. Low Field Imager		
Q1-4	1A Low-field MRI Hardware Development	OPTIMIZATION of low-field head MRI system hardware performance.
Q1-4	1B System Control and Image Acquisition	OPTIMIZATION of image navigation and reconstruction methods.
Q3-4	1C Demonstration of Head Imager	<p>DEMONSTRATION of low-field proton MRI in head-shaped phantoms (including normal and realistic TBI phantoms).</p> <p>COMPARISON of low-field images of head-shaped phantoms with images acquired with a commercial high-field (1.5 T) MRI system.</p> <p>INTEGRATION and TESTING of OEPS system (from Task 2) with low-field head imager using samples of NO-Hb and free-NO in aqueous solution.</p>
Y3 2. OMRI injury imaging		
Q1-4	2A OMRI Hardware Development	OPTIMIZATION of OMRI system sensitivity based on findings from subtasks 2B and 2C.
Q1-4	2C <i>Ex Vivo</i> “Gold Standard” for NO Detection	<p>DETERMINATION of relevant sensitivity window for NO detection in TBI phantom.</p> <p>VALIDATION of sensitivity of PGS at physiologically relevant NO levels in TBI phantom.</p>

YEAR 3 DELIVERABLES: Detailed technical reports on final design and performance characterization of the low-field human head imager and the OMRI system for imaging Overhauser-enhanced free radicals.

High Speed MR Fingerprinting at 6.5 mT

Mathieu Sarraclanie^{1,2}, Brandon D. Armstrong^{1,2} and Matthew S. Rosen^{1,2,3}

¹A. A. Martinos Center for Biomedical Imaging, 149 13th St., Suite 2301, Boston, MA. 02129, ²Department of Physics, Harvard University, 17 Oxford St. Cambridge, MA. 02138, ³Harvard Medical School, 25 Shattuck St, Boston, MA. 02115

High-field MRI instruments offer limited utility in field deployable and portable contexts. Our effort focuses on the critical challenges that must be solved to enable deployment of transportable MRI systems. In recent work [1], we demonstrated high performance MRI at low magnetic field by making use of high-efficiency steady state free precession techniques (b-SSFP) [2] and undersampling for compressed sensing MRI. Earlier in 2013, a new imaging technique termed "magnetic resonance fingerprinting" (MRF) was proposed [3]. Unlike all other MRI sequence strategies, MR Fingerprinting allows the simultaneous quantification of multiple properties of a material or tissue in a single acquisition. In the present work, we show the first implementation of MR Fingerprinting at very low magnetic field in a multi-compartment phantom.

MRF at low magnetic field creates a rapid dynamic series of low signal to noise ratio (SNR) images where the magnitude of each voxel of each image changes at every time step. The TR and flip angle of each image in the time series is varied pseudo-randomly [5]. No steady state is reached, and image voxels with different relaxation times evolve differently, thereby generating unique magnetization trajectories. The time evolution of each voxel is simulated offline using the Bloch equations with the TR and flip angle patterns used for the imaging sequence over a wide range of tissue parameters, and a database (dictionary) of trajectories is generated. The measured voxel trajectory is compared to the dictionary and the best match is chosen, identically providing the T_1 , T_2 , and off-resonance frequency value of that voxel. Lack of SNR at low magnetic field required redesigning our sequence to lower undersampling rates and bigger flip angle range. The resulting sequence is a 200 time points, 50% undersampled, slice-selective 20 spirals sequence. After an inversion pulse, flip angle ranges between 30 and 107°, TR varies between 46.1 ms and 52.7 ms. The dictionary was made of 2,751,975 signal time courses, each with 200 time points. MR total acquisition time was 13 min. The sequence was set with voxel size: $3 \times 3 \times 10 \text{ mm}^3$, FOV: $144 \times 144 \times 10 \text{ mm}^3$, number of average (NA): 6. The low field MRI scanner was previously described [6].

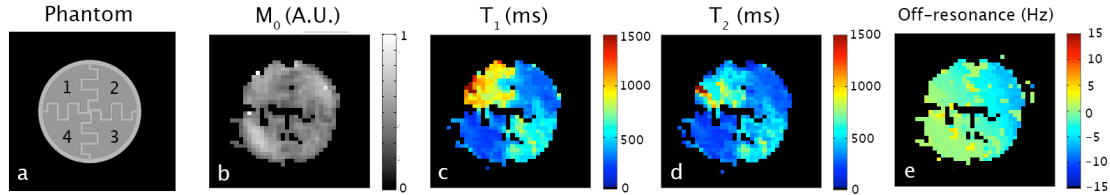


Figure 1: Slice selective MRF results obtained at 6.5 mT. The four-compartment liquid filled structured phantom shown schematically in (a). The compartments vary in relaxation properties. Each compartment had T_1 and T_2 measured in separate reference experiments (Inversion recovery & T2 CPMG respectively). 1: $T_1=1046 \text{ ms}$, $T_2=700 \text{ ms}$, 2: $T_1=425 \text{ ms}$, $T_2=418 \text{ ms}$, 3: $T_1=600 \text{ ms}$, $T_2=591 \text{ ms}$, 4: $T_1=340 \text{ ms}$, $T_2=286 \text{ ms}$. **b-e** show M_0 , T_1 , T_2 , and off-resonance frequency, respectively.

Each image generated in the reconstructed fingerprinting set (Figure 1 b-e) reveals different information. The spin density (M_0) map of Figure 1.a is equivalent to traditional b-SSFP, and no visible difference between compartments is seen. However, Figure 1. c-d reveals that compartments 1-4 have very different T_1 and T_2 relaxation properties. The MRF images show good agreement with the reference measurements. Additionally, a map of the magnetic field homogeneity of the LFI scanner is also generated during the MRF sequence (Figure 1.e).

We have demonstrated MR Fingerprinting at low magnetic field, which results in simultaneous measurement of 4 quantitative parameters, and thus provides 4 different image contrasts in a single acquisition (proton density, T_1 , T_2 and off-resonance) in less than 15 minutes. This technique is of particular relevance at low magnetic field where SNR and contrast are tied to long acquisition times. The combination of MRF with low field MRI scanners has great potential to revolutionize future transportable MRI systems.

References: [1] Sarraclanie M *et al.* ISMRM 2013 #5322; [2] Scheffler K *et al.* Eur Radiol 2003 13:2409-18; [3] Ma D *et al.* Nature 2013 495:187-193; [4] Perlin K *et al.* Comput Graphics 1985 19:287-296; [6] Tsai LL *et al.* JMR 2008; 193:174-85.

Acknowledgement: This research was supported by the Department of Defense, Defense Medical Research and Development Program, Applied Research and Advanced Technology Development Award W81XWH-11-2-0076 (DM09094).

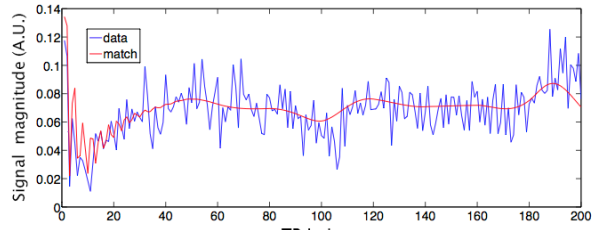


Figure 2: The magnetization trajectory of a single typical voxel over the 200 image fingerprinting sequence is shown (blue: data, red: best match from dictionary). All the parameters of the voxel (M_0 , T_1 , T_2 , and off-resonance frequency) are determined once the trajectory match is

An Optimized 8-Channel Helmet Array for Head Imaging at 6.5 mT

Cristen D. LaPierre^{1,2}, Mathieu Sarraçanie^{1,2}, Lawrence L. Wald^{1,3,4}, Matthew S. Rosen^{1,2,3}

¹A. A. Martinos Center for Biomedical Imaging, Department of Radiology, Massachusetts General Hospital, Charlestown, MA, ²Department of Physics, Harvard University, Cambridge, MA, ³Harvard Medical School, Boston, MA, ⁴Harvard-MIT Division of Health Sciences and Technology, Cambridge, MA

In many traumatic brain injury situations, time-critical diagnostic imaging is needed to properly triage and begin treatment. However, in some scenarios access to conventional MRI scanners is limited, owing in part to their siting requirements. A very low-field imager could enable a potentially transportable and rapidly deployable human imaging system free from many of the system requirements of high-field scanners. We previously demonstrated an eight-channel array [1] for our 6.5 mT electromagnet based scanner [2] capable of imaging objects up to 15.6 cm in diameter and implemented SENSE. The present work demonstrates parallel imaging *in vivo* in the human head with an optimized 8-channel array.

A tight fitting helmet was designed and 3D printed in-house (Fig. 1). Eight 30-turn receive-only coils (24 AWG, 4x12 cm and 4x14 cm loops) were tiled symmetrically about the sagittal plane. All coils were tuned to 276.0 kHz and were matched to at least -27 dB and geometrically decoupled from their nearest neighbors by at least -30 dB. Decoupling from next-nearest neighbors was at least -6 dB. A 30 cm diameter solenoid was used for transmit. Passive decoupling between transmit and receive was achieved using crossed diodes in series with transmit, and in parallel with receive.

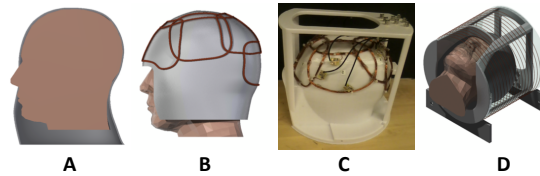


Figure 1: An 8Ch array designed as a tight-fitting helmet (gray) to an anatomically-correct CAD model of the human head (A), tiling of 8 receive-only coils (B) and construction on a 3D printed helmet. D) final assembly modeled in the 30 cm transmit coil.

Axial (Fig. 2.A) and sagittal (Fig. 2.B) images were acquired using a 3D b-SSFP sequence with 50% incoherent undersampling of k-space at 6.5 mT (276 kHz). Imaging parameters were: TR/TE = 33.2/21.6 ms, acquisition matrix = (64x64x9), voxel size = (3x3x6) mm³, number of averages (NA) = 200, and flip angle = 70°. The readout duration was 7.04 ms with a 9091 Hz bandwidth. The total acquisition time was 30 min. Both figures reveal recognizable anatomic features in the head including the skull, cortical structures (gyri/sulci) and the corpus callosum.

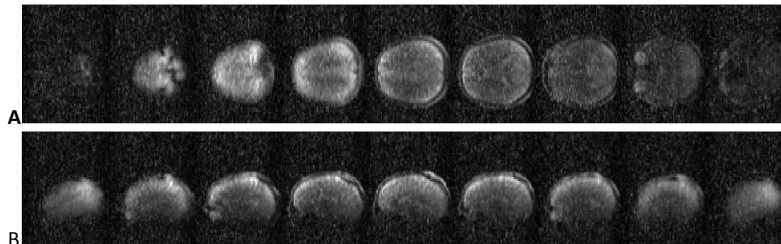


Figure 2: 3D b-SSFP performed *in vivo* in a human head in A. axial and B. sagittal orientation using the optimized 8-channel helmet array at 6.5 mT (276 kHz ¹H frequency). Magnitude images are shown. Voxel size was (3.3x4x17) mm³. Total acquisition time was 30 min.

We have demonstrated that an optimized 8-channel helmet array combined with fast acquisition techniques and undersampling strategies enables 3D imaging at very low field *in vivo*. With (3.3x4x17) mm³ total voxel size, we obtain 2 times greater spatial resolution than very recently published work using a SQUID detector in an ultra-low field MRI system with a 80 mT prepolarization field [3]. In addition, our 3D dataset (9 slices) was acquired more than seven times faster than the single slice 2D brain dataset of the SQUID-detected work. Future work will focus on improved coil decoupling schemes in this very-low-field regime as well as additional image acceleration techniques such as SENSE.

Acknowledgements: This work supported by the Department of Defense, Defense Medical Research and Development Program, Applied Research and Advanced Technology Development Award W81XWH-11-2-0076 (DM09094).

References: 1. LaPierre, M Sarraçanie, LL Wald, MS Rosen. *Proc. Intl. Soc. Mag. Reson. Med.* 21 (2013) 2772., 2. LL Tsai, RW Mair, MS Rosen, S Patz, RL Walsworth. An open-access, very-low-field MRI system for posture-dependent ³He human lung imaging. *J Magn Reson.* 193(2): 274-85 (2008)., 3. B Inglis, K Buckenmaier, P SanGiorgio, AF Pedersen, MA Nichols, J Clarke. MRI of the human brain at 130 microtesla. *PNAS* (Nov. 2013). doi: 10.1073/pnas.1319334110.

Overhauser-enhanced MRI with SENSE Acceleration in the Johnson Noise Dominated Regime

Cristen D. LaPierre^{1,2}, Mathieu Sarraclanie^{1,2}, Brandon Armstrong^{1,2}, Jonathan R. Polimeni^{1,3}, Matthew S. Rosen^{1,2,3}

¹A.A. Martinos Center for Biomedical Imaging, Department of Radiology, Massachusetts General Hospital, Charlestown, MA, ²Department of Physics, Harvard University, Cambridge, MA, ³Harvard Medical School, Boston, MA

MRI at low magnetic fields is time consuming owing to small Boltzmann polarization and consequently low signal. Enhancement techniques such as Dynamic Nuclear Polarization (DNP), and image acceleration techniques like SENSitivity Encoding (SENSE) are compelling tools to obtain high-quality images in reasonable times. The present work combines DNP with eight-channel parallel imaging at 6.5 mT.

Previously we constructed an 8-channel receive array¹ at 276 kHz for our 6.5 mT electromagnet-based scanner² and demonstrated SENSE reconstruction. This setup is now equipped to perform b-SSFP based Overhauser-MRI (OMRI)³. The 8-channel receive array nests inside a 14 cm diameter 140 MHz ESR saddle coil, which is placed inside a 30 cm diameter solenoid for NMR transmit at 276 kHz. An OMRI image of a 13 cm diameter structured phantom was acquired both with- and without SENSE acceleration (reduction factor $R=2$). Coil sensitivity profiles were acquired with the saddle coil in position but without DNP. A 3D balanced Steady State Free Precession (b-SSFP) sequence with full Cartesian acquisition of k -space was acquired with FOV=304×170×60 mm³, acquisition matrix=130×128×3, TE/TR=25.2/50.4 ms, number of acquisitions (NA)=35 except for (b) where NA=140.

Figure 1 shows the structured phantom (a) and images obtained without DNP or SENSE (b), with DNP but not SENSE (c) and using DNP and SENSE (d). The unenhanced image was acquired in 25.5 min. The DNP-only image was acquired in 11.5 min, and adding SENSE acceleration ($R=2$) reduced this time to 5.5 minutes at 6.5 mT.

Figure 2 shows the noise covariance matrix (a) and the correlation coefficient matrix (b) for the 8-channel array. The 8 channels are fairly well decoupled from each other. Channels 6 and 7 show increased mutual coupling—perhaps due to coupling via the EPR saddle coil.

With DNP alone, the SNR efficiency (SNR_{eff}) increased 23.4 fold while there was a 1.8 fold reduction in acquisition time. Combining DNP and SENSE, the SNR_{eff} decreased 22% and acquisition time decreased 4.6 fold. SNR_{eff} is max SNR in the sample normalized by the square root of NA.

These results represent the first use of DNP hyperpolarization combined with SENSE acceleration attained at 6.5 mT and represent important steps towards accelerating hyperpolarized imaging at low field. Future work will improve SENSE reconstruction as well as compare it to incoherent random undersampling strategies.

Acknowledgements: This work supported by the Department of Defense, Defense Medical Research and Development Program, Applied Research and Advanced Technology Development Award W81XWH-11-2-0076 (DM09094).

References: 1. CD LaPierre, M Sarraclanie, LL Wald, MS Rosen. *Proc. Intl. Soc. Mag. Reson. Med.* 21 (2013) 2772.

2. LL Tsai, RW Mair, MS Rosen, S Patz, RL Walsworth. An open-access, very-low-field MRI system for posture-dependent ³He human lung imaging. *J Magn Reson.* 193(2): 274-85 (2008)

3. M Sarraclanie, BD Armstrong, J Stockmann, MS Rosen. High speed 3D overhauser-enhanced MRI using combined b-SSFP and compressed sensing. *Magn Reson Med.* doi: 10.1002/mrm.24705

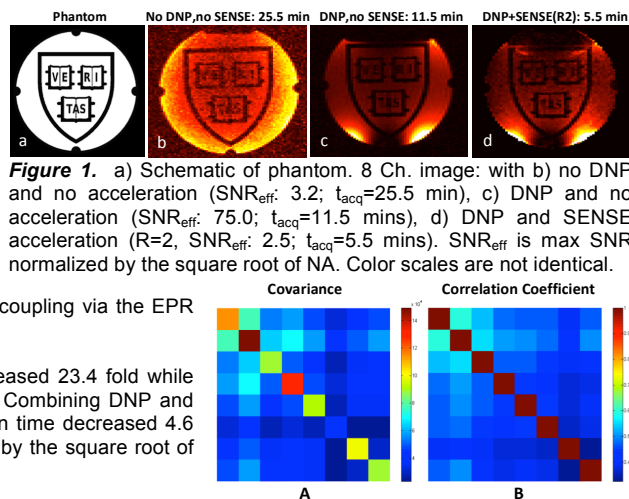


Figure 1. a) Schematic of phantom. 8 Ch. image: with b) no DNP and no acceleration (SNR_{eff} : 3.2; t_{acq} =25.5 min), c) DNP and no acceleration (SNR_{eff} : 75.0; t_{acq} =11.5 mins), d) DNP and SENSE acceleration ($R=2$, SNR_{eff} : 2.5; t_{acq} =5.5 mins). SNR_{eff} is max SNR normalized by the square root of NA. Color scales are not identical.

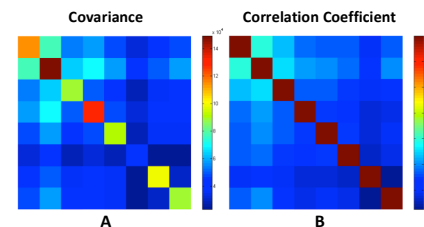


Figure 1. Noise covariance (a) and correlation coefficient (b) matrices for an 8-channel array assembled with NMR transmit and DNP saddle coils.

Overhauser-enhanced MRI as a Non-invasive Probe of BBB Breakdown and Redox State in Stroke

Matthew S Rosen^{1,2,3}, Mathieu Sarraclanie^{1,2}, Brandon D. Armstrong^{1,2}, Fanny Herisson⁴, Najat Salameh^{1,2,5}, Cenk Ayata⁴

¹A. A. Martinos Center for Biomedical Imaging, Dept. of Radiology, Massachusetts General Hospital, Charlestown, MA, USA, ²Dept. of Physics, Harvard University, Cambridge, MA, USA, ³Harvard Medical School, Boston, MA, USA,

⁴Neurovascular Research Lab, Dept. of Radiology, Massachusetts General Hospital, Charlestown, MA, USA, ⁵Institut de Physique des Systèmes Biologiques, EPFL, Lausanne, Switzerland.

Acute reperfusion therapies have changed ischemic stroke care, but treatments are limited because of a short therapeutic window owing to the risk of reperfusion injury and hemorrhage. Detection of early and mild BBB disruption is an unmet need in acute stroke diagnosis [1] and although contrast from relaxation-based MRI contrast agents such as Gd-DTPA is correlated with hemorrhagic transformation of an infarct, it is not sensitive enough to probe more mild BBB disruption [2]. Overhauser-enhanced MRI (OMRI) is a promising technique for imaging free radicals, and a recently developed fast high-resolution OMRI methodology [3] offers new perspectives for the imaging of free radicals in living organisms. We describe here a method to probe hyperacute BBB breakdown following ischemic stroke using OMRI in conjunction with an injected stable free radical.

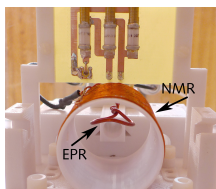


Figure 1: Probe for OMRI rat imaging at 6.5 mT: NMR@276 kHz, ESR@141 MHz.

TEMPOL (4-hydroxy-TEMPO) is detected by OMRI with very high sensitivity. In a normal physiological state, TEMPOL does not cross the BBB [4]. Because of its small size (172 Da) however, it may be able to cross the BBB under pathological circumstances associated with early BBB opening (e.g. ischemia), and act as an OMRI-detectable tracer. The use of TEMPOL as a small, exogenous OMRI agent would allow monitoring BBB disruption in stroke at the hyperacute stage, potentially much earlier than the traditional relaxation-based MRI contrast agents that rely on the leakage of larger molecules (such as Gd-DTPA) across the BBB.

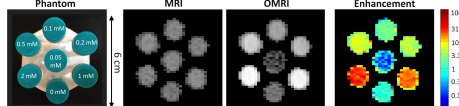


Figure 2: (left) Photo of TEMPOL concentration phantom All seven vials have very similar MRI magnitudes. OMRI demonstrates marked image-based free radical sensitivity.

tion-based MRI contrast agents that rely on the leakage of larger molecules (such as Gd-DTPA) across the BBB.

A custom built, low-field 6.5 mT MRI scanner was used in these experiments [5]. 3D OMRI was performed using an optimized sequence based around b-SSFP as described in [3]. Sensitivity of b-SSFP-based OMRI to free radical concentration was performed using the NMR/ESR coil setup of [3] using vials containing TEMPOL in concentrations from 50 mM–2 mM, and a control containing only water. A rat model of cerebral ischemia/reperfusion was used to test the ability of our technique to detect injected TEMPOL free radicals crossing the BBB *in vivo*. *In vivo* experiments were performed using

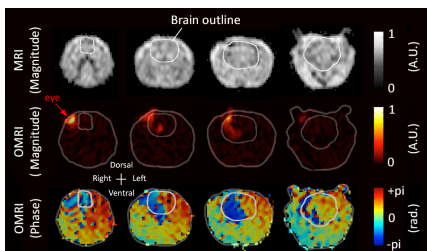


Figure 3: OMRI magnitude and phase images acquired from a rat at 6.5 mT following 75 min right MCAO and 60 min reperfusion. Four coronal slices from 10 slice data set shown. OMRI (NA=10) imaging time was 195 seconds. Low-resolution anatomical MRI (NA=80) was acquired in the OMRI scanner at 6.5 mT with DNP pulses disabled. MRI imaging time was 17 min. All images, voxel size: 1.1 x 1.6 x 8 mm³, TE/TR: 18/36 ms, Matrix: 128 x 35 x 10

with a single loop ESR coil inside a solenoid NMR coil (Figure 1). Under anesthesia, MCAO occlusion was performed in a 3 month old Wistar rat by insertion of filament via external carotid artery. Following 75 min MCAO and 60 min reperfusion, 3.6 μ l/gbw of 300 μ M TEMPOL was injected into the carotid artery after which the animal was sacrificed and OMRI imaging begun. The sensitivity of b-SSFP-based OMRI to free radical concentration is shown in Figure 2. The OMRI scan demonstrates marked image-based free radical sensitivity. The OMRI enhancement image is computed from the ratio of OMRI to MRI magnitude. *In vivo* OMRI signal enhancement in the frontal lobe and eye ipsilateral to the ischemic site is clearly visible in the OMRI images (Figure 3) following reperfusion. The phase of the OMRI image in Figure 3 provides sensitive contrast even in cases where the radical concentration is very low and the Overhauser enhancement may be small.

We have imaged TEMPOL at low concentrations with OMRI methods *in vitro*, and crossing the BBB following ischemia/reperfusion *in vivo*. The use of OMRI in conjunction with the stable free radical TEMPOL as an exogenously administered probe in hyperacute stroke is a new and novel approach, and this study suggests that TEMPOL may be a suitable probe for observing early BBB breakdown following reperfusion in rodent I/R models. Additionally, as TEMPOL reduction has been used as a functional probe to study redox status in tissue [6], we hypothesize that temporally resolved OMRI may be used to indicate the redox status of ischemic tissue.

References: (1) Pillai DR, *et al.* J Cereb Blood Flow Metab., 2009 Aug 5;29(11):1846–55 ; (2) Knight RA *et al* J Cereb Blood Flow Metab. 2009; 29(5):1048–58 ; (3) Sarraclanie M *et al.* MRM 2013 DOI: 10.1002/mrm.24705 ; (4) Behringer W *et al.* J Cereb Blood Flow Metab. 2002 22(1):105–17 ; (5) Tsai LL *et al.* JMR, 2008 93(2):274–85 ; (6) Hyodo F *et al.* J Pharm Pharmacol.2008 60(8):1049–60.

Acknowledgements: This work supported by the Department of Defense, Defense Medical Research and Development Program, Applied Research and Advanced Technology Development Award W81XWH-11-2-0076 (DM09094).

Spatial resolution in rotating Spatial Encoding Magnetic field MRI (rSEM-MRI)

Clarissa Zimmerman Cooley^{1,2}, Jason P. Stockmann^{1,3}, Brandon D. Armstrong^{1,3}, Mathieu Sarraoane^{1,3}, Matthew S. Rosen^{1,3}, and Lawrence L. Wald^{1,4}
¹A. A. Martinos Center for Biomedical Imaging, Dept. of Radiology, Massachusetts General Hospital, Charlestown, MA, United States, ²Dept. of Electrical Engineering and Computer Science, Massachusetts Institute of Technology, Cambridge, MA, United States, ³Dept. of Physics, Harvard University, Cambridge, MA, United States, ⁴Harvard-MIT Division of Health Sciences and Technology, Cambridge, MA, United States

TARGET AUDIENCE: MR system engineers and those requiring portable MRI systems.

PURPOSE: As the premiere modality for brain imaging, MRI could find wider applicability if lightweight, portable systems were available for siting in unconventional locations. However, realization of such lightweight, low power systems will require non-standard spatial encoding approaches such as rotating non-linear Spatial Encoding Magnetic fields (rSEMs). In this work we examine the spatial variations in image resolution of different SEMs for rotating scanners. We compare modeled spatial resolutions to acquired images encoded by a rotating SEM from a lightweight rotating Halbach magnet.

METHODS: A small rotating permanent magnet Halbach array with an inhomogeneous field has been used to create a portable 2D MRI scanner^{1,2}. The field distribution, which is predominately quadrupolar (~ 320 Hz/cm²), is used for image encoding instead of gradient coils. As the magnet is physically rotated around the object using a stepper motor, a RARE type spin echo sequence records the generalized projections onto the SEM. If sufficient multi-polar terms are present in the SEM, as is the case for the Halbach field, then parallel imaging is required to disambiguate the encoding³. We use a stationary 8 channel Rx array containing 8 cm overlapping loops whose sensitivity profiles vary with magnet rotation (as B_0 is rotated relative to the coils).

Data was acquired with the rotating Halbach scanner, and simulated for multiple rotating SEMs and simulation objects. These SEMs include the measured field of the Halbach magnet with and without an additional linear shim field (1.2mT/m), and a pure linear SEM with the same magnetic field range of the Halbach SEM (6 mT/m). In order to evaluate spatial resolution, a line of point sources spaced 5mm apart along the radius of the 16cm circular FOV were simulated. A 2D Gaussian low-pass filter was used to smooth the point sources to 0.5mm FWHM. In addition, images of single point sources were simulated to evaluate the varying FWHM of point spread functions (PSFs) along the radius.

Assuming a 20 KHz sampling BW, 256 point spin echoes were simulated for each coil and each magnet rotation (181 angles spaced 1° apart). The phase accumulation with time in each voxel is calculated using the magnetic field map, then multiplied by the complex coil sensitivity map and the magnitude of the simulated object, and summed to form the net signal.

Data is reconstructed using the encoding matrix which contains the phase information estimated from the encoding field, as well as the effect of the coil sensitivities. This general encoding model is solved iteratively using the Algebraic Reconstruction Technique^{2,4}.

RESULTS: 2D and 1D images of a line of Gaussian points simulated from 3 rotating SEMs are shown in Figure 1a-b. Figure 1c shows variation in FWHM of simulated point spread functions along the radius. A uniform Rx coil was assumed for Fig. 1 simulations (the aliased portion is cropped). Simulated brain images using the 8 channel receive array, and the Halbach SEM or Halbach+linear SEM are shown in Figure 2

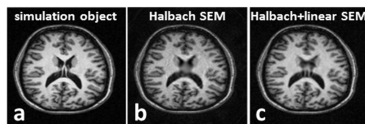


Figure 2: Simulations. (a) T1-weighted brain reference. (b) Simulated using Halbach SEM. (c) Simulated with Halbach SEM + linear field.

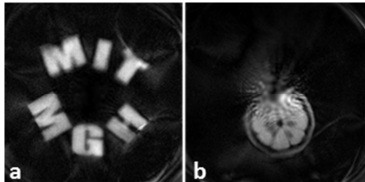


Figure 3: Experimental 16 cm FOV images. (a) 1.5cm thick phantom filled with CuSO4 doped water. (b) 1 cm thick lemon slice.

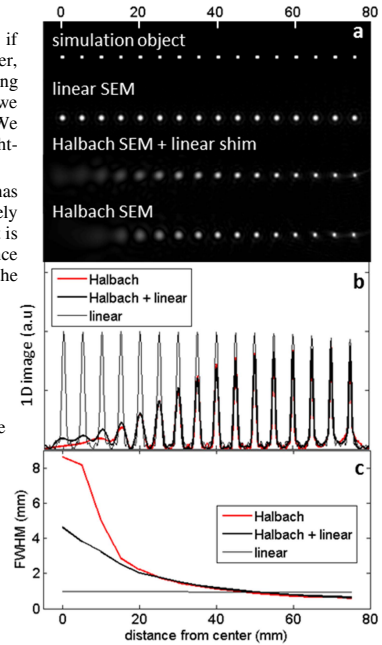


Figure 1: Simulated 2D (a) and 1D (b) images of a line of points starting at center of FOV using multiple rotating SEMs. (c) FWHM of the PSF along the radius. (x-axis common to fig. a,b, and c)

(noise levels matched to experimental data). Figure 3 shows experimental images using the Halbach SEM of a “MIT/MGH” phantom (CuSO₄-doped water, 1.7cm thick, 13cm dia.) acquired with 7 coils of the Rx array, 32 averages of a 6 spin echo train (TR = 550 ms, echo spacing = 8ms) and 91 2° magnet rotations. Figure 4b shows a 1cm thick lemon slice imaged with 5 coils, a 128 echo train (TR = 4500ms, echo spacing = 8ms), and 181 1° magnet rotations.

DISCUSSION & CONCLUSION: As expected, the resolution resulting from the rotating linear SEM is nearly uniform (Fig 1). Multi-polar SEMs have a steep gradient near the periphery and a shallow gradient near the center. This translates to the resulting resolution in images acquired with rSEMs with multi-polar components – higher resolution near the periphery and an “encoding hole” in the center (Fig 1, 2b, 3b). When a sufficient linear term is added to the SEM, the shallow encoding field region does not coincide with the axis of rotation. In this case, the “encoding hole” moves around the object resulting in less severe blurring (Fig 1, 2c). The simulations in Figure 2 show the theoretical resolution of the Halbach rSEM scanner when systematic errors are eliminated. These errors (effects seen in the experimental images, Fig. 3) likely result from field map or coil sensitivity profile inaccuracies propagating through the iterative reconstruction⁶.

REFERENCES: (1) Zimmerman C, ISMRM 2012. (2) Cooley CZ, ISMRM 2013. (3) Schultz G, MRM 2010. (4) Gordon R, Journal of theoretical biology 1970. (6) Stockmann JP, MRM 2013.

ACKNOWLEDGMENTS: The authors thank C Lapierre, M Christensen, E Siskind, B Guerin, and S Cauley. Support by DoD/USAMRRA W81XWH-11-2-0076 (DM09094) and NIH P41EB015896.

High Speed MR Fingerprinting at 6.5 mT

Mathieu Sarraclanie^{1,2}, Brandon D. Armstrong^{1,2} and Matthew S. Rosen^{1,2,3}

¹A. A. Martinos Center for Biomedical Imaging, 149 13th St., Suite 2301, Boston, MA. 02129, ²Department of Physics, Harvard University, 17 Oxford St. Cambridge, MA. 02138, ³Harvard Medical School, 25 Shattuck St, Boston, MA. 02115

High-field MRI instruments offer limited utility in field deployable and portable contexts. Our effort focuses on the critical challenges that must be solved to enable deployment of transportable MRI systems. In recent work [1], we demonstrated high performance MRI at low magnetic field by making use of high-efficiency steady state free precession techniques (b-SSFP) [2] and undersampling for compressed sensing MRI. Earlier in 2013, a new imaging technique termed "magnetic resonance fingerprinting" (MRF) was proposed [3]. Unlike all other MRI sequence strategies, MR Fingerprinting allows the simultaneous quantification of multiple properties of a material or tissue in a single acquisition. In the present work, we show the first implementation of MR Fingerprinting at very low magnetic field in a multi-compartment phantom.

MRF at low magnetic field creates a rapid dynamic series of low signal to noise ratio (SNR) images where the magnitude of each voxel of each image changes at every time step. The TR and flip angle of each image in the time series is varied pseudo-randomly [5]. No steady state is reached, and image voxels with different relaxation times evolve differently, thereby generating unique magnetization trajectories. The time evolution of each voxel is simulated offline using the Bloch equations with the TR and flip angle patterns used for the imaging sequence over a wide range of tissue parameters, and a database (dictionary) of trajectories is generated. The measured voxel trajectory is compared to the dictionary and the best match is chosen, identically providing the T_1 , T_2 , and off-resonance frequency value of that voxel. Lack of SNR at low magnetic field required redesigning our sequence to lower undersampling rates and bigger flip angle range. The resulting sequence is a 200 time points, 50% undersampled, slice-selective 20 spirals sequence. After an inversion pulse, flip angle ranges between 30 and 107°, TR varies between 46.1 ms and 52.7 ms. The dictionary was made of 2,751,975 signal time courses, each with 200 time points. MR total acquisition time was 13 min. The sequence was set with voxel size: $3 \times 3 \times 10 \text{ mm}^3$, FOV: $144 \times 144 \times 10 \text{ mm}^3$, number of average (NA): 6. The low field MRI scanner was previously described [6].

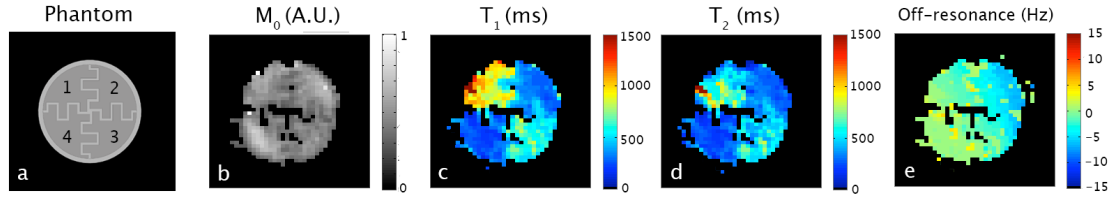


Figure 1: Slice selective MRF results obtained at 6.5 mT. The four-compartment liquid filled structured phantom shown schematically in (a). The compartments vary in relaxation properties. Each compartment had T_1 and T_2 measured in separate reference experiments (Inversion recovery & T2 CPMG respectively). 1: $T_1=1046 \text{ ms}$, $T_2=700 \text{ ms}$, 2: $T_1=425 \text{ ms}$, $T_2=418 \text{ ms}$, 3: $T_1=600 \text{ ms}$, $T_2=591 \text{ ms}$, 4: $T_1=340 \text{ ms}$, $T_2=286 \text{ ms}$. **b-e** show M_0 , T_1 , T_2 , and off-resonance frequency, respectively.

Each image generated in the reconstructed fingerprinting set (Figure 1 b–e) reveals different information. The spin density (M_0) map of Figure 1.a is equivalent to traditional b-SSFP, and no visible difference between compartments is seen. However, Figure 1. c–d reveals that compartments 1–4 have very different T_1 and T_2 relaxation properties. The MRF images show good agreement with the reference measurements. Additionally, a map of the magnetic field homogeneity of the LFI scanner is also generated during the MRF sequence (Figure 1.e).

We have demonstrated MR Fingerprinting at low magnetic field, which results in simultaneous measurement of 4 quantitative parameters, and thus provides 4 different image contrasts in a single acquisition (proton density, T_1 , T_2 and off-resonance) in less than 15 minutes. This technique is of particular relevance at low magnetic field where SNR and contrast are tied to long acquisition times. The combination of MRF with low field MRI scanners has great potential to revolutionize future transportable MRI systems.

References: [1] Sarraclanie M *et al.* ISMRM 2013 #5322; [2] Scheffler K *et al.* Eur Radiol 2003 13:2409-18; [3] Ma D *et al.* Nature 2013 495:187-193; [4] Perlin K *et al.* Comput Graphics 1985 19:287-296; [6] Tsai LL *et al.* JMR 2008; 193:174-85.

Acknowledgement: This research was supported by the Department of Defense, Defense Medical Research and Development Program, Applied Research and Advanced Technology Development Award W81XWH-11-2-0076 (DM09094).

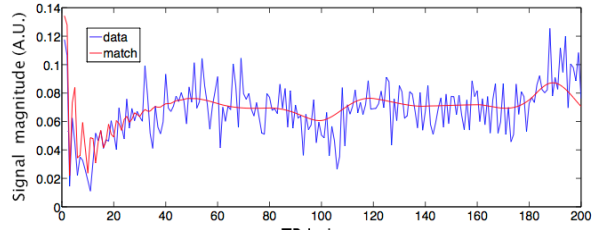


Figure 2: The magnetization trajectory of a single typical voxel over the 200 image fingerprinting sequence is shown (blue: data, red: best match from dictionary). All the parameters of the voxel (M_0 , T_1 , T_2 , and off-resonance frequency) are determined once the trajectory match is

High Speed 3D Overhauser-Enhanced MRI Using Combined b-SSFP and Compressed Sensing

Mathieu Sarraclanie,^{1,2} Brandon D. Armstrong,^{1,2} Jason Stockmann,^{1,2} and Matthew S. Rosen^{1,2,3*}

Purpose: Overhauser-enhanced MRI is a promising technique for imaging the distribution and dynamics of free radicals. A key challenge for Overhauser-enhanced MRI is attaining high spatial and temporal resolution while simultaneously limiting resonator and sample heating due to the long, high power radio-frequency pulses needed to saturate the electron resonance.

Methods: The approach presented here embeds EPR pulses within a balanced steady state free precession sequence. Unlike other Overhauser-enhanced MRI methods, no separate Overhauser prepolarization step is required. This steady-state approach also eliminates the problem of time-varying Overhauser-enhanced signal and provides constant polarization in the sample during the acquisition. A further increase in temporal resolution was achieved by incorporating undersampled k-space strategies and compressed sensing reconstruction.

Results: We demonstrate $1 \times 2 \times 3.5 \text{ mm}^3$ resolution at 6.5 mT across a $54 \times 54 \times 110 \text{ mm}^3$ sample in 33 s while sampling 30% of k-space.

Conclusion: The work presented here overcomes the main limitations of Overhauser enhanced MRI as previously described in the literature, drastically improving speed and resolution, and enabling new opportunities for the measurement of free radicals in living organisms, and for the study of dynamic processes such as metabolism and flow. *Magn Reson Med* 71:735–745, 2014. © 2013 Wiley Periodicals, Inc.

Key words: 3D Overhauser MRI; free radicals; EPR; b-SSFP; compressed sensing

Imaging of free radicals has been used to investigate a number of important physiological processes such as the mapping of pO_2 (1–3), free radical distribution and metabolism (4–7), molecular imaging (8), and to monitor changes in local viscosity (9,10). Magnetic resonance

imaging (MRI) is a powerful and noninvasive tool that provides excellent anatomical detail. However, MRI is sensitive to nuclear spins (typically ^1H of water) and cannot alone reveal spatial information about the distribution of free radical species. EPR imaging (11–17) reveals the spatial distribution of unpaired electron spins, but requires a separate reference MRI to determine where the free radicals are located within the sample. While EPR imaging is a sensitive technique, images have poor resolution due to broad EPR lines, and are usually time-inefficient due to the usual CW acquisition strategy. Overhauser-enhanced MRI (18–23; OMRI, also known as proton-electron double resonance imaging) exploits the dipolar coupling between the unpaired electron of the free radical and the ^1H nuclei of water to increase nuclear magnetization via dynamic nuclear polarization (DNP) and subsequently images the enhanced nuclear spin polarization with MRI. OMRI provides an excellent way to image free radical species as narrow NMR line widths enable imaging using reasonable-strength encoding gradients. OMRI also benefits from the ability to use traditional MRI sequences, though specialized hardware is needed to drive the electron spin resonance, and the sequences must be modified to allow for EPR saturation pulses.

A difficulty of OMRI is the need for high power radio-frequency (RF) to saturate the electron spins. Additionally, as EPR frequencies are two orders of magnitude higher than ^1H frequencies, a high frequency resonator is required, and this leads to high specific absorption rate (SAR) and limited penetration depth. For these reasons, OMRI is usually performed at a low- to intermediate magnetic field (5,22,24) or in a field-cycled setup (4,25). A typical field-cycled OMRI experiment begins at very low magnetic field ($\sim 5 \text{ mT}$) where EPR irradiation is applied for approximately the nuclear T_1 of the sample at the irradiation magnetic field. The magnetic field is then quickly ramped up to the imaging field and a line or plane of k-space data is acquired. The magnetic field is then ramped down for EPR irradiation and repolarization because the DNP signal decays with the ^1H nuclear T_1 . Field-cycled OMRI helps to overcome both the hardware and penetration depth challenges by reducing the EPR frequency, but these experiments are much slower and more complex than traditional MRI due to the need to refresh the DNP-enhanced signal many times over the acquisition time.

We present here a new method for 3D OMRI based on b-SSFP at a constant field of 6.5 mT that provides up to 7-fold acceleration compared to the fastest OMRI sequence reported in the literature (24). We further

¹Department of Physics, Harvard University, Cambridge, Massachusetts, USA.

²Department of Radiology, A.A. Martinos Center for Biomedical Imaging, Massachusetts General Hospital, Boston, Massachusetts, USA.

³Department of Radiology, Harvard Medical School, Boston, Massachusetts, USA.

Grant sponsor: Department of Defense, Defense Medical Research and Development Program, Applied Research and Advanced Technology Development Award; Grant number: W81XWH-11-2-0076 (DM09094).

*Correspondence to: Matthew S. Rosen, Ph.D., Low Field MRI and Hyperpolarized Media Laboratory, A. A. Martinos Center for Biomedical Imaging, 149 13th Street, Suite 2301, Charlestown, MA 02129, USA.

E-mail: mrosen@cfa.harvard.edu

Received 30 October 2012; revised 11 January 2013; accepted 7 February 2013.

DOI 10.1002/mrm.24705

Published online 8 March 2013 in Wiley Online Library (wileyonlinelibrary.com).

© 2013 Wiley Periodicals, Inc.

maintain the high acquisition efficiency of b-SSFP by applying the Overhauser saturation pulses during the phase encode step, eliminating the time-consuming pre-irradiation step done in all previously reported OMRI. Additionally, we add undersampling strategies and compressed sensing (CS) techniques to increase the temporal resolution while also reducing the total number of EPR RF pulses. We obtain $1 \times 2 \times 3.5 \text{ mm}^3$ resolution on a $54 \times 54 \times 110 \text{ mm}^3$ sample in 33 s. We show that a steady-state signal is still achieved with this new OMRI b-SSFP sequence, and that simulations with no free parameters agree very well with the experimental results.

METHODS

OMRI Setup

A custom built, low-field MRI scanner with a biplanar 6.5 mT electromagnet (B_0) and biplanar gradients was used for all experiments and was previously described (26) (Fig. 1a). The system was upgraded and optimized for ^1H imaging for this work resulting in improved B_0 stability, higher gradient slew rates, and lower overall noise. This effort included the use of an improved power supply (System 854T, Danfysik, Taastrup, Denmark) for the electromagnet with ± 1 ppm stability over 20 min and ± 2 ppm stability over 8 h, and the addition of high-current shielded cables throughout the system. The

scanner operates inside a double-screened enclosure (ETS-Lindgren, St. Louis, MO) with a RF noise attenuation factor of 100 dB from 100 kHz to 1 GHz.

The transfer of electron spin polarization to dipolar or scalar coupled nuclear spins via the Overhauser effect requires high power irradiation of the electron spin resonance (27,28). A 7 cm OD, 13 cm long Alderman-Grant coil (29,30; Fig. 1b) with guard rings to reduce sample heating was used to saturate the electron spin resonance of the nitroxide radical 4-hydroxy TEMPO (Sigma-Aldrich, St. Louis, MO). The electron spin resonance is split into three transitions by the hyperfine coupling of the spin 1 ^{14}N nucleus (at 6.5 mT, there still exist other transitions described by the Breit-Rabi equations but their transition probabilities are small and ignored here; 31). As SAR scales with ω^2 (32–36) the EPR coil was tuned to the low energy transition of 140.8 MHz to minimize SAR. The EPR coil was placed inside a 10 cm OD, 16 cm long solenoid coil used for NMR excitation and detection at 276 kHz (Fig. 1c). The coils were oriented such that their B_1 fields were perpendicular to each other and to B_0 . Placing the NMR coil outside the ESR coil sacrifices NMR filling factor to gain larger B_1 for electron spin saturation as our DNP signal enhancement (defined as $\langle I_z \rangle / I_0$ where I_0 is the thermal equilibrium NMR signal and $\langle I_z \rangle$ is the DNP signal) is limited by the available RF power.

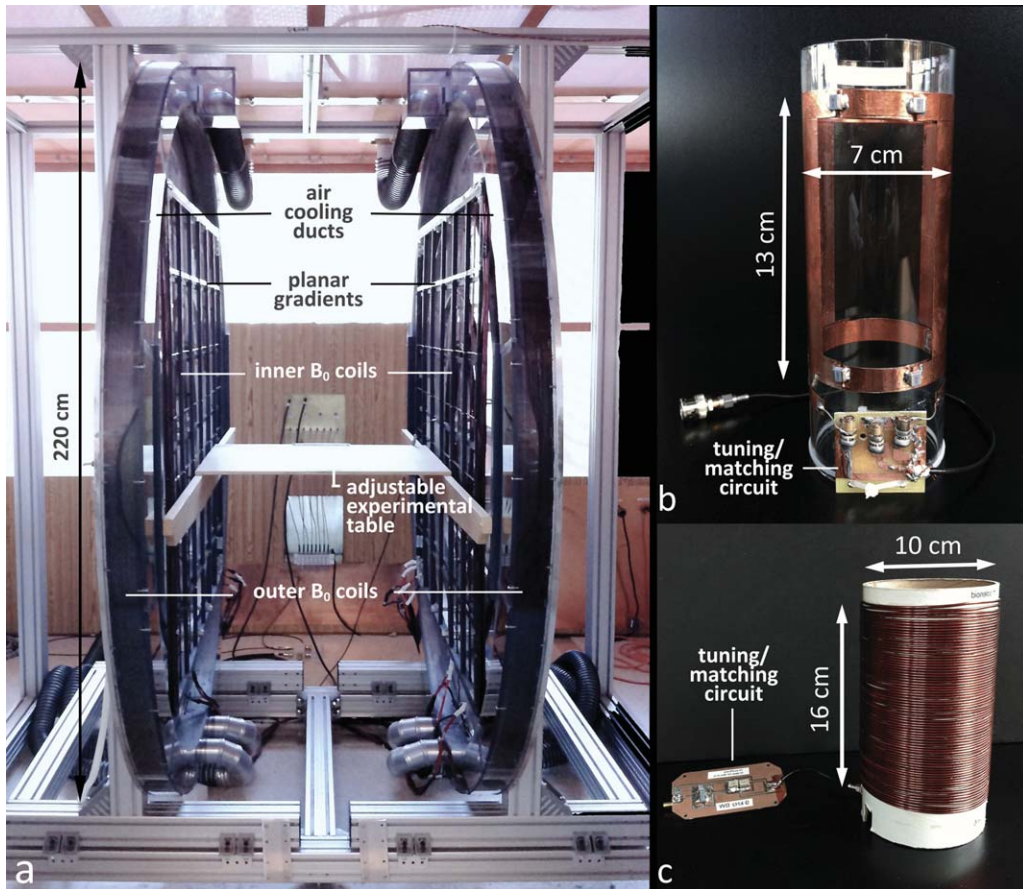


FIG. 1. OMRI setup. Photographs of (a) the custom built 6.5 mT MR scanner with bi-planar electromagnet and gradient set inside the shielded room, (b) the EPR (141 MHz), and (c) NMR (276 kHz) coils used for the OMRI experiments.

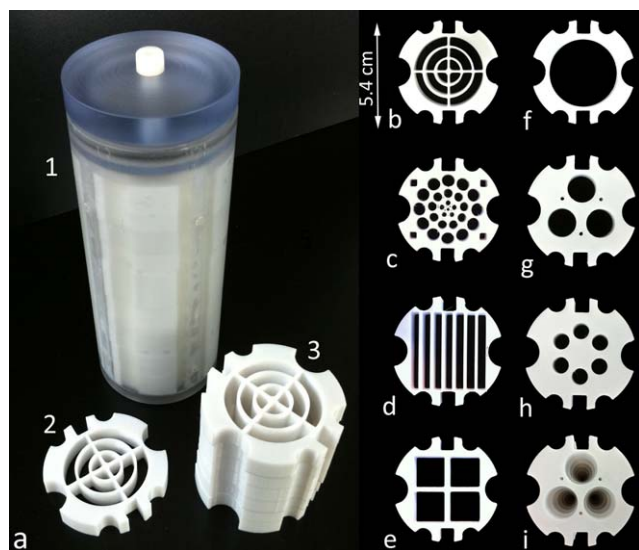


FIG. 2. Photograph of (a1) the assembled OMRI phantom, (a2) a 10 mm thick internal piece, and (a3) a stack of internal pieces. Shown in (b-h) are individual pieces of the phantom in configuration 1 (f-h) and configuration 2 (b-e). A top view of the stacked pieces for the phantom in configuration 1 as described in the text is shown in (i). [Color figure can be viewed in the online issue, which is available at wileyonlinelibrary.com.]

A Redstone NMR console (Tecmag, Houston, TX) was used for data acquisition and controlled the gradients and RF channels. The console has two transmit channels allowing for both NMR and EPR irradiation. A 100 W, CW amplifier (BT00100-DeltaB-CW) was used for EPR saturation and a 500 W pulsed amplifier (BT00500-AlphaS) was used for NMR (from both Tomco Technologies, Stepney, Australia).

Phantom Design

A configurable imaging phantom was built for these experiments. Various pieces designed to demonstrate resolution in three dimensions and test the ability to resolve sharp edges in under-sampled k-space were 3D printed in polycarbonate on a Fortus 360 mc (StrataSys, Eden Prairie, MN). The 3D printed pieces were stacked inside a 5.5 cm ID, 13 cm long machined polycarbonate cylinder. The advantage of this phantom is the flexibility to design and 3D print any desired structure for a particular experiment. The cylinder was then filled with 250 mL of 2.5 mM 4-hydroxy TEMPO solution in water, and a leak-tight polycarbonate cap inserted. The assembled phantom and individual pieces are shown in Figure 2. Imaging experiments were performed in two different phantom stacking configurations. The first stacked geometry consists of two interlocking sets of a trio of step-wise-smooth cones and was used to evaluate the 3D character of the sequence and the minimum structure sizes that can be resolved for round-shaped objects (Fig. 2f-i). The second configuration used more complex structures with finer details to assess the sequence performance, ability to resolve small in-plane structures, and the results of undersampling on sharp edges (Fig. 2b-e). Fiber optic temperature probes (Luxtron,

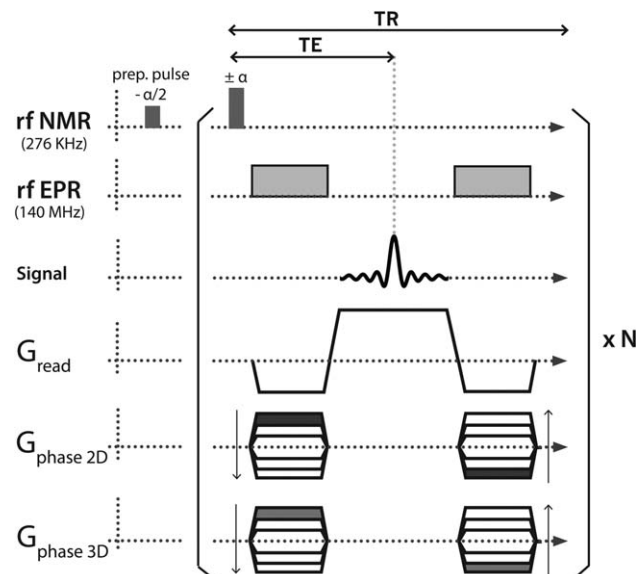


FIG. 3. Diagram of the 3D b-SSFP sequence with embedded EPR pulses (rf EPR). N is the total number of TRs in the sequence.

LumaSense Technologies, Santa Clara, CA) were placed inside the phantom and near a ring capacitor on the EPR coil during tests of the imaging sequence to monitor sample and coil temperatures.

3D Balanced SSFP with DNP

The pulse sequence used is shown in Figure 3. It is important to note that there is no separate EPR saturation step unlike all OMRI sequences reported in the literature. The sequence is a b-SSFP sequence with the addition of EPR (Overhauser) irradiation during the balanced phase encode gradients. The b-SSFP excitation train consists of an initial $-\alpha/2$ preparation pulse immediately followed by a train of alternating $\pm\alpha$ excitation pulses as previously described by Sheffler and Lehnardt (37). The $\pm\alpha$ pulses are separated by TR and the time interval between the $-\alpha/2$ preparation pulse and the first α pulse was set to 2 μ s. The main benefit of using a preparation pulse is that it prevents large fluctuations of the pre-steady state signal that would produce image artifacts and thus could not be used for signal acquisition (37). In b-SSFP, the optimal flip angle α is given by $\cos(\alpha) = \frac{T_1/T_2 - 1}{T_1/T_2 + 1}$ (37). T_1 and T_2 in our phantom were measured to be 545 ms and 488 ms, respectively, which leads to an optimal flip angle of $\alpha \sim 90^\circ$.

Bloch simulations were performed for a sequence without phase gradients (i.e., at the center of k-space), both with- and without EPR irradiation to model the buildup and time course of transverse magnetization as well as the signal enhancement provided by DNP. The simulations were run in MATLAB (MathWorks, Natick, MA) using code written in-house. Input parameters to the simulations were the measured T_1 and T_2 relaxation times, the measured enhancement provided by DNP with a 1.5 s EPR pulse ($\sim 3 \times {}^1\text{H } T_1$) in a 1D spectroscopy experiment (-44.5 fold enhancement), $\text{TR}/\text{TE} = 54/27$ ms and $\alpha = 90^\circ$. This negative enhancement results from

Overhauser DNP pumping into the opposite spin nuclear ground state compared with the Boltzmann case. This sign is important for the simulations. OMRI experiments with these parameters, a total bandwidth $BW = 9091$ Hz, and a 71 Hz bandwidth per pixel, were run and compared with the simulations.

The 3D imaging experiment was performed initially with full Cartesian acquisition of k-space. The sequence was set with $TR/TE = 54/27$ ms, a $256 \times 64 \times 112$ mm³ field of view, and acquisition matrix of $128 \times 64 \times 32$, resulting in a $2 \times 1 \times 3.5$ mm³ voxel size. The balanced phase gradient durations were both set to 20 ms to reach the desired in-plane spatial resolution when the gradient amplifiers were at maximum power. The readout duration was 14 ms with 9091 Hz bandwidth and total acquisition time was 114 s for fully sampled k-space. Critical to the success of these experiments is a very stable magnetic field as off-resonance effects can distort the image and cause severe banding artifacts (37).

It should be noted that the application of EPR saturation pulses while the gradients are on is only possible because our maximum gradient strength is low, 0.1 gauss cm⁻¹, giving a spread in electron resonance frequencies across the 5.5 cm sample (in-plane dimension) of ~ 1.54 MHz. The loaded Q of the EPR coil was determined using a vector network analyzer and an untuned pick up coil to measure the transmission response of the EPR coil (S21). The measured Q of 62 corresponds to a bandwidth of ~ 2.3 MHz, thus the spread in electron spin frequencies during the phase encode step is well covered.

Compressed Sensing

Most images are sparse in the sense that they can be accurately represented with fewer coefficients than one would assume given their spectral bandwidth (38). CS is a framework for exploiting sparsity to reconstruct high-fidelity MR images from undersampled k-space datasets that do not fulfill the Nyquist sampling theorem. In CS image reconstruction, image sparsity is enforced by truncating the small coefficients of an object's representation in a sparse basis, typically chosen to be a wavelet transform domain. During image reconstruction, the data are transformed from k-space (the sensing basis) into the wavelet basis via a sparsifying transform, ψ , taken for this work to be the Dirichlet wavelet transform.

CS uses norms to modify the objective function that is optimized during image reconstruction. To understand the role of norms in the objective function, it is helpful to recall standard Fourier reconstruction. For a discrete image m , Fourier operator F , and k-space dataset y , the L_2 -norm, $\|Fm - y\|_2 = (\sum_i |(Fm)_i - y_i|^2)^{1/2}$, is implicitly used to find an image whose Fourier transform differs as little as possible from the k-space data in the Euclidean sense. For fully sampled data, the least squares solution is provided by the Fourier transform. In the case of underdetermined matrix problems (as when the k-space data is undersampled), the L_2 -norm may be additionally used to constrain image reconstruction so as to reduce the noise (an approach known as Tikhonov regularization). However, when the L_2 -norm is used in this way, it functions as a low-pass filter, penalizing noise at the

expense of introducing bias. It does not promote image sparsity. By contrast, the L_1 -norm, defined as $\|x\|_1 = \sum_i |x_i|$ for an arbitrary function x , has a tendency to preserve edges and large coefficients, e.g., for neighboring voxels $\{0,3,0\}$ the L_2 -norm will tend to penalize the difference toward $\{1,1,1\}$, while the L_1 -norm of both cases is the same, preserving the edge.

The ability of the L_1 -norm to preserve large coefficients makes it an appealing choice for enforcing sparsity in images (39,40). In the CS framework, the L_1 -norm is applied to the wavelet transform of the image, where it naturally selects the large coefficients representing image features while reducing the small coefficients corresponding to noise and incoherent artifacts. For additional denoising and artifact suppression, a finite difference norm (a discrete implementation of the Total Variation, or TV , norm) is applied in the image domain (41). This norm has been shown to preserve object edges while eliminating noise.

As shown in (42), the resulting image reconstruction problem is expressed as a balance between the L_1 -norm constraints and the L_2 -norm data consistency constraint:

$$\min [\|F_u m - y\|_2 + \alpha \|\psi m\|_1 + \beta TV(m)]$$

where F_u is the undersampled Fourier transform operator, y is the undersampled k-space data, and coefficients α and β weight the relative contributions of each norm to the final image. A variety of algorithms are available for minimizing this nonlinear objective function (42). Specific details about our implementation of CS for OMRI b-SSFP are given below.

Undersampled OMRI b-SSFP

The use of CS in MRI relies on the possibility to acquire a priori compressed information and be able to reconstruct the original image as if the latter was fully sampled (42). In the context of data acquisition, this motivates the use of undersampling. CS has been found to work best when k-space is randomly undersampled to produce incoherent artifacts rather than the familiar wrap-around ghosts due to field-of-view contraction when k-space lines are skipped in a regular coherent pattern as is done in conventional parallel imaging (43). For the images presented here, a choice was made to acquire random lines of k-space in the phase-encode directions (k_y, k_z) following a gaussian probability density function. The readout direction was fully sampled. The standard deviations of the sampling pattern as a fraction of the field-of-view along y and z , σ_y , and σ_z , respectively, were adjusted manually to preserve adequate high-frequency information for each undersampling rate. We investigated four undersampling fractions, 50, 70, 80, and 90%. The undersampling patterns are shown in Figure 4. On the acquisition side, this resulted in programming different phase encode tables for each undersampled sequence. The total acquisition time for each undersampling rate is shown in Table 1. To perform image reconstruction according to the L_1 -norm and the data consistency constraints, the Sparse MRI code (<http://www.eecs.berkeley.edu/~mlustig/Software.html>) was used. This code solves the optimization problem using a

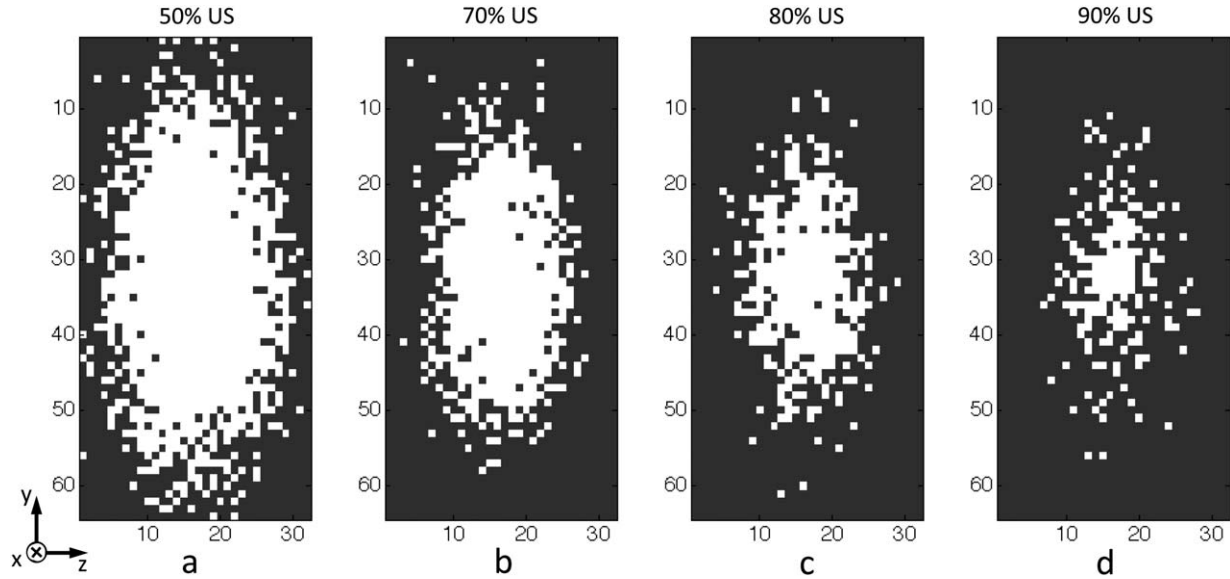


FIG. 4. Undersampling (US) patterns used for (a) 50% undersampling, (b) 70% undersampling, (c) 80% undersampling, and (d) 90% undersampling. For an undersampling rate of 50%, 995 of 2048 lines were acquired. For 70% undersampling, 585 of 2048 lines were acquired. For 80% and 90% undersampling, 383 and 185 of 2048 lines were acquired, respectively.

nonlinear conjugate gradient method along with backtracking line-search as described in (42). The parameters for the wavelet and image domain norms were tuned manually to produce low-noise images with preserved object features. The missing values in the acquired k-space data were made identically zero. To separate out the data into slices, a Fourier transform was performed along the readout direction (*x*). Each sagittal slice of k-space data (*y*–*z* plane) was then reconstructed by the Sparse MRI algorithm. After all slices were reconstructed, the resulting 3D block of image domain data was then displayed as transverse (*x*–*y*) slices. The computation time for a laptop equipped with a 2.3 GHz quad-core processor was 4.5 min, permitting CS image reconstruction immediately following k-space acquisition.

Table 1

Comparison of Acquisition Time, Maximum SNR, and Mean Absolute Error (MAE) as a Function of the Undersampling Fraction for the Two Different Phantom Configurations with the Maximum Applied RF Power of 62 W at the EPR Coil

	Acq. time (s)	Maximum SNR		MAE
		No CS	CS	
<i>Configuration 1</i>				
Fully sampled	114	23	40.6	
50% Undersampling	56	35.8	75.8	0.073 ± 0.006
70% Undersampling	33	44.6	95	0.072 ± 0.008
80% Undersampling	21	64.3	160	0.112 ± 0.011
90% Undersampling	10	69.8	148	0.149 ± 0.014
<i>Configuration 2</i>				
Fully sampled	114	24.6	42.6	
50% Undersampling	56	30.47	49.7	0.049 ± 0.005
70% Undersampling	33	42	78.3	0.059 ± 0.010
80% Undersampling	21	49.9	94.7	0.100 ± 0.013
90% Undersampling	10	58.1	88.3	0.114 ± 0.014

RESULTS

Steady-State Signal with Embedded EPR Pulses

To understand the approach of transverse magnetization to steady state with embedded EPR pulses in the sequence, Bloch simulations were performed without the phase encode gradients and compared with acquired data. The results are shown in Figure 5. The data was normalized such that the maximum measured signal and the maximum simulated signal were both set to 1. The experimental data with DNP (\square) begins at thermal equilibrium, but rapidly builds up to 30 times that of the non-DNP data (\circ). This build up corresponds to the T_1 relaxation time of the sample (545 ms). The signal reaches $\sim 90\%$ of its steady state value after 24 echoes, or 1.3 s, and the simulation is in good agreement with the data (dashed line; not a fit).

Fully Sampled Versus Undersampled

Images of the two different phantom configurations are shown in Figures 6 and 7 after CS reconstruction. Images reconstructed from fully sampled k-space and from 50, 70, 80, and 90% undersampling are shown. Figure 6a,b shows the top and center structures of the interlocking cones (configuration 1). Figure 6c displays 3D rendered images of the segmented cones for each undersampling fraction. Figure 7a–e shows the different segments of the phantom in configuration 2. For both phantom configurations, 50 and 70% undersampling reproduces the fully sampled images well. Even small structures such as 2 mm diameter holes (Fig. 6a), 1 and 1.5 mm solid separators and 2.5 mm holes (marked by white arrows in Fig. 7b–d) are well resolved at 70% undersampling. For 80 and 90% undersampling, most of the structures are still visible although substantial blurring and ghosting artifacts begin to appear. Figure 7a,e correspond to the top and bottom slice of the phantom and show lower signal

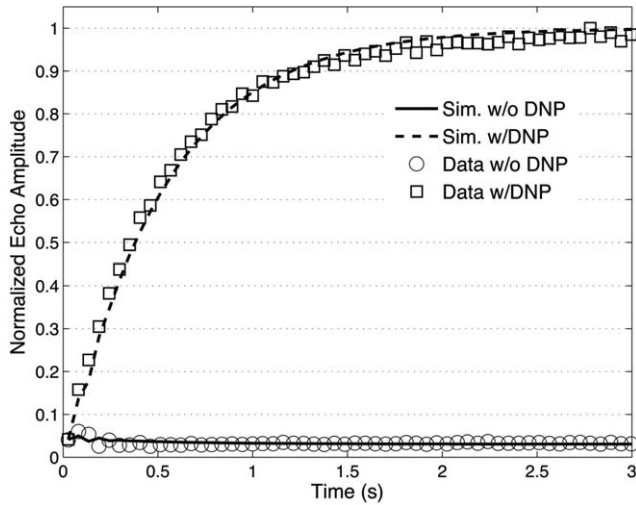


FIG. 5. Simulation and measurement of the approach to steady-state with- and without DNP. Plotted are the echo amplitudes acquired during the pulse sequence in Figure 3 with only the read gradient active. The DNP signal is nearly 30 times larger than the signal without DNP after reaching steady-state. Solid curves plotted are not a fit to the data but an exact simulation with no free parameters as described in the text.

magnitude due to the B_1 profile of the EPR coil. The maximum SNR was calculated from maximal signal amplitudes divided by two times the standard deviation of a user defined noise region before and after CS reconstruction and is shown in Table 1. The increase in SNR with undersampling rate is due to the undersampling

pattern acting as an apodization filter that removes high spatial frequencies from k-space. However, all images show an increase in SNR after CS reconstruction. The SNR enhancement using CS increases with the initial SNR of the image and ranges from about 1.5 to 2.5.

To quantify the errors that occur in the undersampled images, the mean absolute error (MAE) was calculated for each image (Table 1). The MAE was calculated by first thresholding the images such that only points that were five times greater than the noise (σ_n) were kept. The undersampled image was then subtracted from the fully sampled image and all non-zero values counted as an error. As seen in Table 1, the MAEs for the 50 and 70% undersampling rates are small and comparable while those for 80 and 90% increase significantly. The MAE for each of the 32 phase encode gradients along z for configuration 1 is shown in Figure 8 for all undersampling rates. There is little difference across the entire sample between 50 and 70%, again showing that the image is well reproduced with only 30% of the k-space data. Losses in SNR due to the B_1 profile of the EPR coil on slices 1–5 and 25–32 result in increased MAE values for all undersampling rates.

SAR Considerations

A problem limiting the use of OMRI is that the high power RF pulses necessary for DNP lead to high SAR. Two methods were used to estimate SAR. A fiber optic temperature probe was placed inside the sample and the fully sampled k-space sequence was run several times, waiting several minutes in between runs to allow the

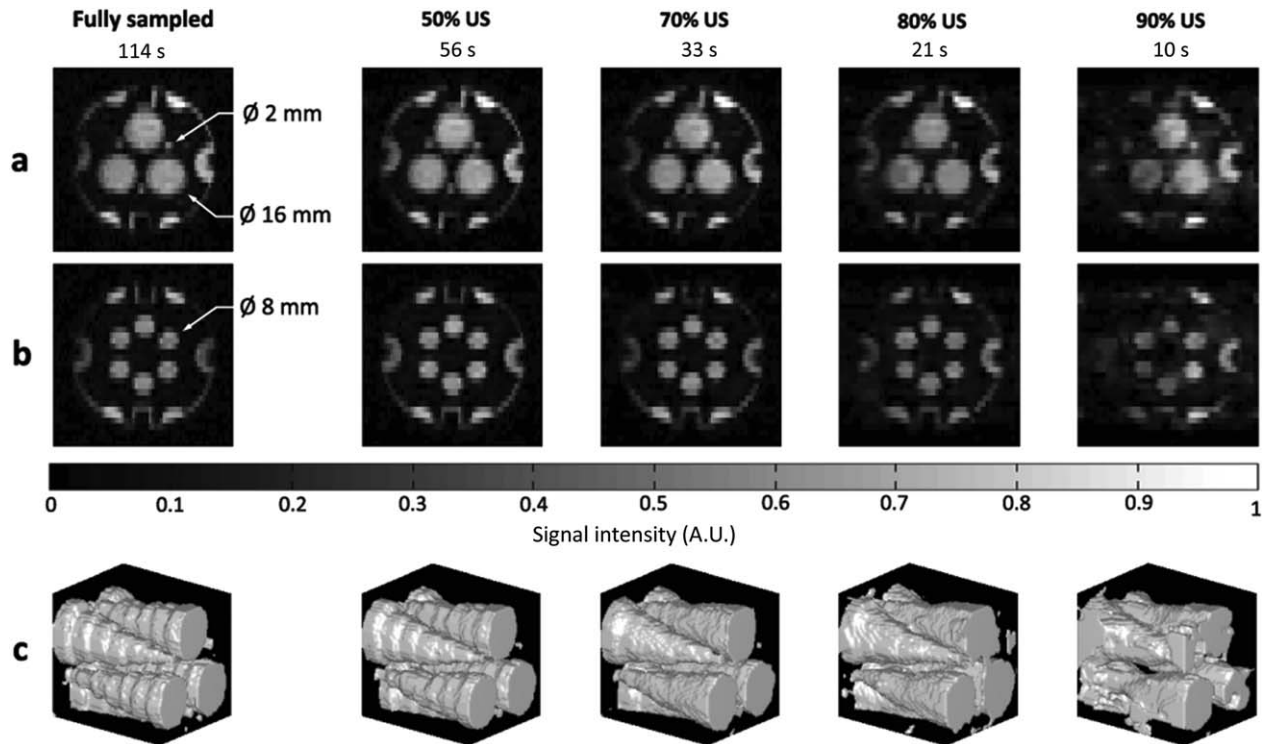


FIG. 6. Fully and undersampled (US) images of the phantom in configuration 1 after CS reconstruction as a function of undersampling fraction. a: Representative slices: Top (a) and center (b) of the full 32 slice dataset. Acquisition matrix: $128 \times 64 \times 32$, voxel size: $2 \times 1 \times 3.5 \text{ mm}^3$. c: 3D rendered images of the interlocked cone structure obtained from the fully and undersampled datasets.

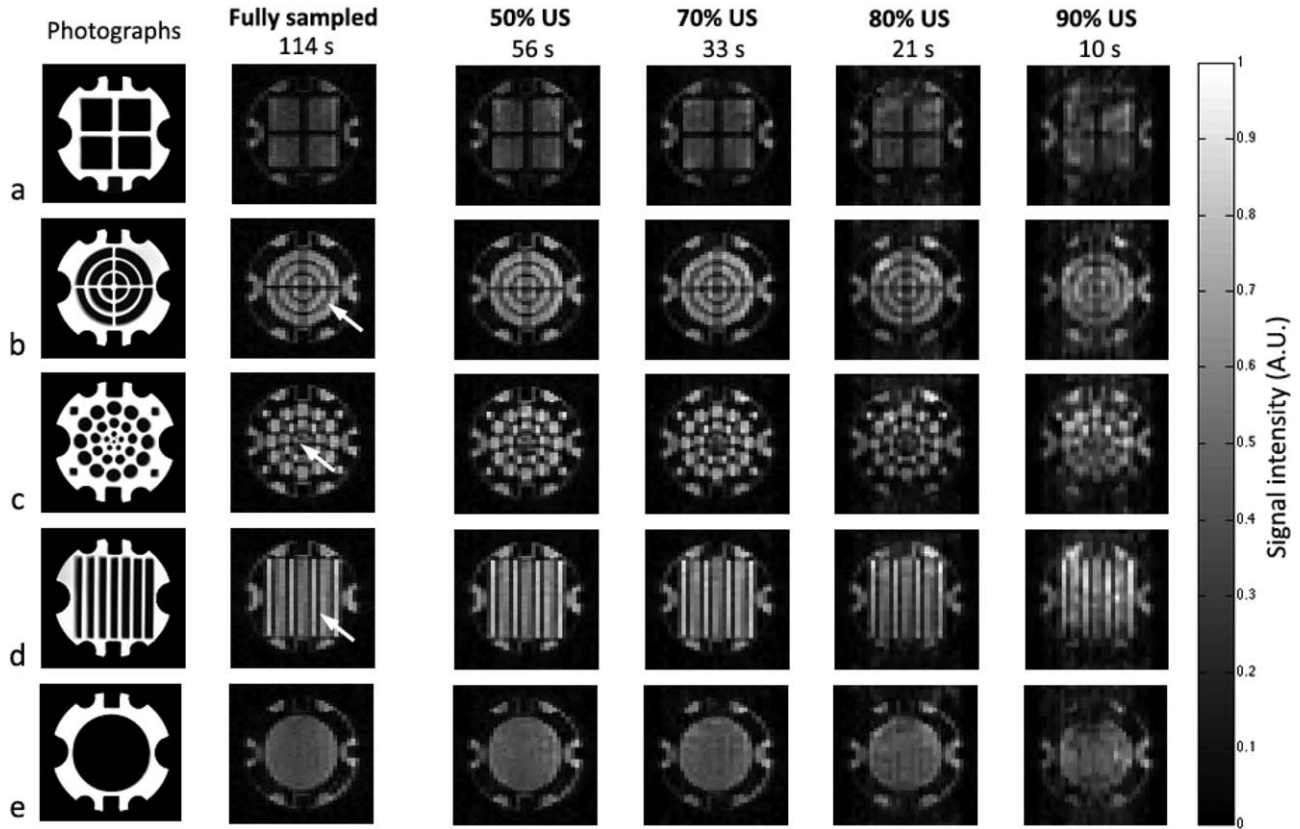


FIG. 7. Fully and undersampled (US) images of five representative slices after CS reconstruction. The full 32-slice data set was acquired with the phantom in configuration 2 as described in the text. MR images are shown alongside photographs of the corresponding phantom piece. Acquisition matrix: $128 \times 64 \times 32$, voxel size: $2 \times 1 \times 3.5 \text{ mm}^3$. White arrows indicate 1 and 1.5 mm solid separators, (b) and (d), respectively, and 2.5 mm diameter structures (c).

EPR coil to cool. The maximum measured temperature increase was 0.4°C . No temperature increase was measured for any of the undersampled sequences. Estimating

$\text{SAR} \sim cT/\Delta t$ (44) where c is the specific heat, ΔT is the temperature change and Δt is the time of the sequence gives $\text{SAR} = 15 \text{ W kg}^{-1}$. We expect this to represent a lower limit as heat may have dissipated during the sequence. As a second method, the power dissipated in the sample was estimated using (45):

$$P_{\text{sample}} = P_{\text{coil}}(1 - Q_{\text{loaded}}/Q_{\text{unloaded}})$$

The forward power was measured using a directional coupler (Model 3020A, Narda Microwave, Hauppauge, NY) and power meter (V3500A, Agilent Technologies, Santa Clara, CA), and the maximum forward power to the coil was $\sim 62 \text{ W}$. The loaded Q was measured to be 52 while the unloaded Q was 62. Thus the power to the sample during an EPR pulse is $\sim 10 \text{ W}$. The EPR irradiation is on for 73% of TR and the sample mass is 0.25 kg , therefore $\text{SAR} = 29 \text{ W kg}^{-1}$.

The 50% undersampled images in Figures 6 and 7 have high SNR and accurately represent the phantom. Therefore, we reduced the forward power to the coil by factors of 2, 4, 8, and 16 to investigate how much the SAR could be reduced (thusly reducing the Overhauser enhancement) while maintaining high image quality. The results are shown in Figure 9 and Table 2. Image quality is well maintained for 31 and 15.5 W forward power corresponding to an estimated SAR of ~ 14.5 and 7.25 W kg^{-1} , respectively.

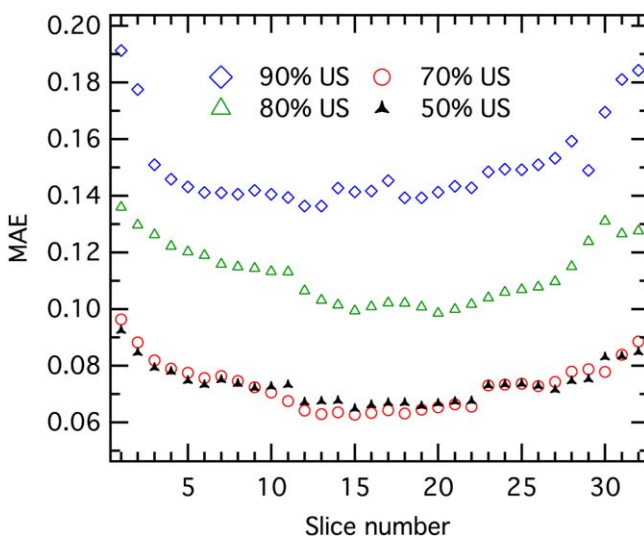


FIG. 8. MAE computed each slice number for each undersampling fraction with the phantom in configuration 1: 50% US (black), 70% US (red), 80% US (green), and 90% US (blue). [Color figure can be viewed in the online issue, which is available at wileyonlinelibrary.com.]

DISCUSSION

The 3D Overhauser-enhanced b-SSFP sequence presented here in combination with CS and undersampling techniques allows us to attain $1 \times 2 \times 3.5 \text{ mm}^3$ voxel size in our phantom in 33 s (70% undersampling in Figs. 6 and 7) at 6.5 mT. The resulting CS reconstructed image is nearly identical to the original fully sampled image and has ~ 2 times higher SNR. This was achieved by inserting the EPR saturation pulses within TR during the prephase/rephase gradients, thus removing the time consuming prepolarization step as in other OMRI sequences. As shown in our experiments and simulations (Fig. 5), a large steady-state signal is quickly reached with 90% of the maximum signal reached in < 1.5 s, and constant polarization in the sample is maintained during the remainder of the acquisition. This eliminates the need to correct acquisitions for T_1 decay and to rectify undesirable phase shifts that can occur when using prepolarization techniques (25,46). The maximum signal with b-SSFP at thermal equilibrium is given by $M_{ss} = \frac{1}{2} M_0 \sqrt{T_2/T_1} = 0.47 M_0$ (37). Overhauser saturation pulses during the phase gradient increases M_{ss} by ~ 30 for the sample used here, thus allowing high SNR images comparable to those obtained with conventional OMRI techniques. The simulations provide a reliable tool to optimize the phase encode gradient durations depending on T_1 and T_2 .

The application of EPR saturation pulses during the balanced phase encode gradient events is our first major source of acceleration. This allows us to acquire images twice as fast as spin echo OMRI sequences recently published in the literature (24) with nearly seven times higher spatial resolution ($1 \times 2 \times 3.5 \text{ mm}^3$ vs. $1.25 \times 1.25 \times 30 \text{ mm}^3$). This is possible by covering the spread in electron spin frequencies in the phantom when the maximum 0.1 gauss cm^{-1} phase encode gradient was turned on. This sets an upper limit on the Q factor of the EPR coil, or alternatively, the maximum gradient strength that can be used for these experiments. While the maximum steady-state DNP enhancements would benefit from a higher Q coil, the goal of maintaining nearly constant signal enhancement across the sample during imaging would suffer. However, when the EPR irradiation occurs as separate step before imaging as in other OMRI sequences, the DNP signal is also not constant across the image due to the decay of polarization, so a compromise of higher gradient strength for uneven DNP polarization may be acceptable.

Partial sampling of k-space (and subsequent reconstruction via CS) is our second major acceleration factor. In the case of 70% undersampling, this result in additional 3.5 fold acceleration while keeping the voxel size unchanged, thus resulting in seven times faster acquisition compared with recently published work (24). By undersampling in each phase encode direction according to a gaussian probability density function, the center of k-space is emphasized, preserving image contrast without completely sacrificing the high frequency information at the edge of k-space. However, the choice of the lines sampled in k-space was empirically determined and only a few undersampling patterns were empirically

tested for a given undersampling rate. The degrees of freedom in the generation of undersampling patterns is large (choice of lines sampled, $\sigma_{y,z}$) and a large number of combinations could have been tested with the opportunity to give even better results. However, for the $\sigma_{y,z}$'s used here, the 50% and 70% undersampling rates accurately reproduced the image for different random samplings of k-space. In addition, this work focuses on Cartesian sampling, but alternative sampling trajectories (spiral and radial) have been shown to offer more flexibility in the design of 3D incoherent sampling sequences that are particularly well for the use of CS techniques (47–50).

CS performs natural denoising, bringing an improvement in SNR. Incoherent artifacts resulting from subsampled k-space are efficiently suppressed using L_1 -norm constraints in the image and wavelet domains as previously detailed in the literature (42). However, more than 70% undersampling could not provide satisfying reconstruction in spite of high SNR. The incorporation of prior knowledge (51–53) in the image reconstruction process could overcome this limitation by partially recovering irretrievable loss of information caused by heavy undersampling and further increase our temporal resolution. In addition, it is important to note that the 4.5 min computation time required for the CS reconstruction does not significantly penalize the time saved from undersampling.

The gain in temporal resolution obtained here for 70% undersampling, around 1 s per acquired slice, provides new insight for investigating cases where high temporal resolution is needed, such as monitoring the concentration change, oxidation, and metabolism of free radicals that correlate directly with organ functions and tissue health. In addition, shorter durations for the read and phase encode gradients could have been implemented to give significantly shorter acquisition times but at the cost of a decreased spatial resolution. Likewise, doubling the gradient strength in read and both phase encode directions would allow us to reach 2^3 times higher spatial resolution for a fixed acquisition time.

Considering the SAR resulting from the sequence, the amount of power sent to the EPR coil was decreased by a factor of 4 while still keeping the SNR > 25 . Even if a compromise has to be found between the desired spatial resolution of the image and sample heating due to the high power RF, the total amount of RF power sent to the sample during imaging is considerably reduced by the use of undersampling strategies. No temperature rise was measured in the sample for the 50 to 90% undersampling fractions with the maximum EPR power used in this study. With the maximum available EPR power, we acquired images with an in-plane resolution of $1 \times 1 \text{ mm}^2$ as shown in Figure 10 with 70% undersampling (while maintaining the 3.5 mm slice thickness). Total acquisition time was 65 s. This image displays excellent in-plane resolution with very little blurring of the 1 mm features and high SNR.

The images presented here were acquired with a sufficiently long TR to obtain the desired in-plane resolution while keeping the gradient strength low enough for

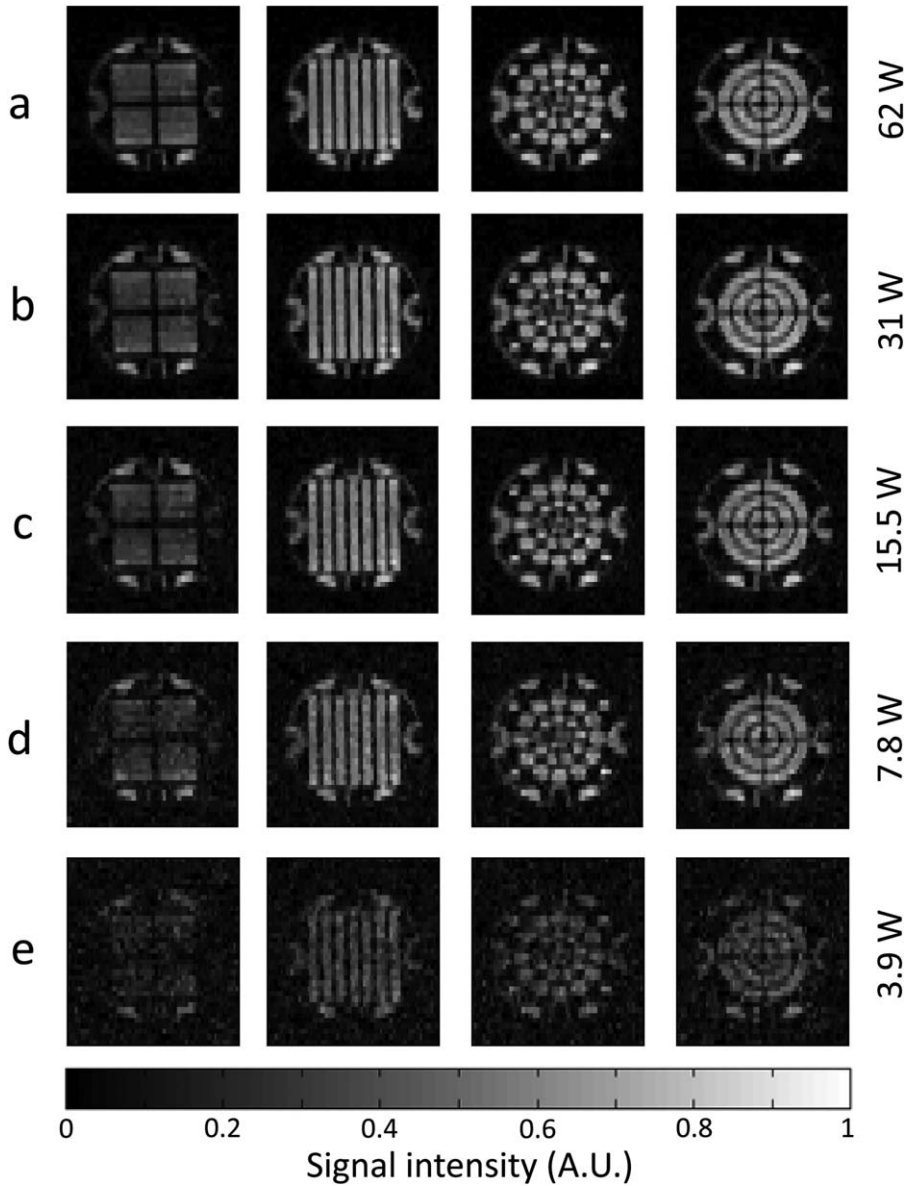


FIG. 9. Images taken with the phantom in configuration 2 and 50% under-sampling as a function of Overhauser drive power: (a) 62 W, (b) 31 W, (c) 15.5 W, (d) 7.8 W, and (e) 3.9 W EPR power. Acquisition matrix: $128 \times 64 \times 32$, voxel size: $2 \times 1 \times 3.5 \text{ mm}^3$, and TR/TE: 54/27 ms. Total acquisition time per image was 56 s.

efficient EPR saturation during phase encoding. We note that the phantom used here has significantly longer T_2 and T_1 relaxation times than would be expected for in vivo applications. Bloch simulations were run to estimate how the current sequence would perform with relaxation times 10 times shorter than the phantom used here. Keeping all simulation parameters as in Figure 5, but decreasing T_1 to 55 ms and T_2 to 49 ms resulted in

Table 2
The Maximum SNR as a Function of Power at the EPR Coil with and without CS for the Phantom in Configuration 2

Power to EPR coil (W)	Max. SNR	
	No CS	CS
62	36	75
31	29.3	48
15.5	21	26.4
7.8	15.2	18.2
3.9	11.4	16.2

<15% reduction in signal intensity (compared with the dashed line in Figure 5). While relaxation times comparable to TR tend to reduce signal, this is partially offset by a faster approach to steady state. More likely to hamper the effectiveness of OMRI in vivo, however, is a decrease in the maximum DNP signal enhancement due to extra ^1H nuclear spin relaxation pathways that compete with relaxation caused by dipolar coupling to the electron spin (27). To observe this effect, simulations were run with the short T_1 and T_2 times above while decreasing the maximum DNP signal enhancement to -10 and -5 . This reduced the steady state signal intensity by 80 and 90%, respectively, compared with the dashed line in Figure 5. Although the signal is much smaller, it is still a factor of 7 and 3.5 times larger than the thermal equilibrium signal with the same parameters, and therefore still provides very useful contrast. In the case of injected free radical detection, this decrease in signal can be partially overcome by increasing the free radical concentration. For example, injection of 0.6 mL

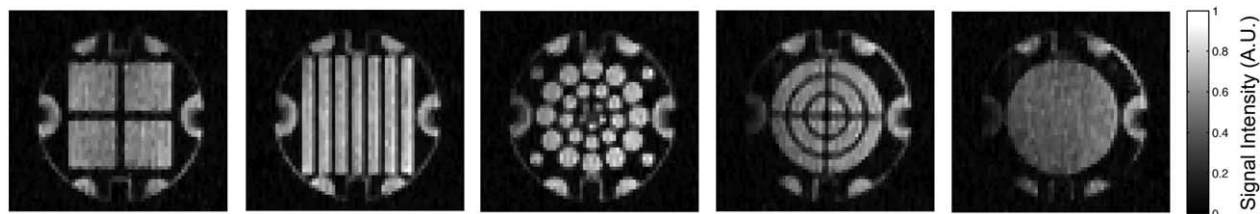


FIG. 10. High-resolution CS reconstructed images taken in the phantom in configuration 2 (five slices are shown) with 70% undersampling. Acquisition matrix: $256 \times 64 \times 32$, voxel size: $1 \times 1 \times 3.5 \text{ mm}^3$, and TR/TE: 54/27 ms. Total acquisition time was 65 s.

of 100 mM nitroxide radical in mice has been reported in recent work (24). Assuming 60–80 mL of blood per kg of bodyweight (54), the dilution factor is between 3 and 4 for a 30 g mouse, resulting in a nominal 29 mM free radical concentration, more than 10 times higher than the 2.5 mM used in the work presented here.

CONCLUSION

We have demonstrated a new strategy for fast high-resolution 3D Overhauser MRI using b-SSFP in a phantom containing 2.5 mM 4-hydroxy TEMPO solution at 6.5 mT. The embedding of EPR excitation pulses directly into the b-SSFP sequence eliminates the prepolarization step used in other OMRI sequences, reducing the acquisition time and obviating the need for long, high power RF EPR pulses. The use of undersampling strategies and CS reconstruction algorithms further reduces imaging time. We have shown that an undersampling rate of 70% gives unperceivable reconstruction errors when compared with the fully sampled data sets, allowing the acquisition of 32 slices in our phantom volume within 33 s. This work overcomes the main limitations of Overhauser enhanced MRI as previously described in the literature, drastically improving speed and resolution, and enabling new opportunities for the measurement of free radicals in living organisms, and for the study of dynamic processes such as metabolism and flow.

ACKNOWLEDGMENTS

The authors thank Ronald Walsworth and Stephen DeVience for assistance with relocating and upgrading the low-field scanner, Jennifer McNab and Thomas Witzel for valuable discussions on implementing b-SSFP sequences at 6.5 mT, and David Donoho and Michael Lustig for sharing the package wavelet toolbox (Wavelab) online with the scientific community.

REFERENCES

- Ardenkjaer-Larsen JH, Laursen I, Leunbach I, Ehnholm G, Wistrand LG, Petersson JS, Golman K. EPR and DNP properties of certain novel single electron contrast agents intended for oximetric imaging. *J Magn Reson* 1998;133:1–12.
- James PE, Madhani M, Roebuck W, Jackson SK, Swartz HM. Endotoxin-induced liver hypoxia: defective oxygen delivery versus oxygen consumption. *Nitric Oxide* 2002;6:18–28.
- Ahn KH, Scott G, Stang P, Conolly S, Hristov D. Multiparametric imaging of tumor oxygenation, redox status, and anatomical structure using overhauser-enhanced MRI–prepolarized MRI system. *Magn Reson Med* 2011;65:1416–1422.
- Lurie DJ, Davies GR, Foster MA, Hutchison JMS. Field-cycled PEDRI imaging of free radicals with detection at 450 mT. *Magn Reson Imaging* 2005;23:175–181.
- Massot P, Parzy E, Pourtau L, Mellet P, Madelin G, Marque S, Franconi J-M, Thiaudiere E. In vivo high-resolution 3D Overhauser-enhanced MRI in mice at 0.2 T. *Contrast Media Mol Imaging* 2012;7:45–50.
- Kosem N, Naganuma T, Ichikawa K, Phumala Morales N, Yasukawa K, Hyodo F, Yamada K-I, Utsumi H. Whole-body kinetic image of a redox probe in mice using Overhauser-enhanced MRI. *Free Radic Biol Med* 2012;53:328–386.
- Caia GL, Efimova OV, Velayutham M, El-Mahdy MA, Abdelghany TM, Kesselring E, Petryakov S, Sun Z, Samouilov A, Zweier JL. Organ specific mapping of in vivo redox state in control and cigarette smoke-exposed mice using EPR/NMR co-imaging. *J Magn Reson* 2012;216:21–27.
- Mellet P, Massot P, Madelin G, Marque SRA, Harte E, Franconi J-M, Thiaudiere E. New concepts in molecular imaging: non-invasive MRI spotting of proteolysis using an overhauser effect switch. *PLoS One* 2009;4:e5244.
- Halpern HJ, Chandramouli GV, Barth ED, Yu C, Peric M, Grdina DJ, Teicher BA. Diminished aqueous microviscosity of tumors in murine models measured with in vivo radiofrequency electron paramagnetic resonance. *Cancer Res* 1999;59:5836–5841.
- Barros W, Engelsberg M. Enhanced Overhauser contrast in proton-electron double-resonance imaging of the formation of an alginate hydrogel. *J Magn Reson* 2007;184:101–107.
- Eaton GR, Eaton SS, Ohno K. EPR imaging and in vivo EPR. Boca Raton: CRC Press; 1991.
- Kuppusamy P, Chzhan M, Zweier J. Principles of imaging. In: Berliner LJ, editor. *Biological magnetic resonance*, Vol. 18. In vivo EPR (ESR): theory and applications. New York: Kluwer Academic/Plenum Publishers; 2003. p 99–152.
- Halpern HJ, Yu C, Peric M, Barth ED, Karczmar GS, River JN, Grdina DJ, Teicher BA. Measurement of differences in pO₂ in response to perfluorocarbon/carbogen in F5a and NFSa murine fibrosarcomas with low-frequency electron paramagnetic resonance oximetry. *Radiat Res* 1996;145:610–618.
- Halpern HJ, Yu C, Peric M, Barth E, Grdina DJ, Teicher BA. Oxymetry deep in tissues with low-frequency electron paramagnetic resonance. *Proc Natl Acad Sci USA* 1994;91:13047–13051.
- Subramanian S, Yamada K-I, Irie A, Murugesan R, Cook JA, Devashayam N, Van Dam GM, Mitchell JB, Krishna MC. Noninvasive in vivo oximetric imaging by radiofrequency FT EPR. *Magn Reson Med* 2002;47:1001–1008.
- Velayutham M, Li H, Kuppusamy P, Zweier JL. Mapping ischemic risk region and necrosis in the isolated heart using EPR imaging. *Magn Reson Med* 2003;49:1181–1187.
- He G, Samouilov A, Kuppusamy P, Zweier JL. In vivo imaging of free radicals: applications from mouse to man. *Mol Cell Biochem* 2002;234/235:359–367.
- Lurie DJ, Bussell DM, Bell LH, Mallard JR. Proton-electron double magnetic resonance imaging of free radical solutions. *J Magn Reson* 1988;76:366–370.
- Golman K, Petersson JS, Ardenkjaer-Larsen JH, Leunbach I, Wistrand LG, Ehnholm G, Liu K. Dynamic in vivo oxymetry using overhauser enhanced MR imaging. *J Magn Reson Imaging* 2000;12:929–938.
- Krishna MC, English S, Yamada K, et al. Overhauser enhanced magnetic resonator imaging for tumor oximetry: coregistration of tumor anatomy and tissue oxygen concentration. *Proc Natl Acad Sci USA* 2002;99:2216–2221.

21. Utsumi H, Yamada K-I, Ichikawa K, Sakai K, Kinoshita Y, Matsumoto S, Nagai M. Simultaneous molecular imaging of redox reactions monitored by Overhauser-enhanced MRI with ¹⁴N- and ¹⁵N-labeled nitroxyl radicals. *Proc Natl Acad Sci USA* 2006;103:1463–1468.
22. Li H, He G, Deng Y, Kuppusamy P, Zweier JL. In vivo proton electron double resonance imaging of the distribution and clearance of nitroxide radicals in mice. *Magn Reson Med* 2006;55:669–675.
23. Benial AM, Ichikawa K, Murugesan R, Yamada K, Utsumi H. Dynamic nuclear polarization properties of nitroxyl radicals used in Overhauser-enhanced MRI for simultaneous molecular imaging. *J Magn Reson* 2006;182:273–282.
24. Sun Z, Li H, Petryakov S, Samouilov A, Zweier JL. In vivo proton electron double resonance imaging of mice with fast spin echo pulse sequence. *J Magn Reson Imaging* 2012;35:471–475.
25. Youngde W, Lurie DJ, Foster MA. Rapid imaging of free radicals in vivo using hybrid FISP field-cycled PEDRI. *Phys Med Biol* 2002;47:1091–1100.
26. Tsai LL, Mair RW, Rosen MS, Patz S, Walsworth RL. An open-access, very-low-field MRI system for posture-dependent ³He human lung imaging. *J Magn Reson* 2008;193:274–285.
27. Hausser KH, Stehlik D. Dynamic nuclear polarization in liquids. *Adv Magn Reson* 1968;3:79–139.
28. Muller-Warmuth W, Meise-Gresch K. Molecular motions and interactions as studied by dynamic nuclear polarization (DNP) in free radical solutions. *Adv Magn Reson* 1983;11:1–45.
29. Alderman DW, Grant DM. An efficient decoupler coil design which reduces heating in conductive samples in superconducting spectrometers. *J Magn Reson* 1979;36:447–451.
30. Lurie DJ, Li H, Petryakov S, Zweier JL. Development of a PEDRI free-radical imager using a 0.38 T clinical MRI system. *Magn Reson Med* 2002;47:181–186.
31. Rabi II, Zacharias JR, Millman S, Kusch P. A new method of measuring nuclear magnetic moment. *Phys Rev* 1938;53:318.
32. Bottomley PA, Andrew ER. RF magnetic field penetration, phase shift and power dissipation in biological tissue: implications for NMR imaging. *Phys Med Biol* 1978;23:630–643.
33. Jin J. *Electromagnetic analysis and design in magnetic resonance imaging*. Boca Raton, FL: CRC Press; 1998.
34. Collins CM, Li S, Smith MB. SAR and B1 field distributions in a heterogeneous human head model within a birdcage coil. Specific energy absorption rate. *Magn Reson Med* 1998;40:847–856.
35. Collins CMC, Smith MBM. Calculations of B(1) distribution, SNR, and SAR for a surface coil adjacent to an anatomically-accurate human body model. *Magn Reson Med* 2001;45:692–699.
36. Collins CM, Wang Z. Calculation of radiofrequency electromagnetic fields and their effects in MRI of human subjects. *Magn Reson Med* 2011;65:1470–1482.
37. Scheffler K, Lehnhardt S. Principles and applications of balanced SSFP techniques. *Eur Radiol* 2003;13:2409–2418.
38. Candes EJ, Romberg J, Tao T. Robust uncertainty principles: exact signal reconstruction from highly incomplete frequency information. *IEEE Trans Inform Theory* 2006;52:489–509.
39. Donoho DL. Compressed sensing. *IEEE Trans Inform Theory* 2006;52:1289–1306.
40. Candes EJ, Wakin MB. An introduction to compressive sampling. *IEEE Signal Process Mag* 2008;25:21–30.
41. Rudin LI, Osher S, Fatemi E. Nonlinear total variation based noise removal algorithms. *Phys D: Nonlinear Phenom* 1992;60:259–268.
42. Lustig M, Donoho D, Pauly JM. Sparse MRI: the application of compressed sensing for rapid MR imaging. *Magn Reson Med* 2007;58:1182–1195.
43. Pruessmann KP, Weiger M, Scheidegger MB, Boesiger P. SENSE: sensitivity encoding for fast MRI. *Magn Reson Med* 1999;42:952–962.
44. Oh S, Webb AG, Neuberger T, Park B, Collins CM. Experimental and numerical assessment of MRI-induced temperature change and SAR distributions in phantoms and in vivo. *Magn Reson Med* 2010;63:218–223.
45. Matsumoto S, Yamada K, Hirata H, Yasukawa K, Hyodo F, Ichikawa K, Utsumi H. Advantageous application of a surface coil to EPR irradiation in overhauser-enhanced MRI. *Magn Reson Med* 2007;57:806–811.
46. Puwanich P, Lurie DJ, Foster MA. Rapid imaging of free radicals in vivo using field cycled PEDRI. *Phys Med Biol* 1999;44:2867–2877.
47. Lustig M, Lee J, Donoho D, Pauly J. Faster imaging with randomly perturbed, undersampled spirals and L1 reconstruction. In *Proceedings of the 13th Annual Meeting of ISMRM*, Miami Beach, Florida, USA, 2005. p. 155.
48. Santos JM, Cunningham CH, Lustig M, Hargreaves BA, Hu BS, Nishimura DG, Pauly JM. Single breath-hold whole-heart MRA using variable-density spirals at 3T. *Magn Reson Med* 2006;55:371–379.
49. Ye JC, Tak S, Han Y, Park HW. Projection reconstruction MR imaging using FOCUSS. *Magn Reson Med* 2007;57:764–775.
50. Block KT, Uecker M, Frahm J. Undersampled radial MRI with multiple coils. Iterative image reconstruction using a total variation constraint. *Magn Reson Med* 2007;57:1086–1098.
51. Mistretta CA, Wieben O, Velikina J, Block W, Perry J, Wu Y, Johnson K, Wu Y. Highly constrained backprojection for time-resolved MRI. *Magn Reson Med* 2005;55:30–40.
52. Chen G-H, Tang J, Leng S. Prior image constrained compressed sensing (PICCS): a method to accurately reconstruct dynamic CT images from highly undersampled projection data sets. *Med Phys* 2008;35:660–663.
53. Lauzier PT, Tang J, Chen G-H. Prior image constrained compressed sensing: implementation and performance evaluation. *Med Phys* 2012;39:66–80.
54. Sluiter W, Oomens LWM, Brand A, Van Furth R. Determination of blood volume in the mouse with ⁵¹Chromium-labelled erythrocytes. *J Immunol Methods* 1984;73:221–225.

2D Imaging in a Lightweight Portable MRI Scanner without Gradient Coils

Clarissa Zimmerman Cooley^{1,2}, Jason P. Stockmann^{1,3}, Brandon D. Armstrong^{1,3}, Mathieu Sar-
racanie^{1,3}, Michael H. Lev^{4,5}, Matthew S. Rosen^{1,3,5}, Lawrence L. Wald^{1,5,6}

¹A. A. Martinos Center for Biomedical Imaging, Dept. of Radiology, Massachusetts General
Hospital, Charlestown, MA, USA

²Dept. of Electrical Engineering and Computer Science, Massachusetts Institute of Technology,
Cambridge, MA, USA

³Dept. of Physics, Harvard University
Cambridge, MA, USA

⁴Dept. of Radiology, Massachusetts General Hospital, Boston, MA, USA

⁵Harvard Medical School, Boston, MA, USA

⁶Harvard-MIT Division of Health Sciences Technology
Cambridge, MA, USA

Corresponding Author:

Clarissa Zimmerman Cooley
149 13th Street, Rm 2301, Charlestown, MA 02129
E-mail: clzimmer@mit.edu
Phone: +1-617-724-1839

Running Title: Lightweight MRI Scanner without Gradient Coils

Keywords: *portable MRI, low-field MRI, nonlinear SEMs, Halbach magnet, parallel imaging*

Word count: 6108

Abstract

Purpose: As the premiere modality for brain imaging, MRI could find wider applicability if lightweight, portable systems were available for siting in unconventional locations such as Intensive Care Units, physician offices, surgical suites, ambulances, emergency rooms, sports facilities, or rural healthcare sites.

Methods: We construct and validate a truly portable ($<100\text{kg}$) and silent proof-of-concept MRI scanner which replaces conventional gradient encoding with a rotating lightweight cryogen-free, low-field magnet. When rotated about the object, the inhomogeneous field pattern is used as a rotating Spatial Encoding Magnetic field (rSEM) to create generalized projections which encode the iteratively reconstructed 2D image. Multiple receive channels are used to disambiguate the non-bijective encoding field.

Results: The system is validated with experimental images of 2D test phantoms. Similar to other non-linear field encoding schemes, the spatial resolution is position dependent with blurring in the center, but is shown to be likely sufficient for many medical applications.

Conclusion: This novel MRI scanner demonstrates the potential for portability by simultaneously relaxing the magnet homogeneity criteria and eliminating the gradient coil. This new architecture and encoding scheme shows convincing proof of concept images that are expected to be further improved with refinement of the calibration and methodology.

Introduction

Specialized, portable MRI systems have the potential to make MR neuroimaging possible at sites where it is currently unavailable and enable immediate, “point-of-care” detection and diagnosis of acute intracranial pathology which can be critical in patient management. For example, the characterization of acute post-traumatic space occupying brain hemorrhage is a time-sensitive emergency for which simple clinical assessment and even urgent CT scanning may be insufficient. While conventional MR scanners are capable of making this diagnosis, they are not available in remote locations. In Intensive Care Units scanners are generally nearby, but are difficult to utilize because of the dangers associated with transporting critical care patients. A portable bed-side scanner could offer major benefits in such situations. Portable, low-cost scanners are compelling for applications where power, siting and cost constraints prohibit conventional scanners. Examples include clinics in rural or underdeveloped areas, military field hospitals, sports arenas, and ambulances. Finally, analogous to the current use of ultra-sound, a low-cost and easy-to-implement scanner could find uses in neurology, neurosurgery or neuro-oncology examination rooms for routine disease monitoring (e.g. monitoring ventricle size after stent placement). The development of a portable scanner relies on the co-design of a new image encoding methods and simplified hardware. This approach is detailed in the present work.

Traditional Fourier MR imaging methods rely on homogeneous static polarizing fields (B_0) and high strength linear Spatial Encoding Magnetic Fields (SEMs) produced by magnetic gradient coils. Conventional scanners utilize high cost superconducting wire, liquid cryogen cooling systems, and high power supplies and electronics. These aspects make it difficult to simply scale-down conventional MRI scanners to portable, low cost devices. Recently in (1) and (2), high resolution imaging has been achieved with table-top and small bore permanent magnet systems with long acquisition times (1), including a mobile MRI system developed for outdoor imaging of small tree branches (2), but these scanners lack a bore size suitable for brain imaging and the long acquisition times are not conducive to imaging in triage settings. Other approaches that scale-down the size of conventional systems for intra-operative MRI show promise (3). However, while these systems are relatively easy to retrofit in operating room, they are not truly portable.

In the present work, we use a novel image encoding method based on rotating spatial encoding magnetic fields (rSEM) to create a portable scanner. We replace the B_0 magnet **and** linear gradient coils with a rotating permanent magnet featuring an inhomogeneous field pattern used for spatial encoding. In this scheme, the inhomogeneity in the B_0 field serves as a spatial encoding magnetic field (SEM), and is requirement for image encoding not a nuisance. Loosening the homogeneity constraint of some conventional magnet designs leads to a reduction in the minimum required magnet material, and allows for more sparse/lightweight designs (45kg in our prototype). Additionally, the rotation of the magnet’s inhomogeneous field pattern replaces the function of heavy switchable gradient coils with significant power requirements.

Several NMR devices for niche applications have explored relaxing the magnet homogeneity constraint, as well as reducing the reliance on traditional Fourier image encoding. The oil well-logging industry was the first to explore the idea of mobile NMR using “external sample” or “inside-out” NMR tools for measuring fluid in rock formations down-hole (4). This work was initially done with electromagnets or in the earth’s field, but the advent of rare-earth magnets with high energy products such as SmCo and NdFeB (5), has allowed more effective borehole NMR tools to be developed (6). Some portable single-sided NMR devices (7,8) exploit inhomogeneous magnetic fields from permanent magnets for 1D spatial encoding. In these systems a rare-earth magnet array is placed against the object such that the field falls off roughly linearly with depth. Broadband excitation and spin-echo refocusing are used to obtain a 1D depth profile of the water content in the object (9–11). Thus, these systems use the inhomogeneity of the small magnet to spatially encode the depth of the water; a principle that we will exploit in a more complete way.

Previously, Cho et al. implemented a mechanically rotating DC gradient field in conjunction with a conventional MRI scanner with the motivation of silent imaging (12). In that case, the rotating electromagnet produced a linear gradient field so traditional projection reconstruction methods could be used. In the presently described portable scanner, the dominant SEM field term is quadrupolar, which requires specialized acquisition and reconstruction techniques. Spatial encoding with similar nonlinear fields created with electromagnets has recently drawn attention as a way to achieve focused high imaging resolutions, reduced peripheral nerve stimulation (13), and improved parallel imaging performance (14). In our scanner, the approximately quadrupolar

SEM fields are physically rotated around the object along with the B_0 field, and stationary RF coils are used to acquire generalized projections of the object in spin-echo train form.

In this manuscript, we describe the design, construction, and testing of a portable 2D MRI scanner. We show that the encoding scheme we introduce can achieve a resolution of a few millimeters in phantom images. While full 3D encoding is not demonstrated, the system is compatible with RF encoding schemes, such as the TRASE method (15,16), capable of adequately encoding the third dimension (along the axis of the cylindrical magnet). The magnet design and initial encoding attempts were previously reported in abstract form (17–19).

Methods

Magnet and field mapping

The described rSEM encoding method is valid for arbitrary encoding field shapes, although the shape will affect the spatially variable resolution of the images. A sparse dipolar Halbach cylinder design similar to the “NMR Mandhala” (20,21) was chosen to produce the rotating B_0 field presented here. This arrangement of permanent magnets produces an approximately uniform field directed transverse to the axis of the cylinder (22). The major design criteria for our Halbach magnet were: 1) maximum average field for highest SNR, 2) sufficient field variation for spatial encoding but not so inhomogeneous that excessive measurement or excitation bandwidths were required, 3) minimum volume of permanent magnet material to keep cost and weight down, 4) use of stock rare-earth magnet material shapes, and 5) minimum size to fit the head (in order to maximize B_0). Note, the design was not focused on the specific spatial encoding field shape, and the resulting pattern in the constructed magnet was accepted as the SEM for the presented scanner. The Halbach cylinder design consists of a 36 cm diameter array of 20 rungs comprising N42 grade NdFeB magnets that are each 1x1x14” (magnetized through the 1” thickness). Two additional Halbach rings made up of 20 1” NdFeB cubes are added to the ends of the cylinder to reduce field fall-off caused by the relatively short length of cylinder. Figure 1 shows a 3D drawing of the magnet, the simulated field, and constructed magnet.

The predicted field pattern (Fig. 1a-b), as well as the forces between the magnet rungs were simulated using COMSOL Multiphysics (Stockholm, Sweden). This calculation estimated an internal force of 178 N, which is adequately handled by the fiberglass and ABS frame designed

to hold the NdFeB magnet array. The magnet rungs consist of NdFeB magnets stacked inside square fiberglass tubes (McMaster-Carr, Elmhurst, Illinois USA), which are fixed by five water jet cut 3/8" ABS rings (Fig. 1d). Each 14" long magnet rung is comprised of four individual bar magnets (Applied Magnet, Plano, TX, USA) which were bonded together (three 4" bars and a 2" bar). The ABS/fiberglass frame was assembled prior to NdFeB magnet handling, and then the magnet rungs were populated one at a time. Since the 4 magnets comprising each rung repel each other as they are inserted, a magnet loading and pushing jig was necessary to force the magnets together while the magnet bonding adhesive cured (Loctite p/n 331 and 7387, Düsseldorf, Germany). The jig was a simple threaded rod mounted to the magnet assembly frame above the opening of the fiberglass tube.

The constructed magnet weighs 45 kg and has a 77.3 mT average field in the 16cm FOV center plane, corresponding to a 3.29 MHz proton Larmor frequency. The cylindrical magnet sits on PVC rollers covered with a high friction urethane. The MRI console is used to drive a stepper motor (model 34Y106S-LW8, Anaheim Automation, Anaheim, CA, USA) that is attached to the aluminum axis of one of the rollers through a 5:1 gearbox (model GBPH-0901-NS-005, Anaheim Automation, Anaheim, CA, USA). Magnet rotation is incorporated into the pulse sequence so that it is controlled by the MRI console to a precision of one degree at a rate of 10 deg/s. Peripheral nerve stimulation is not a concern with this B_0 rotation rate. Even at 10x the current rotation rate, the dB/dt from the rotating magnet is 2 orders of magnitude below the dB/dt generated by a modest clinical gradient system. The magnet assembly is enclosed in a copper mesh Faraday cage to reduce RF interference.

An initial 3D field map was obtained with a 3-axis gaussmeter probe attached to a motorized stage. The measured field shape is roughly quadrupolar, similar to the fields used in the initial realization of multipolar PatLoc (Parallel Imaging Technique using Localized Gradients) encoding (13), but with significant higher-order components as well. The measured field variation range in y - z (imaging plane), x - z , and x - y planes of a 16 cm sphere were $\Delta f_{yz} = 95$ kHz, $\Delta f_{xz} = 60$ kHz and $\Delta f_{xy} = 52$ kHz. Large Larmor frequency bandwidths make it difficult to design RF excitation and refocusing pulses that achieve the same flip angle and phase across all the spins. In addition, it is difficult to make transmit and receive coils uniformly sensitive over the entire bandwidth. Therefore, shimming was done to decrease field variation (no attempt was made to

reshape the SEM). The field variation was shimmed down to $\Delta f_{yz} = 32$ kHz, $\Delta f_{xz} = 32.5$ kHz and $\Delta f_{xy} = 19$ kHz with the addition of small shim magnets (0.5" diameter, 0.25" length cylindrical NdFeB magnets) which were attached to the fiberglass rungs. The 3 planes of the shimmed field map are shown in figure 2.

An accurate field map is critical for image reconstruction, particularly when nonlinear encoding fields force the use of iterative matrix solvers rather than the Fourier transform (14). The field is perturbed by external fields (including the earth's magnetic field), and must be remapped when the magnet is relocated. In order to quickly acquire center-plane field maps, a linear array of 7 field probes spaced 1.5cm apart was constructed (Fig. 3a). The field probes are tuned 5mm long, 4mm diameter, 18-turn solenoids measuring signal from 1mm capillaries of CuSO₄-doped water (23). To acquire a field map the probes are held stationary while the magnet is rotated around them. Polynomial basis functions are then fit to the measured points and the field map (Fig. 3b) is synthesized. The polynomial coefficients up to 6th order of one magnet rotation angle are shown in table 1. The net magnetic field from the NdFeB magnets is sensitive to temperature (on the order of 4 kHz/deg C for the Halbach magnet) as well as interactions with external fields, so an additional field probe is used to monitor field drift during data acquisition. This navigator probe is mounted to the Halbach array and rotates with the magnet. The measured field changes, ΔB_0 , are then accounted for in the image reconstruction.

Acquisition Method

To acquire data, the magnet is physically rotated around the sample in discrete steps. At each rotation step, generalized projections onto the nonlinear field are acquired (similar to those described in (24)). Examples of these projections are shown in Fig. 4 for a simple two-sphere phantom. The field experienced by the spheres changes at each rotation due to the non-linear SEM, providing new information in each projection.

The constructed Rx coil array (Fig. 5a) consists of eight 8cm diameter loops of wire encircling the FOV on the surface of a 14cm diameter cylinder. The inductances of the coils are roughly 230 nH, requiring capacitors on the order of 10 nF (Voltronics, Salisbury, MD) for tuning. Geometric decoupling and PIN diode detuning were implemented (25, 26). The coils are

tuned and matched to 50 Ohm impedance low noise preamplifiers (MITEQ P/N AU-1583, Hauppauge, NY).

A Tecmag Apollo console with TNMR software (Houston, TX) was used. The console has 1 transmit channel, 3 gradient channels, and 1 receive channel. Since the programmable gradient analog outputs are not needed for gradient coils, they are used for other purposes. For example, the G_z gradient output is used to control the stepper motor for magnet rotation. The fact that the console only has 1 receive channel means that true parallel imaging cannot be performed. Instead, the receive channel is switched between the coils in the array, acquiring data serially. The G_x gradient output along with a RelComm Technologies (Salisbury, MD) relay and Arduino UNO board are used to switch between the receive coils. Although pre-amp decoupling has not been implemented yet, data is being acquired from one coil at a time, permitting the other receive coils to be detuned to prevent coupling.

Two scanner coordinate systems are defined because the object and RF coils remain stationary while B_0 is rotated. The rotating coordinate system of the magnet and the spins is defined as x', y', z' (examples shown in Fig. 6b), and fixed coordinate system for the coils and objects is defined as x, y, z (shown in Fig. 1a-b). Image reconstruction requires accurate knowledge of the coil sensitivity map, $C_{q,r}(\mathbf{x})$. Here the index q refers to the coil channel and r to the rotation position of the magnet. The coil sensitivity map is different for each rotation position since B_I^- is formed from a projection of the coil's B_I field onto the $x'-y'$ plane (which rotates with the magnet). In conventional MRI, B_I^- is mapped by imaging the object or a phantom with fully sampled encoding by the gradient waveforms. However, this approach is not possible with our encoding scheme because knowledge of $C_{q,r}(\mathbf{x})$ is necessary to form an image without aliasing.

Because of the difficulty of measuring B_I^- on our scanner, we use estimated B_I^- maps. Magnetostatic approximations are suitable at the 3.29 MHz Larmor frequency, so B_I of the individual coils was modeled with Biot-Savart calculations. By symmetry, the x component of the circular surface coils' B_I is zero in the center plane FOV. The x' component B_0 is also nearly zero because of the geometry of the magnet. So the coil sensitivity calculation reduces to a two dimensional problem, since only the B_I component perpendicular to B_0 contributes to the sensitivity map.

To calculate the coil sensitivity map for each rotation (r), the B_I component parallel to B_{0r} (the B_0 vector for rotation r) is subtracted and we are left with the perpendicular component.

$$B_{1r}^\perp = B_1 - (B_1 \cdot B_{0r}) B_{0r} \quad [1]$$

The phase is equal to the angle, θ_r , between B_{1r}^\perp and B_{0r} , which will either be $+90^\circ$ or -90° due to the symmetry properties discussed above. The variation in a single coil's B_I^- as a function of B_0 angle is illustrated in Figure 6a-b, and the B_I^- magnitude for 4 coils and a single B_0 angle is shown in Figure 6c. When B_0 points along the normal to the coil, the sensitivity profile resembles a “donut” pattern with low sensitivity in the center of the FOV. Maximum signal sensitivity occurs when B_0 is oriented orthogonal to the normal vector of the coil loop.

Similar to single-sided imaging methods (7), echo formation requires the use of spin echo sequences in the presence of the inhomogeneous field. The T_2^* of the signal is short due to the static Spatial Encoding Magnetic field (SEM) and it is impossible to do the equivalent of gradient echo refocusing because the sign of the SEMs cannot be quickly switched. However, the encoding can be repeated and averaged to improve SNR in a spin-echo train, which does refocus the SEM. Unlike in high-field systems, the specific absorption rate (SAR) from the consecutive 180° pulses is negligible because of the low excitation frequency (3.29 MHz).

Unlike conventional MRI scanners, the B_0 field of the Halbach magnet is oriented radially instead of along the bore of the magnet. This means that in order for B_I^+ to be orthogonal to B_0 at all rotations, it should be directed along the cylindrical axis of the Halbach magnet. This makes a solenoid more suitable than a birdcage coil for RF excitation. The constructed solenoid, shown in figure 5c, has a 20cm diameter and a 25cm length. $N=25$ turns of AWG 20 was chosen as a reasonable value in the tradeoff between B_I^+ homogeneity and parasitic capacitance from closely spaced windings. The 70 μH Tx coil is tuned to 3.29 MHz with eight 230pF series capacitors distributed along the length of the solenoid, which reduces the susceptibility to stray capacitance. Because the static SEM field is “always on”, the transmit coil must have a relatively low Q in order to excite a wide bandwidth of spins. The Q of the coil is about 60 corresponding to a 55 KHz bandwidth. A 1 KW power amplifier (Tomco, Stepney, SA, Australia) is used to produce short 600W pulses for broadband excitation (25 μs for 90° pulses and 50 μs for 180° pulses).

PIN diode detuning is used in the transmit and receiver coils to prevent coil interaction (25). The tuning/matching circuits are constructed so that the transmit coil is tuned and the receive coils are detuned when the pin diodes are forward biased with console controlled DC voltage. The converse is true when the diodes are reverse biased (Tx coil detuned and Rx coils tuned).

Reconstruction Method

The Halbach magnet's spatial encoding field is approximately quadrupolar and therefore produces a non-bijective mapping between object space and encoding space. This encoding ambiguity leads to aliasing in the image through the origin. As described by Schultz et al. (27), parallel imaging with encircling receive coils can be used to disambiguate the non-bijective mapping. This is possible because the coil sensitivity profiles provide additional spatial encoding that localizes signal within each source quadrant of the FOV, eliminating aliasing. This idea is illustrated in Figure 5b. This specific implementation of the portable scanner closely resembles the case of PatLoc imaging with quadrupolar fields and a radial frequency-domain trajectory (28). However, the measured Halbach SEM is not purely quadrupolar, and the presence of arbitrary field components prevents the decomposition of the rotating SEM into linear combinations of 2 orthogonal encoding fields. For this reason, the direct back-projection reconstruction method described in (28) is not valid, and iterative matrix methods such as those described in (29) are used.

The discretized signal acquired by a coil (q) at a given magnet rotation (r) at time n can be described as

$$s_{q,r}(n) = \sum_{\mathbf{x}} C_{q,r}(\mathbf{x}) e^{-i2\pi k(r,\mathbf{x},n)} m(\mathbf{x}) \quad [2]$$

where $m(\mathbf{x})$ is the magnetization of the object at location vector \mathbf{x} , $C_{q,r}(\mathbf{x})$ is the complex sensitivity of the coil at location \mathbf{x} , and $k(r, \mathbf{x}, n)$ is the evolved phase from the nonlinear gradient at rotation r , location \mathbf{x} , and time n . The exponential term and coil sensitivity term can be grouped together to form the encoding function $enc_{q,r}(\mathbf{x}, n)$.

$$s_{q,r}(n) = \sum_{\mathbf{x}} enc_{q,r}(\mathbf{x}, n) m(\mathbf{x}) \quad [3]$$

The matrix form of this signal equation for a single projection readout acquired with one RF coil is simply

$$\mathbf{S}_{q,r} = \mathbf{E}_{q,r} \mathbf{m}. \quad [4]$$

The acquired signal, $\mathbf{S}_{q,r}$, is a vector made up of the sampled readout points (N_{smp}). The object that we are solving for, \mathbf{m} , is a vector made up of all the image voxels (N_{vox}). The encoding matrix, $\mathbf{E}_{q,r}$, contains the evolved phase of each voxel in the FOV for each time point in the acquisition as well as the coil sensitivity multiplier. With linear gradient fields, \mathbf{E} is made up of the sinusoidal Fourier basis set, which allows the image to be reconstructed using radial back-projection, k-space re-gridding, and other approaches. In the nonlinear SEM case, \mathbf{E} is more complicated, but can be calculated from the measured field maps. Before the appropriately rotated field map is used to calculate the phase evolution, the field change captured by the navigator probe during the acquisition is added as a global offset.

A separate block of the encoding matrix, $\mathbf{E}_{q,r}$ is calculated for the data acquired by each coil at each rotation. There will be a total of $R \times C$ blocks (where R is total number of rotation and C is the total number of coils), which are vertically concatenated to form the full encoding matrix, \mathbf{E} . \mathbf{S} is also made up of vertically concatenated subparts, $\mathbf{S}_{q,r}$, which are the signals acquired from each coil at each rotation.

To reconstruct the image from the acquired data, the object, \mathbf{m} , can be found by inverting the matrix, \mathbf{E} . However, the full encoding matrix size is $N_{\text{smp}} \times R \times C \times N_{\text{vox}}$. In the typical case of 256 readout points, 181 rotations, 8 coils and a 256x256 voxel reconstructed image, the full matrix size is 371K x 65K. Since it is not computationally feasible to invert this matrix, iterative methods such as the Conjugate Gradient method (30) and the Algebraic Reconstruction Technique (31,32) can be used to solve for the minimum norm least squares estimator of \mathbf{m} . The generality of this approach allows arbitrary field shapes and coil profiles as well as systematic errors such as temperature-dependent field drifts to be incorporated into the encoding matrix.

The reconstructed images and simulations shown here were done using the Algebraic Reconstruction Technique. The encoding matrix was calculated line by line during the reconstruction using the appropriately rotated and temperature drift-corrected field map and the calculated coil sensitivity profiles for the given B_0 direction. To demonstrate the importance of temperature

drift compensation, a phantom image was also reconstructed with an uncorrected encoding matrix. The field of view of the images is 16 cm and the in-plane voxel size is 0.625 mm.

Phantom Imaging Methods

Images of a “MIT/MGH” phantom were acquired both with a single channel solenoid Rx coil and with 7 coils of the Rx array. The 3D printed polycarbonate phantom is 1.7cm thick with a 13cm diameter, and is filled with CuSO₄-doped water. Thirty-two averages of a 6 spin-echo train (TR = 550 ms, echo-spacing = 8ms) were acquired for 91 rotation angles over 180 degrees. Navigator field probe data was also acquired at each rotation. The coil array’s lengthy acquisition time of 66 minutes results from multiplexing a single console receiver and would be reduced to 7.3 minutes by acquiring data from all channels and the field probe in parallel.

A 1cm thick lemon slice was imaged using only the bottom 5 surface coils with 181 1° rotations. The total acquisition time was 93 minutes (15.5 minutes if surface coils and navigator probe were acquired in parallel). A single average of a 128 echo train at each rotation provided sufficient SNR. Each echo was recorded as 256 pts with a 20KHz BW (TR = 4500ms, echo spacing = 8ms). For comparison, the lemon image was also reconstructed using only 91 rotations out of 181 acquired rotations in addition to the full reconstruction.

Image simulation methods

The described acquisition method was simulated using the measured field map from the central slice of the Halbach magnet. Images were simulated using a high resolution T₁ brain image or a numerically generated checkerboard with 2.5mm grid size as the “object.” The measured field map and calculated coil profiles of the 8 coil array were used in the forward model to generate the simulated data. In one simulation, an artificial field map was used to simulate the addition of a linear field component to measured SEM. Complex noise was added to the simulations to match noise levels observed in comparable phantom projection. These simulations were done with the same sequence parameters of the lemon image: 181 1° magnet rotations, 256 pt readout, 20KHz BW, echo spacing = 8ms.

Results

Experimental images of the 3D printed “MIT MGH” phantom are shown in Figure 7. The image acquired with the solenoid coil used in transmit/receive mode is shown in Figure 7a. Only the “MGH” part of the phantom was filled at the time, so the top half of the image should ideally be empty. Instead the expected aliasing pattern is seen through the center onto frequency matched quadrants of the FOV. The aliased image is markedly more blurry than one would expect for a purely quadrupolar field, which maps all signals symmetrically about the center during reconstruction. This discrepancy likely arises due to the presence of first-order and higher-order field terms which perturb the symmetry of the dominant quadrupolar field.

The importance of monitoring and correcting for field drift due to temperature is emphasized by comparing Fig. 7b and Fig. 7c which show images with and without temperature drift correction. The drift correction is achieved by monitoring the frequency seen by the navigator field probe which rotates with the magnet. This probe’s frequency is ideally independent of the rotation angle during the acquisition, but varies due to two causes. Firstly, small changes in room temperature translate to a global scaling of the Halbach array’s magnetization and thus the central B_0 . With no attempt to insulate or stabilize the magnet’s temperature, changes up to 0.4 °C and 1.6 KHz were observed over an hour. The second cause for the fixed probe’s change in field as a function of rotation is due to the changing vector sum of the earth’s field and the Halbach field. This effect creates a peak-peak variation of 3.7 kHz for the magnet location and orientation. This effect must also be incorporated in the encoding matrix. Even though field drift correction is applied to Fig. 7c, some of the letters are sharper than others; this is likely attributable to field map inaccuracies.

The 1cm lemon slice images are seen in Figure 8. The use of 5 out of 8 coils of the receive array prevents aliasing in the image, but center blurring is more pronounced in these images than in the simulations (Fig. 9). Figure 8a was reconstructed using half of the rotations angles of Figure 8b, resulting in poorer image quality and streaking artifacts.

Figure 9 shows an encoding and reconstruction simulation using a typical high field T_1 -weighted brain MRI as the imaging object (Fig. 9a). Noise was added to the object model to simulate the lower SNR of the low field scanner. Figure 9b shows a simulated image using the measured encoding field of Halbach magnet. There is no aliasing in the image because the calculated coil sensitivity profiles of the 8 channel Rx array were used. However, there is

blurring in the center which coincides with the shallow region of the nonlinear gradient field. The center blurring in Figure 9c is reduced because the image was simulated using an artificial field map that consists of our measured SEM plus an additional linear field. The simulation of the 2.5mm grid numerical phantom (Fig. 9d) shows the ultimate resolution possible with the existing experimental protocol in the absence of systematic errors. Outstanding resolution at the periphery gradually gives way to a blurry central region.

Discussion

As expected, the non-bijective mapping of the Halbach magnet's SEM results in aliasing. Fortunately, as described in (13) the aliasing is resolved by the addition of a multi-channel receive array with differing spatial profiles and an appropriate geometry. Since the Halbach encoding is dominated by the quadrupolar "PatLoc" SEM, the system's spatially-varying voxel size changes approximately as c/ρ within the FOV, where ρ is the radius and the constant c depends on the strength of the SEM and the length of the readout (27). This means that our Halbach magnet encoding field results in higher resolution at the periphery due to the uniform nature of the SEM near the center of the FOV. This center blurring is seen in both the experimental images in Fig. 8 and the simulations in Fig. 9.

While we did not attempt to control the precise spherical harmonic distribution in the magnet design, future work will likely benefit from shimming the magnet to obtain a more desirable SEM. For example, if a sufficient linear term were added, the uniform encoding field region would not lie on-axis with the rotation. In this case, which is simulated in Fig. 9c, the "blind-spot" would move around the object allowing some rotations to contribute to encoding of any given pixel, as previously explored in "O-Space imaging" (14). Pursuing this strategy even further would result in a SEM containing only a linear term. In this case, the encoding becomes very similar to a radial imaging scheme with conventional gradients, and to the strategy proposed by Cho et al. who used a rotating gradient coil in a conventional magnet (12). With accurate field mapping instrumentation and shimming software, we suspect that the magnet could be shimmed to a more desirable SEM. Although a linear SEM would eliminate the encoding hole and allow a more straightforward reconstruction method, there are advantages to second-order SEMs including the coincidence of the high spatial resolution area and high coil sensitivity area near the edge of the FOV. Note that in our configuration, where the magnet and encoding field rotate together,

we would still have to deal with the effects of the changing orientation of B_0 relative to the body and Rx coils.

The lemon images of Fig. 8 show that when 91 projection rotations are used instead of 181, a radial streaking artifact is visible. The streaking artifacts are consistent with those arising in conventional undersampled radial trajectories played by linear SEMs as well as undersampled radial trajectories played by PatLoc SEMs (27). It has been shown that the use of total variation and total generalized variation priors during reconstruction suppresses streaking artifacts in undersampled conventional radial (33) and PatLoc radial (34) acquisitions. Similar techniques may be pursued in future work to suppress streaking in images obtained with fewer projection rotations of our scanner.

The simulations in Figure 9 show the theoretical resolution of the scanner when systematic errors are eliminated. These errors are most likely a result of field map and coil sensitivity profile inaccuracies, which are critical to the iterative reconstruction (14). The current coil sensitivity profiles facilitate proof-of-concept reconstructions, but their fidelity is suspect because they were calculated rather than measured. In these calculations the magnetostatic Biot Savart approximation was used with no external structures present. While wavelength effects in the body are not expected at this frequency, the close proximity of the conducting magnets and other coils might perturb the experimental fields. Additionally, a 2D field map is currently used to reconstruct thin samples (1 to 1.5cm thick), but field variation does exist in the \hat{x} direction (along the axis of the Halbach cylinder) within the sample thickness. This causes through-plane dephasing and must be incorporated into the encoding matrix based on a 3D field map.

Field map errors arise from temperature drifts which are significant on the time scale of the imaging and mapping acquisitions. We have shown that any uncorrected temperature drift causes substantial blurring in the image (Fig. 7b). Temperature drift is a pervasive problem in permanent magnet MRI and has been addressed in a number of ways. In the current experimental protocol the frequency at a fixed point is measured at every rotation and the drift is built into the encoding matrix as a global offset to the field maps. This method reduces blurring considerably (Fig. 7c), but other options have been proposed for permanent magnet NMR and MRI that may offer higher encoding matrix accuracy. For example, Kose et al. (1) describes the implementation of a NMR lock method plus thermal insulation. Additionally, a new Halbach design was recently

reported which uses two types of magnet materials with different temperature coefficients to substantially reduce the effect of temperature changes on the B_0 field (35). When compared to an uncompensated SmCo magnet, this reduced their temperature coefficient 100 fold, bringing the field drift down to 10ppm for a 3°C temperature change. However this method has the disadvantages of producing a lower field and requiring more magnet material than the traditional design.

For time-efficient acquisitions, true parallel imaging will be needed. To accomplish this goal, a multi-channel receiver console is required, as well as the implementation of pre-amp decoupling. This is advantageous for practical diagnostic reasons and will also alleviate the field drift problem by shortening acquisition times. In addition to multiple channels, future prototypes must be made larger to accommodate the human head. Although the head can be fit into the presented magnet, its 36cm diameter does not leave sufficient room for the transmit and receive arrays as well as the structural supports for the magnetic material. Construction of a larger diameter magnet with the same basic design will result in a reduced B_0 field, although this could be mitigated by adding more magnet material and/or higher grade material. The current B_0 field of 77.3 mT is estimated to decrease to 62 mT if the diameter is increased to 40cm. However if 24 N45 NdFeB magnet rungs are used instead of 20 N42 rungs, a field of 80 mT is theoretically achievable. The standard landmark for brain imaging (between the eyebrows) is 18cm above the shoulders. The presented Halbach magnet was designed using the maximum cylinder length that allows the brain to be centered in the magnet, 14" (~2x18cm). Future magnet designs will likely adhere to this constraint because increasing the length of the magnet requires increasing the bore size to fit shoulders, which would result in a considerably weaker B_0 .

In the described experiments the B_0 field rotates relative to the receiver coils (coils are stationary), which causes the shape of the coil profiles to change with each acquisition angle. However this arrangement is not a requirement for rotating SEM imaging, and in theory the receiver coils could rotate with the magnet. In this case, the coil sensitivity profiles are simply rotated for each acquisition angle, but the shapes of profiles do not change. Data acquisition with rotating coils and stationary coils was simulated. However, there was not a significant difference in performance in either the visual appearance of the reconstructed images or the RMSE (root mean squared error). For data simulated with 91 magnet rotations there was a 0.2% RMSE improve-

ment when using the rotating coil profiles, and for data simulated with 23 magnet rotations (undersampled) there was a 3.6% RMSE improvement. This suggests that rotating the coil array may improve performance when data is undersampled. The 23 rotation simulated images are included in the supplemental material. The rotating receive coil case is similar to the RRFC (Rotating RF Coils) method described in (36, 37), where continuously rotating surface coils are used in a conventional magnet for parallel imaging.

The goal of the current work was to provide a proof-of-principle that the basic 2D encoding scheme can be performed, which was demonstrated with 2D imaging of thin samples. However, the addition of 3rd axis encoding is an obvious requirement for medical applications. A promising possibility for encoding the 3rd dimension (along the axis of rotation) is Transmit Array Spatial Encoding (TRASE) (15,16). TRASE uses custom-designed RF coils to generate uniform amplitude but linear B_1^+ phase variation along the encoding axis. Spatial encoding is achieved using at least two Tx coils with different phase gradients (typically differing by their sign). Spin-echo trains are used in which the linear phase variation is changed by 180 degrees in between successive refocusing pulses. As the sign of the refocusing pulse is flipped over the course of the echo train, k-space is traversed one echo at a time. The resolution depends on the number of echoes used and the slope of the transmitted B_1 phase ramp across the FOV (16). The approach is synergistic with the echo trains used in the Halbach encoding scheme for purposes of signal averaging. Furthermore, at low field, TRASE spin-echo trains do not suffer from the SAR limits that may impact the method's performance at high field.

Conclusion

Using an inhomogeneous magnet for spatial encoding in lieu of gradient coils, we have constructed and demonstrated a lightweight scanner for 2D MR imaging with minimal power requirements. The 2D proof-of concept images from this nearly head-sized imager show the ability of this encoding scheme to produce sufficient spatial resolution and sensitivity for the detection and characterization of many common neurological disorders such as hydrocephalus and traumatic space-occupying hemorrhages. Future work in perfecting the calibration methods is likely to bring experimental image quality closer to the theoretical limit, but the resolution of the current system is sufficient for identifying gross pathologies. With the future implementation of true

parallel imaging and 3D encoding, this scanner has the potential to enable a truly portable, low-cost brain imaging device.

Acknowledgments

The authors thank Matthew Christensen and Cris LaPierre for their 3D modeling and design work, Bastien Guerin for advice on calculating coil sensitivities, and Stephen Cauley for help with reconstruction methods. This research was supported by the Department of Defense, Defense Medical Research and Development Program, Applied Research and Advanced Technology Development Award W81XWH-11-2-0076 (DM09094). This research was carried out at the Athinoula A. Martinos Center for Biomedical Imaging at the Massachusetts General Hospital, using resources provided by the Center for Functional Neuroimaging Technologies, P41EB015896, a P41 Biotechnology Resource Grant supported by the National Institute of Biomedical Imaging and Bioengineering (NIBIB), National Institutes of Health. This project was supported by a training grant from the NIH Blueprint for Neuroscience Research (T90DA022759/R90DA023427). Its contents are solely the responsibility of the authors and do not necessarily represent the official views of the NIH.

Figure Captions

Figure 1: The magnet array consists of twenty 1”x 1”x 14” NdFeB magnets oriented in the $k = 2$ Halbach mode. Additional Halbach rings made of 1”x 1”x 1” magnets were added at the ends to reduce field fall off along the cylindrical axis. (A,B) Simulation of the magnetic field in two planes. The field is oriented transverse to the cylinder axis (z-direction). (C) Schematic of NdFeB magnets composing array. The targeted spherical imaging region (18 cm dia.) is depicted at isocenter. (D) End-view photo of the Halbach magnet mounted on high friction rollers. Magnet was constructed with ABS plastic and square fiberglass tubes containing the NdFeB magnets. Faraday cage not shown.

Figure 2: Measured Larmor frequency maps of the spatial encoding magnetic field (SEM) in the z - y (imaging plane), z - x , and y - x planes of shimmed Halbach magnet. The B_0 field is oriented in the z direction.

Figure 3: (A) Linear array of 7 NMR field probes used for mapping the static magnetic field. The probes are held stationary, while the magnet is rotated around them and points on the 2D center plane are sampled. (B) Measured field map for the center transverse slice through the magnet after fitting 6th order polynomials to the probe data. The black dots mark the location of the probe measurements. The field is plotted in MHz (proton Larmor frequency). This field distribution serves as the SEM information used in image reconstruction.

Figure 4: Schematic depiction of the generalized projections (bottom row) of an object onto the rotating SEM field. The object consists of two water-filled spheres depicted as dashed black lines which are superimposed on the Halbach magnet's SEM field at a few rotations (black arrow depicts B_0 orientation). The NMR spectrum was acquired with a single volume Rx coil. The second spectrum illustrates the frequency aliasing associated multipolar SEMs because the two spheres are located in a nearly common frequency distribution.

Figure 5: (A) Photo of the 8 channel receiver array coil with 3D printed disk-phantom at isocenter. The 14cm diameter array is made up of eight, 8 cm loops overlapped to reduce mutual inductance. (B) Relative voxel size is illustrated as a function of radius from the center using two rotations of the magnet's SEM (field isocontour lines illustrated in figure). Symmetry of the isocontours causes aliasing of each voxel through the origin. Using the local sensitivity profiles of an encircling array of coils, the correct location of each signal source in the FOV can be resolved. (adapted from (28)) (C) Photo of the 25 turn, 20cm diameter, 25cm length solenoid transmit coil.

Figure 6: Biot-Savart calculation of the sensitivity map of the Rx coil array. The white arrows show representative orientations of B_0 , which define the spin coordinate system orientation (x', y', z'). Image reconstruction requires accurate coil sensitivity profiles for each B_0 angle used in the experiment. (A-B) B_I^- magnitude and phase for a single representative surface coil located at the right side of the FOV (position marked with white line). Because of the symmetry of the coils' at isocenter, the coils' x' component is always zero, and the process of taking the projection onto the $x'-y'$ plane (to solve for B_I^-) will produce a vector parallel or anti-parallel to y' . Therefore, the B_I^- phase is always $+90^\circ$ or -90° in the depicted transverse isocenter plane. (C) B_I^- magnitude of 4 different coils of the array (marked with white lines) for a single magnet rotation position.

Figure 7: Experimental 256×256 voxel, 16cm FOV images of a 3D printed phantom with CuSO₄ doped water occupying the interior of the letters and polycarbonate plastic surrounding it. The phantom has a 13cm dia. and is 1.5cm thick. 91 magnet rotations spaced 2° apart were used, readout bandwidth/Npts = 20 KHz/256, TR = 550ms, spin-echo train length = 6 or 16, with 8ms echo-spacing. Echoes in the spin-echo train for a given rotation were averaged. (A) Image acquired with solenoid Rx coil (32 averages of a 6 spin-echo train). (B) Image acquired with 7 coils of the Rx coil array (8 averages of a 16 spin-echo train). Temperature drift was not corrected for. (C) Image from same data as (B), but with temperature drift correction implemented.

Figure 8: Experimental 256 x 256 voxel, 16cm FOV image of a 1 cm thick slice of lemon placed off axis in the magnet. 5 receiver coils of the array were used to acquire 1 average of a 128 spin-echo train, readout bandwidth/Npts = 20 KHz/256, TR = 4500ms, echo-spacing = 8ms. (A) 91 magnet rotations spaced 2° apart were used (B) 181 magnet rotations spaced 1° apart were used.

Figure 9: Simulated images using the calculated sensitivity profiles of the 8 coil Rx array to generate the forward model for 181 1° rotations of the encoding field, 6.4ms, 256 point readouts. The data seen by the Halbach scanner was simulated by processing this “object” through the forward model and adding noise to make it consistent with the SNR of the time-domain signals measured in a water phantom. The model data was then reconstructed using the Algebraic Reconstruction Technique in a 16cm FOV. (A) Reference high resolution 3T T₁ weighted brain image used as the model object. Note: the SEMs were scaled to the brain FOV. (B) Simulated reconstruction using the measured SEM to generate the forward model. (C) Simulated reconstruction using the measured SEM with the additional artificial linear field component (500 Hz/cm). (D) Simulated reconstruction of a 2.5mm grid numerical phantom. Only one quadrant of the FOV is shown, the center of the FOV is marked with white cross-hairs in the upper right.

Table 1: The calculated polynomial coefficients composing the z-y plane (2D imaging plane) of the Halbach spatial encoding field are shown. Measured points from the linear array of field probes (fig. 3) were used for this 6th order polynomial fit.

Supplemental Figure: Simulated images comparing the performance of rotating and stationary receiver coil arrays in the rotating Halbach magnet. Data was simulated using 23 8° rotations of the encoding field and 6.4ms, 256 point readouts. The model data was then reconstructed using the Algebraic Reconstruction Technique in a 16cm FOV. (A) Reference high resolution 3T T₁

weighted brain image used as the model object. Note: the SEMs were scaled to the brain FOV. (B) Simulated reconstruction with added noise using stationary coil profiles (same as experimental setup). The root mean squared error (RMSE) of the simulated image compared with the reference image is 208.3. (C) Simulated reconstruction with added noise using coil profiles that rotate with the magnet, RMSE = 201.1. Compared to brain simulations in figure 9, these simulated images contain more artifacts because the data was undersampled (23 magnet rotations versus 181 rotations).

References

1. Kose K, Haishi T. High resolution NMR imaging using a high field yokeless permanent magnet. *Magn Reson Med Sci*. 2011;10:159–167.
2. Kimura T, Geya Y, Terada Y, Kose K, Haishi T, Gemma H, Sekozawa Y. Development of a mobile magnetic resonance imaging system for outdoor tree measurements. *Rev Sci Instrum*. 2011;82:053704.
3. Gerlach R, du Mesnil de Rochemont R, Gasser T, Marquardt G, Reusch J, Imoehl L, Seifert V. Feasibility of Polestar N20, an ultra-low-field intraoperative magnetic resonance imaging system in resection control of pituitary macroadenomas: lessons learned from the first 40 cases. *Neurosurgery*. 2008;63:272–284; discussion 284–285.
4. Jackson JA, Burnett LJ, Harmon JF. Remote (inside-out) NMR. III. Detection of nuclear magnetic resonance in a remotely produced region of homogeneous magnetic field. *J Magn Reson*. 1980;41:411–421.
5. Sagawa M, Fujimura S, Togawa N, Yamamoto H, Matsuura Y. New material for permanent magnets on a base of Nd and Fe (invited). *J. Appl. Phys*. 1984;55:2083–2087.
6. Kleinberg R., Sezginer A, Griffin D., Fukuhara M. Novel NMR apparatus for investigating an external sample. *J Magn Reson*. 1992;97(3):466–485.
7. Casanova F, Perlo J, Blümich B. *Single-Sided NMR*. Springer; 2011.
8. G. Eidmann RS. The NMR MOUSE, a mobile universal surface explorer. *J Magn Reson Series A*. 1996;122:104–109.
9. Todica M, Fechete R, Blümich B. Selective NMR excitation in strongly inhomogeneous magnetic fields. *J Magn Reson*. 2003;164(2):220–227.
10. Perlo J, Casanova F, Blümich B. 3D imaging with a single-sided sensor: an open tomograph. *J Magn Reson*. 2004;166(2):228–235.

11. Landeghem MV, Danieli E, Perlo J, Blümich B, Casanova F. Low-gradient single-sided NMR sensor for one-shot profiling of human skin. *J Magn Reson.* 2012;215:74–84.
12. Cho ZH, Chung ST, Chung JY, Park SH, Kim JS, Moon CH, Hong IK. A new silent magnetic resonance imaging using a rotating DC gradient. *Magn Reson Med.* 1998;39(2):317–321.
13. Hennig J, Welz AM, Schultz G, Korvink J, Liu Z, Speck O, Zaitsev M. Parallel imaging in non-bijective, curvilinear magnetic field gradients: a concept study. *Magn Reson. Mater. Phys.* 2008;21(1-2):5–14.
14. Stockmann JP, Galiana G, Tam L, Juchem C, Nixon TW, Constable RT. In vivo O-Space imaging with a dedicated 12 cm Z2 insert coil on a human 3T scanner using phase map calibration. *Magn Reson Med.* 2013;69(2):444–455.
15. Sharp JC, King SB. MRI using radiofrequency magnetic field phase gradients. *Magn Reson Med.* 2010;63(1):151–161.
16. Sharp JC, King SB, Deng Q, Volotovskyy V, Tomanek B. High-resolution MRI encoding using radiofrequency phase gradients. *NMR in Biomed.* 2013
17. Zimmerman C, Blau J, Rosen MS, Wald LL. Design and construction of a Halbach array magnet for portable brain MRI. In *Proceedings of the 20th Annual Meeting of ISMRM, Melbourne, Australia, 2012.*2575.
18. Cooley CZ, Stockmann JP, Armstrong BD, Rosen MS, Wald LL. A lightweight, portable MRI brain scanner based on a rotating Halbach magnet. In *Proceedings of the 21st Annual Meeting, Salt Lake City, USA, of ISMRM 2013.*137.
19. Stockmann JP, Cooley CZ, Rosen MS, Wald LL. Flexible spatial encoding strategies using rotating multipolar fields for unconventional MRI applications. In *Proceedings of the 21st Annual Meeting of ISMRM, Salt Lake City, Utah, USA, 2013.*2664.
20. Raich H, Blümli P. Design and construction of a dipolar Halbach array with a homogeneous field from identical bar magnets: NMR Mandhalas. *Concepts in Magnetic Resonance Part B: Magnetic Resonance Engineering.* 2004;23B(1):16–25.
21. Wroblewski P, Szyszko J, Smolik WT. Mandhala magnet for ultra low-field MRI. In: *2011 IEEE International Conference on Imaging Systems and Techniques (IST).* ; 2011. pp. 248–252.
22. Halbach K. Design of permanent multipole magnets with oriented rare earth cobalt material. *Nuclear Instruments and Methods.* 1980;169(1):1–10.
23. De Zanche N, Barmet C, Nordmeyer-Massner JA, Pruessmann KP. NMR probes for measuring magnetic fields and field dynamics in MR systems. *Magn Reson Med.* 2008;60(1):176–186.
24. Schultz G, Gallichan D, Reiser M, Hennig J, Zaitsev M. MR image reconstruction from generalized projections. *Magn Reson Med.* 2013.

25. Edelstein W., Hardy C., Mueller O. Electronic decoupling of surface-coil receivers for NMR imaging and spectroscopy. *Journal of Magnetic Resonance* (1969). 1986 March;67(1):156–161.
26. Roemer PB, Edelstein WA, Hayes CE, Souza SP, Mueller OM. The NMR phased array. *Magn Reson Med*. 1990;16(2):192–225.
27. Schultz G, Ullmann P, Lehr H, Welz AM, Hennig J, Zaitsev M. Reconstruction of MRI data encoded with arbitrarily shaped, curvilinear, nonbijective magnetic fields. *Magn Reson Med*. 2010;64(5):1390–1403.
28. Schultz G, Weber H, Gallichan D, Witschey WRT, Welz AM, Cocosco CA, Hennig J, Zaitsev M. Radial imaging with multipolar magnetic encoding fields. *IEEE Trans Med Imaging*. 2011;30(12):2134–2145.
29. Stockmann JP, Ciris PA, Galiana G, Tam L, Constable RT. O-space imaging: Highly efficient parallel imaging using second-order nonlinear fields as encoding gradients with no phase encoding. *Magn Reson Med*. 2010;64(2):447–456.
30. Hestenes M, Stiefel E. Methods of Conjugate Gradients for Solving Linear Systems. *Journal of Research of the National Bureau of Standards*. 1952;49(6):409–436.
31. Kaczmarz S. Angenäherte Auflösung von Systemen linearer Gleichungen. *Bulletin International de l'Académie Polonaise des Sciences et des Lettres*. 1937;35:355–357.
32. Gordon R, Bender R, Herman GT. Algebraic reconstruction techniques (ART) for three-dimensional electron microscopy and x-ray photography. *J Theor Biol*. 1970;29(3):471–481.
33. Block KT, Uecker M, Frahm J. Undersampled radial MRI with multiple coils. Iterative image reconstruction using a total variation constraint. *Magn Reson Med*. 2007;57(6):1086–1098.
34. Knoll F, Schultz G, Bredies K, Gallichan D, Zaitsev M, Hennig J, Stollberger R. Reconstruction of undersampled radial PatLoc imaging using total generalized variation. *Magn Reson Med*. 2013;70(1):40–52.
35. Danieli E, Perlo J, Blümich B, Casanova F. Highly stable and finely tuned magnetic fields generated by permanent magnet assemblies. *Phys Rev Lett*. 2013;110(18):180801.
36. Trakic A, Weber E, Li BK, Wang H, Liu F, Engstrom C, Crozier S. Electromechanical design and construction of a rotating radio-frequency coil system for applications in magnetic resonance. *IEEE transactions on bio-medical engineering*. 2012;59(4):1068–1075.
37. Li M, Jin J, Trakic A, Liu F, Weber E, Li Y, Crozier S. High acceleration with a rotating radiofrequency coil array (RRFCA) in parallel magnetic resonance imaging (MRI). In: 2012 Annual International Conference of the IEEE Engineering in Medicine and Biology Society (EMBC). ; 2012. pp. 1098–1101.